

THE BOLOCAM GALACTIC PLANE SURVEY. XIV.
PHYSICAL PROPERTIES OF MASSIVE STARLESS AND STAR FORMING CLUMPS

BRIAN E. SVOBODA^{1,†}, YANCY L. SHIRLEY^{1,2}, CARA BATTERSBY³, ERIK W. ROSOLOWSKY⁴,
ADAM G. GINSBURG^{5,6}, TIMOTHY P. ELLSWORTH-BOWERS⁶, MICHELE R. PESTALOZZI⁷,
MIRANDA K. DUNHAM⁸, NEAL J. EVANS II⁹, JOHN BALLY⁶, JASON GLENN⁶

Draft version June 11, 2018

ABSTRACT

We sort 4683 molecular clouds between $10^\circ < \ell < 65^\circ$ from the Bolocam Galactic Plane Survey based on observational diagnostics of star formation activity: compact $70 \mu\text{m}$ sources, mid-IR color-selected YSOs, H_2O and CH_3OH masers, and UCHII regions. We also present a combined NH_3 -derived gas kinetic temperature and H_2O maser catalog for 1788 clumps from our own GBT 100m observations and from the literature. We identify a subsample of 2223 (47.5%) starless clump candidates, the largest and most robust sample identified from a blind survey to date. Distributions of flux density, flux concentration, solid angle, kinetic temperature, column density, radius, and mass show strong (> 1 dex) progressions when sorted by star formation indicator. The median starless clump candidate is marginally sub-virial ($\alpha \sim 0.7$) with $> 75\%$ of clumps with known distance being gravitationally bound ($\alpha < 2$). These samples show a statistically significant increase in the median clump mass of $\Delta M \sim 170 - 370 M_\odot$ from the starless candidates to clumps associated with protostars. This trend could be due to (i) mass growth of the clumps at $\dot{M} \sim 200 - 440 M_\odot \text{Myr}^{-1}$ for an average free-fall 0.8 Myr time-scale, (ii) a systematic factor of two increase in dust opacity from starless to protostellar phases, (iii) and/or a variation in the ratio of starless to protostellar clump lifetime that scales as $\sim M^{-0.4}$. By comparing to the observed number of CH_3OH maser containing clumps we estimate the phase-lifetime of massive ($M > 10^3 M_\odot$) starless clumps to be $0.37 \pm 0.08 \text{ Myr} (M/10^3 M_\odot)^{-1}$; the majority ($M < 450 M_\odot$) have phase-lifetimes longer than their average free-fall time.

Subject headings: ISM: clouds, molecules, surveys — stars: formation — submillimeter: ISM — masers

1. INTRODUCTION

Massive stars ($M > 8 M_\odot$) strongly influence the evolution of galaxies and the ISM, yet their formation remains an open problem in contemporary astrophysics (see reviews by McKee & Ostriker 2007; Tan et al. 2014). A major bottleneck in the study of massive star formation is the difficulty in identifying and systematically analyzing the properties of the incipient phases of intermediate- and high-mass (protocluster) star formation, high-mass starless clumps. These objects fragment into dense starless cores that subsequently contract to form individual or bound systems of protostars (Tan et al. 2014). Starless cores (and gravitationally bound prestellar cores) are cold ($T_d < 20 \text{ K}$), dense ($n(\text{H}_2) > 10^4 \text{ cm}^{-3}$), and centrally concentrated objects that lack an embedded protostar (di Francesco et al. 2007). The study of low-mass ($< 10 M_\odot$) starless cores has received considerable attention due to their proximity and the systematic mapping of nearby molecular clouds in the Gould's Belt (Ward-Thompson et al. 1994; Tafalla

et al. 2004; André et al. 2007, 2013). In contrast, the study of intermediate and high-mass starless cores and clumps is still in a nascent state due in part to their greater distances and few systematic observations to identify them (Wilcock et al. 2012; Tackenberg et al. 2012; Ragan et al. 2013; Traficante et al. 2015a). Our understanding of how cluster formation is initiated and ensuing protocluster evolution both ultimately depend on identifying and constraining the physical properties of representative samples of high-mass starless clumps. This situation is beginning to change with the publication of a catalogs of 170 and 667 starless clumps identified with the *Herschel Space Observatory* towards Infrared Dark Clouds (IRDC; Wilcock et al. 2012; Traficante et al. 2015a). In this paper, we analyze the star formation activity of clumps observed in the Bolocam Galactic Plane Survey to identify a population of over 2000 massive starless clump candidates in a 84.4 square degree region of the first quadrant of the Galaxy.

Recent blind surveys of the dust continuum emission at (sub-)millimeter wavelengths are able to detect embedded star forming regions in a wide range of evolutionary states, including the starless phases (e.g., Tackenberg et al. 2012; Traficante et al. 2015a), throughout the Galaxy. There are three primary surveys that have mapped far-infrared through millimeter wavelength emission in the Milky Way. The Bolocam Galactic Plane Survey¹⁰ (BGPS; Aguirre et al. 2011; Rosolowsky et al. 2010; Ginsburg et al. 2013) at $\lambda = 1.1 \text{ mm}$ surveyed from $-10^\circ < \ell < 90^\circ$ and targeted regions in the second and third quadrants with $|b| < 0.5^\circ$ (expands to $|b| < 1.5$ at selected ℓ) at $33''$ resolution. ATLASGAL (Schuller et al. 2009; Contreras et al. 2013; Csengeri et al. 2014) surveyed at $\lambda = 870 \mu\text{m}$ between $-60^\circ < \ell < 60^\circ$ and $|b| < 1.5^\circ$ with an extension

[†]email: svobodb@email.arizona.edu

¹ Steward Observatory, University of Arizona, 933 North Cherry Avenue, Tucson, AZ 85721, USA

² Adjunct Astronomer, National Radio Astronomy Observatory

⁴ Department of Physics, 4-181 CCIS, University of Alberta, Edmonton AB T6G 2E1, Canada

⁶ CASA, University of Colorado, 389-UCB, Boulder, CO 80309, USA

⁵ European Southern Observatory, Karl-Schwarzschild-Strasse 2, D-85748 Garching bei München, Germany

⁷ University of Gothenburg, SE-412 96 Gothenburg, Sweden

³ Harvard-Smithsonian Center for Astrophysics, 60 Garden Street, Cambridge, MA 02138, USA

⁸ Department of Astronomy, Yale University, P.O. Box 208101, New Haven, CT 06520, USA

⁹ Department of Astronomy, The University of Texas at Austin, 2515 Speedway, Stop C1400, Austin, TX 78712-1205, USA

¹⁰ See http://irsa.ipac.caltech.edu/data/BOLOCAM_GPS/

covering $-80^\circ < \ell < -60^\circ$ and $-2.0 < b < +1.0$ at $22''$ resolution. In the far-infrared and submillimeter, the *Herschel* Infrared Galactic Plane Survey (Hi-GAL; Molinari et al. 2010) surveyed the entire Galactic plane in the five PACS and SPIRE bands from $\lambda = 60 - 500 \mu\text{m}$. In this paper, we shall focus on studying the physical properties of starless and star forming clumps identified in the BGPS.

The BGPS v2.0 survey identified 8294 clumps with 1.1 mm flux densities above 100 mJy and 8594 clumps cataloged in total (Rosolowsky et al. 2010; Aguirre et al. 2011; Ginsburg et al. 2013). The second data release (v2.0) of the Bolocam images and source catalog (Ginsburg et al. 2013) used improved analysis of the time-stream data to improve angular flux recovery with full recovery out to $\sim 80''$ and partial recovery out to $\sim 300''$. The v2.0 data also resolves systematic flux and pointing calibration offsets and includes new fields in the second quadrant. In this work we exclusively use the BGPS v2.0 data products, and all clumps are referenced to the BGPS v2.0 maps and Bolocat clumps.

Extensive followup observations of BGPS clumps have been carried out to determine unique velocities, kinematic distances, and gas kinetic temperatures to use in calculations of physical properties. Followup spectroscopic observations of the BGPS catalog in dense molecular gas tracers $\text{HCO}^+ 3-2$ and $\text{N}_2\text{H}^+ 3-2$ with the Arizona Radio Observatory’s Heinrich Hertz Submillimeter Telescope (HHSMT; Schlingman et al. 2011; Shirley et al. 2013) detected about half of the objects in the BGPS catalog ($> 97\%$ of those clumps have a single velocity component) from which kinematic distances may be derived. A novel Bayesian technique has been developed to calculate a continuous function of the probability that a source lies at a given heliocentric distance (Ellsworth-Bowers et al. 2013, 2014). The posterior Distance Probability Density Function (DPDF) is constructed by multiplying the bimodal likelihood function (with equal probability of being located at the near or far kinematic distance) with prior distributions that account for the source positions relative to the known H_2 distribution in the Galaxy and the coincidence and contrast of $8 \mu\text{m}$ absorption features (Ellsworth-Bowers et al. 2013). Since the dense molecular gas lines are only detected toward approximately half of BGPS clumps, Ellsworth-Bowers et al. (2014) extended the number of sources with bimodal likelihood functions by developing a morphological matching technique between $^{13}\text{CO } 1-0$ from the Galactic Ring Survey (Jackson et al. 2006) and the BGPS 1.1 mm emission. This technique assigns a clump the dominant ^{13}CO velocity component that matches the 1.1 mm morphology. The DPDF formalism is a powerful tool that permits proper accounting and propagation of the distance uncertainty in calculations of distance dependent physical properties (i.e., size, mass, and luminosity).

Early BGPS papers have characterized clump physical properties on modest subsets of the BGPS. Schlingman et al. (2011) determined the physical properties of 529 sources drawn uniformly from the BGPS 1.1 mm flux distribution, finding that BGPS sources have median physical radii of 0.75 pc, median total masses of $330 M_\odot$, and non-thermal linewidths that are 10 times the thermal linewidth on median. Dunham et al. (2011b) performed an initial evolutionary analysis on a subsample of 456 BGPS sources towards which NH_3 was detected, finding a median gas kinetic temperature of 16 K and identifying a subset of starless clump candidates (SCCs) that composes $\sim 1/3$ of their sample. While BGPS sources are commonly referred to generically as clumps, Dunham et al. (2011b) pointed out that BGPS objects are part of a continuum of hierarchical structure

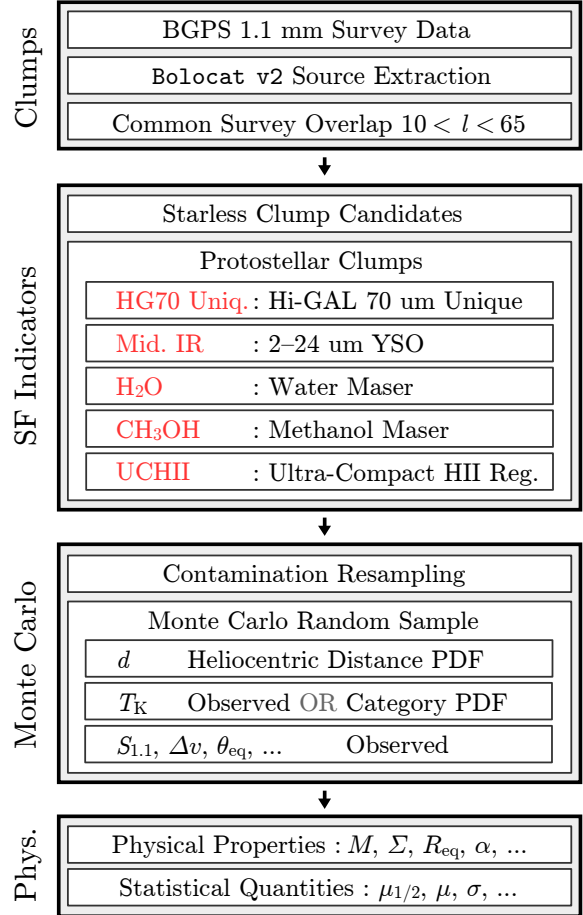


Figure 1. Flow chart describing the BGPS catalog, sorting by star formation indicator, Monte Carlo random sampling, and property calculation.

which sample cores, clumps, and clouds on different scales and at different distances. Indeed, higher resolution observations at $350 \mu\text{m}$ indicate that BGPS clumps typically break up into collections of smaller substructures (Merello et al. 2015). All of these early studies made crude assumptions to resolve the kinematic distance ambiguity (i.e., all sources associated with $8 \mu\text{m}$ absorption are at the near distance or using the presence or lack of HI self-absorption to distinguish between near and far kinematic distance; see §4.3). Ellsworth-Bowers et al. (2015) is the first study to utilize the full power of the DPDF formalism in which they characterize the clump mass distribution for the subset of 1710 clumps with well-constrained DPDFs. They find that the clump mass distribution is best fit with a lognormal distribution with an approximately power-law distribution for high-mass sources and a power-law index that is intermediate between that observed for giant molecular clouds and that observed for the stellar initial mass function.

A significant remaining challenge with the BGPS data set is to identify the star formation activity of all of the BGPS clumps and, in particular, identify the earliest phase of protocluster formation: starless clumps. The extensive characterization and followup of the BGPS presents an excellent sample drawn from a blind survey to rigorously calculate population statistics and physical properties. Measuring the physical properties of starless clumps will not only constrain the initial conditions of protocluster evolution but starless clumps will also be the

proving grounds between theories of high-mass star formation, such as virialized turbulent core accretion (TCA; [McKee & Tan 2003](#)) and a sub-virial competitive accretion (CA; [Bonnell et al. 2001, 2007](#)). Resolving the current tension between these two theories is a major objective in the near-term study of high-mass star formation, but requires the identification of a representative sample of massive starless clumps for further high resolution study. In this paper we address questions related to how starless clumps, as the host environments of future intermediate- and high-mass stars, evolve through the starless phase into the protostellar phase. How long does the starless phase last and how does the starless clump lifetime depend on the mass of the clump? Do clumps undergo significant evolution in their fundamental physical properties and do they undergo significant interaction with the surrounding molecular cloud throughout their lifetimes? We study these questions by analyzing large, statistical subsamples ($N \sim 10^2 - 10^3$) of BGPS clumps.

We present a catalog of 4683 BGPS clumps sorted by observational indicators of star formation activity from a comparison to other Galactic plane surveys in a common overlap range between $10^\circ < \ell < 65^\circ$. We also present 1215 targeted NH_3 and H_2O maser observations with the 100 m Robert C. Byrd Green Bank Telescope (GBT) in §2. Schematically, we follow the procedure shown in Figure 1. In §3 we describe the survey data sets and methods in developing a BGPS star formation catalog. In §4 we describe the methods used to extend the sample of Distance Probability Density Functions to additional sources with a position-position-velocity (PPV) clustering algorithm. We use Monte Carlo sampling of the DPDFs, re-sampling techniques to account for contamination of evolved stars, and sampling of uncertainties on observed quantities to calculate and analyze the physical properties of the BGPS clumps associated to star formation indicators in §5. We discuss the properties of the starless clump candidate sample and possible evidence for clump mass growth during this phase in §6.

2. NH_3 AND H_2O MASER SURVEY OF BGPS SOURCES

2.1. New GBT NH_3 Observations

We have conducted targeted, spectroscopic observations of the NH_3 (1, 1), (2, 2), and (3, 3) inversion transitions as well as the $J_{K_+,K_-} = 6_{1,6} - 5_{2,3}$ 22 GHz H_2O maser line with the GBT¹¹ toward 1215 new BGPS sources. [Dunham et al. \(2011b\)](#) observed 631 BGPS sources within narrow ranges in Galactic longitude, while the new data presented in this work observed BGPS clumps that were detected in dense gas tracer $\text{HCO}^+ 3 - 2$ and had $T_{\text{pk}}(\text{HCO}^+) > 0.3$ K from [Schlingman et al. \(2011\)](#) and [Shirley et al. \(2013\)](#). All new observations were targeted with the center pixel of the K-band Focal Plane Array (KFPA) towards the $S_{1.1\text{mm}}$ flux density peak in the BGPS v2.0 maps ([Ginsburg et al. 2013](#)). We measure NH_3 properties using the slab model previously adopted in [Dunham et al. \(2011b\)](#). This model assumes a uniform-temperature, beam-filling slab of NH_3 with column density $N(\text{NH}_3)$, intrinsic velocity dispersion σ_v , kinetic temperature T_K , and line-of-sight velocity v_{LSR} . The model assumes equal column densities of ortho- and para- NH_3 and that the levels are populated in thermodynamic equilibrium. Given these assumptions, we use a non-linear least square regression to determine the optimal emission model incorporating the hyperfine structure

and opacity of each component that matches the observed data ([Rosolowsky et al. 2008](#)). As in previous pointed spectroscopy studies, the NH_3 fitting provides an excellent reproduction of the observed data with the derived parameters representing emission-weighted averages of the physical conditions within the GBT beam. The observational setup, data reduction methods, and NH_3 fitting techniques are described in detail in [Dunham et al. \(2010, 2011b\)](#).

Previous KFPA observations based on the BGPS v1.0 are updated to match the v2.0 based on the coincidence of the pointing within the BGPS label-mask (discussed in §3.1 describing the catalog cross matching method). Because of the changes in the BGPS catalog between data releases, 178 pointings are duplicates within the same v2.0 clumps and 245 pointings are not within a half-beam of a v2.0 clump. We use the observation closest to the peak flux density $S_{1.1\text{mm}}$ position when there are multiple NH_3 observations within the clump. Columns are included in Table 2 for the `Bolocat` v2.0 source and coordinate offset from the peak flux position. Table 2 also includes the observations from [Dunham et al. \(2011b\)](#) for consistency with the transition to BGPS v2.0. We find an overall detection rate in NH_3 (1,1) at 75%. For accurate estimates of the kinetic temperature we require a source to have $> 3\sigma$ detections in both the (1,1) and (2,2) transitions, resulting in 1663 clumps with suitable T_K fits. Table 2 lists the observed NH_3 properties from the fits and 3σ upper limits for non-detections. Unique T_K measurements are added for 48 BGPS clumps in $10^\circ < \ell < 65^\circ$ from observations in [Wienen et al. \(2012\)](#).

2.2. New GBT H_2O Maser Observations

The 22 GHz H_2O maser line is a well known tracer of protostellar activity and was simultaneously observed in the fourth IF alongside the NH_3 (1, 1) – (3, 3) inversion transitions. A separate reduction in GBTIDL is used for the H_2O maser data because of the complex structure in the spectra from multiple overlapping maser spots in the beam, strong baseline ripples, and a telluric feature at the topocentric zero velocity. The observations are dual-frequency switched with a 5 MHz (69 km s^{-1}) throw. The telluric feature is pressure broadened by ~ 2 MHz ($\sim 30 \text{ km s}^{-1}$) and adds significant structure to the baseline when frequency switched. We baseline fit the spectra with first to third order polynomials to accommodate the complex baseline morphology. Spectra are required to have a $> 5\sigma$ detection in a single channel to qualify as detections. Table 3 lists the observed H_2O maser properties and 3σ upper limits for non-detections. These values include the R.A. and Dec. of the GBT pointing, offset from the BGPS peak position θ_{offset} , velocity of the peak component v_{LSR} , FWZI spread between the left- and right-most velocity components v_{spread} , main-beam peak intensity T_{mb} , main-beam integrated intensity W , and number of unblended velocity components N_{lines} . We observe 472 detections, 343 of which are unique associations not contained in the published surveys by the Mopra and Arcetri observatories discussed in §3.3.1. No significant deviation was seen between the center velocity defined by the first moment and that of the strongest peak. The number of unblended line peaks are identified through visual inspection, but because the maser components can be heavily blended towards strong sources, this number represents a lower limit to the number of maser components towards a BGPS source. For extreme H_2O maser emission, the weaker telluric feature is covered and adds a $\sim 0.5 \text{ K km s}^{-1}$ uncertainty to the calculated H_2O maser integrated intensity. This overlap introduces a $< 1\%$ uncertainty in the $> 100 \text{ K km s}^{-1}$ H_2O maser spectra where

¹¹ The GBT is operated by the The National Radio Astronomy Observatory is a facility of the National Science Foundation operated under cooperative agreement by Associated Universities, Inc.

this occurs.

3. DEVELOPING A STAR FORMATION INDICATOR CATALOG

Recently completed blind Galactic plane surveys with wavelength coverage from the near infrared to radio provide a wide range of indicators of star formation activity. We develop an evolutionary catalog for clumps in the BGPS based on the indicators of star formation that can be associated with the clumps. These evolutionary indicators are then grouped into the categories so that their observed and physical properties can be compared. From this catalog, we identify a subsample of starless clump candidates that lack indicators of protostellar activity. Below we describe the surveys and data sets used to define the flags of star formation indicators. The published surveys include: the Red MSX Survey (Lumsden et al. 2002), Glimpse Red Source Catalog (Robitaille et al. 2008), Hi-GAL 70 μm images (Molinari et al. 2010), H₂O Southern Galactic Plane Survey (Walsh et al. 2011), Methanol Multibeam Maser Survey (Breen et al. 2015), and Coordinated Radio and Infrared Sky Survey for High-mass Star Formation (Hoare et al. 2012) in addition to the GBT H₂O maser and NH₃ observations presented in this paper. We aim for the most uniform coverage in the surveys to accurately compare star formation indicator populations. The common overlap region among the surveys described below is between $10^\circ < \ell < 65^\circ$.

3.1. Catalog Cross-Matching

All published catalogs are cross-matched to the BGPS v2.0 catalog based on line-of-sight coincidence on the sky. The `Bolocat` modified seeded watershed algorithm extracts the clump catalog from the Bolocam data and defines the spatial extent of each clump (Rosolowsky et al. 2010). In this context the “label-map” or “label-mask” refers to the pixels in the Bolocam 1.1 mm flux image associated with a clump by the watershed. For a source from another catalog to be matched with a clump we require that it must be contained within the clump label-mask. In the common overlap region between $10^\circ < \ell < 65^\circ$ there are 4683 BGPS clumps and 2203 clumps with either HCO⁺ or NH₃ dense gas detections. Table 1 lists the observed 1.1 mm properties for the 4683 BGPS clumps within the common overlap region. Table 4 shows the detection statistics for the cross-matched catalogs described in §3.2.1-§3.4 to the BGPS. The table lists the number of sources in the overlap region, the number of sources matched with BGPS clumps, and the number of BGPS clumps containing at least one matched source.

Without accurate independent distances for both a BGPS clump and a catalog source for a star formation tracer, we must rely on spatial coincidence on the sky to cross-match sources. To assess the accuracy of the cross-matched associations, Dunham et al. (2011a) estimate the rate of chance alignments statistically. Dunham et al. (2011a) compare the fraction of cross-matched sources in a given catalog to the average fraction of sources cross-matched when the coordinates have been randomized on area much greater than a single BGPS clump’s environment (see Table 1). Randomizing the coordinates of the catalog preserves the large-scale projected spatial distribution of sources throughout the Galaxy. If the sources in a catalog are quasi-uniformly distributed on the sky, this randomized overlap fraction would simply be the area of the sky covered by BGPS clumps divided by the survey coverage. However, because of Galactic structure and line of sight projection effects,

the distribution of most catalog sources (e.g., red GLIMPSE sources) will not be uniform, and this will be reflected in a higher count of randomized cross-matches towards, e.g., the inner Galaxy. The randomized cross-matching yields typically between 7 – 9% of catalog sources being associated to BGPS clumps. In this work we use the BGPS v2.0 whereas Dunham et al. (2011a) used the BGPS v1.0. We find similar results for the RMS, EGO, and R08 sources matched to clumps (§3.2) and the number of clumps with associated sources within a few percent of the total fraction of matched sources. Catalogs that are new additions in this work such as MMB and CORNISH also have high-association rates, > 80%, so we do not suspect that the sources in these catalogs are highly contaminated by chance alignments. Furthermore, other datasets in this work such as the Hi-GAL visual inspection and the GBT H₂O observations are targeted and the coordinates can not be randomized.

3.2. Infrared Surveys

3.2.1. Red MSX Survey

The Red MSX Survey (RMS; Lumsden et al. 2002, 2013) with observations at 8, 12, 14, and 21 μm defines a sample of massive YSOs complete above $L_{\text{bol}} > 10^4 L_\odot$ and $d_\odot < 10$ kpc, approximately a B0 type main sequence star. The RMS catalog region has complete overlap with the BGPS for $\ell > 10^\circ$, where confusion does not dominate the MSX data. Extensive followup observations of RMS sources yield detailed classifications: proto-planetary nebula, planetary nebula, evolved star, HII region, YSO, OH/IR star, young/old star, HII/YSO, carbon star, and a miscellaneous “other”. We use the RMS classifications associated with YSOs (YSO, HII/YSO, young/old star) to classify BGPS sources in the mid-IR category. We do not associate BGPS sources with star formation activity for the other categories because contamination between the RMS classifications are low. This is further evidenced by the minimal overlap in Table 4. The RMS sources provide a well-vetted sample of massive YSOs, but for spectral types later than B0, or YSOs that are at distances > 10 kpc, the survey is incomplete. Recent Galactic plane surveys by *Spitzer* and *Herschel* offer sensitive datasets through the mid- and far-IR to probe the star formation activity in BGPS clumps and complement the RMS data.

3.2.2. GLIMPSE Red Source Catalog

The GLIMPSE survey is a *Spitzer*/IRAC Legacy survey of the Galactic mid-plane, at 3.6, 4.5, 5.8, 8.0 μm (Benjamin et al. 2003; Churchwell et al. 2009). The GLIMPSE I and II fields provide complete overlap coverage with the BGPS for $10^\circ < \ell < 65^\circ$. Robitaille et al. (2008) (hereafter R08) use the GLIMPSE Catalog to select a total number of 18,949 intrinsically red ($[4.5] - [8.0] \geq 1$) sources that also meet photometric quality criteria. MIPS 24 μm magnitudes are also calculated at the same positions for 86.9% of the sources from the MIPS-GAL survey (Carey et al. 2009). Because GLIMPSE has better spatial resolution and sensitivity than the MSX-survey, lower luminosity YSOs can be detected. R08 estimate that a 100 L_\odot Stage I YSO should be detected at distances between 0.2 – 10 kpc and a $10^4 L_\odot$ YSO between 2 – 30 kpc. Intrinsically red sources are further classified by color-magnitude and color-color selection criteria (see eq. 7-9 Robitaille et al. 2008) into candidate YSOs, “Standard” C- and O-rich AGB stars (sAGB), and “Extreme” AGB stars (xAGB). The color criteria selects sources with spectral index $\alpha \geq -1.2$, which following the

“Class” system of [Greene et al. \(1994\)](#) selects all Class I and a significant number of Class II YSOs. Contamination from planetary nebula and background galaxies is expected to be between 2 – 3%. However, because AGB and YSO sources have similar mid-IR colors, the YSO/AGB discrimination is uncertain based on 4.5, 8.0, and 24 μm photometry alone, with up to 50% contamination between the two categories. [Dunham et al. \(2011b\)](#) estimate a $\sim 40\%$ contamination fraction of YSOs in the R08 candidate AGB sources. We shall account for this contamination in the Monte Carlo sampling in §5. The number of R08 candidate YSO or AGB sources matched to BGPS clumps is listed in Table 4.

An additional class of sources called Extended Green Objects (EGOs) have been identified from the *Spitzer* GLIMPSE data ([Cyganowski et al. 2008](#); [Chen et al. 2013](#)). EGOs are sources of extended 4.5 μm emission from shocked H_2 driven by strong outflows from massive star formation. 72 BGPS clumps match EGOs, and all except one clump (G044.008-00.026) contain RMS YSOs, R08 YSOs, or 70 μm compact sources (see §3.2.4).

3.2.3. MIPS GAL 24 μm

The Version 3.0 data products from the *Spitzer* MIPS GAL survey cover $-69^\circ < \ell < 68^\circ$ and $|b| < 1^\circ$ at 24 μm ([Carey et al. 2009](#)). The MIPS 24 μm band is sensitive to the hot dust found around YSOs and HII regions, but also to envelopes of evolved stars. [Gutermuth & Heyer \(2015\)](#) have created a comprehensive point-source catalog from the MIPS GAL 24 μm maps. Two catalogs are presented: a high-quality catalog and more complete archive. Combined the catalogs total 268,430 point sources in the fields of the BGPS overlap region, with 4.9% of MIPS GAL sources associated to clumps and 80.9% of clumps associated to MIPS GAL point sources. While some subset of MIPS GAL sources do represent observational indicators of embedded protostellar activity, this low match fraction of 4.9% is consistent with the $6.8\% \pm 2.2\%$ randomized match fraction calculated in [Dunham et al. \(2011b\)](#) for RMS Evolved Stars (i.e., sources with no physical association). Figure 2 illustrates this poor correspondence to BGPS clumps. Two maps at 70 μm and 24 μm are shown of the same field centered on a single, isolated clump. Whereas the 24 μm image shows identified point sources from both the Catalog and Archive, only a few point sources have direct association to the clump 1.1 mm emission. In contrast, the 70 μm image uniquely associates a single compact source to the clump. The 70 μm dust continuum emission is more sensitive to the deeply embedded star formation activity that is better positionally correlated to BGPS clumps. We conclude that line of sight association of 24 μm point sources from the MIPS GAL catalog are not a sufficient sole indicator of star formation activity because of the high contamination from evolved stars. Thus while the MIPS GAL flags are not used in any calculations of physical properties, for completeness we present the flags in Table 4 (see §3.5). These contamination issues also strongly affect the lower resolution WISE 22 μm observations. To further refine our set of star formation indicators, rather than pursue color- and quality-selection criteria to identify a less contaminated subsample from the MIPS GAL catalog, we associate clumps to 70 μm compact sources.

3.2.4. Herschel Hi-GAL 70 μm

The *Herschel* Infrared Galactic Plane Survey (Hi-GAL) is a far-IR survey of the Galaxy with the 70 and 170 μm PACS

bands and the 250, 350, and 500 μm SPIRE bands ([Molinari et al. 2010](#)). The Hi-GAL survey completely covers the BGPS fields that we discuss. Previous survey data sets in the 100 μm regime from IRAS and *Akari* are not suitable for detecting faint point sources due to their poor angular resolution ($> 1'$). The *Herschel* Hi-GAL 10.2'' resolution ([Traficante et al. 2011](#)) at 70 μm is essential to disentangling the far-IR emission reprocessed by dust around embedded YSOs and their often active environment. Most important however is the less severe contamination in the Hi-GAL 70 μm images from evolved stars compared to the MIPS 24 μm or WISE 22 μm images. Whereas $> 80\%$ clumps have at least one associated MIPS GAL source, only 46% of clumps have an associated 70 μm compact source from visual identification with clearly correlated positions to the 1.1 mm maps.

Due to complicated background structure, identifying compact sources algorithmically is difficult. The CuTeX algorithm ([Molinari et al. 2011](#)) was developed specifically for identifying sources in highly spatially variable backgrounds such as those found in the Hi-GAL images. Careful visual inspection is necessary because of false negatives where CuTeX misses faint sources and false positives where CuTeX mis-identifies sources in regions of strong emission. Cuts on CuTeX fit parameters were trained on publicly available data in the $\ell = 30^\circ$ field ([Bally et al. 2010](#)) and then applied to all cutout images to compare with the results of the visual inspection classifications. The comparisons show that 77.7% of the classifications agree, and 22.3% disagree. 81% of the disagreements originate from sources flagged with fainter 70 μm sources from the visual inspection but missed by CuTeX.

We visually inspect $5' \times 5'$ cutouts of the reduced Hi-GAL 70 μm band images ([Molinari et al. 2011](#)) for comparison against the BGPS data. For consistency with the catalog matching scheme used for the other surveys in this study, we classify clumps as containing a Hi-GAL 70 μm source if it is within the Bolocat label-mask. Visual inspection was carried out only on the 70 μm images alone, without simultaneous comparison to GLIMPSE or MIPS GAL images to prevent systematic bias in the classifications. We assign BGPS clumps one of five flags in the visual inspection process. Multiple flags are necessary to qualify the image background level and source characteristics. Flags 1, 2, and 4 represent clumps identified with a compact source within the label-mask while flags 0 and 3 lack a clearly identifiable source. Representative 70 μm cutouts of these flags are shown in Figure 3. Flag 1's show a high confidence compact source on the scale of the *Herschel* 10.2'' PSF. Flag 2's are more diffuse than the PSF but identifiable as compact sources due to strong, localized emission above the background level. These are common for extremely bright 70 μm sources with $\geq 80\%$ of uniquely high-mass indicators, RMS sources, CH_3OH masers, and UCHII regions, assigned flag 2's. We identify 944 flag 1 and 1044 flag 2 clumps, or 42.5% of clumps. Flag 4's show a weak, PSF-like source whose classification is lower confidence. Adding the 182 flag 4's increases the total to 46.3% of clumps classified with a Hi-GAL source. The brightness and complexity of the 70 μm background can make the visual source identification difficult. Because of this we assign 1847 flag 0's to clumps with quiescent, smooth, and low-level backgrounds and 655 flag 3's to clumps with bright and more complex backgrounds. The far-IR background of the Milky Way changes locally and as a function of Galactic longitude (generally $10^2 - 10^3$ MJy sr^{-1}), and thus the flux threshold for source detection changes as well.

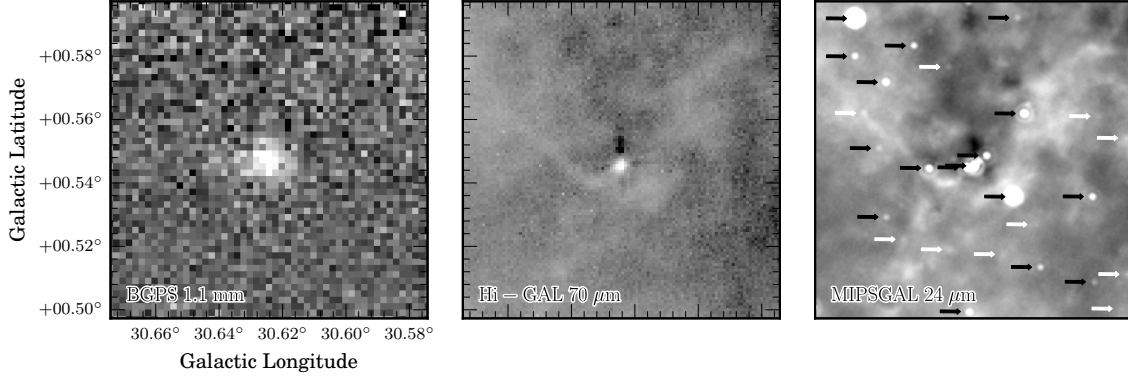


Figure 2. Comparison between BGPS 1.1 mm (Left), Hi-GAL 70 μm (Center), and MIPS GAL 24 μm (Right) with point sources overlaid. The BGPS shows the location of G030.624+00.547 with a clear association to a Hi-GAL compact source where MIPS GAL shows numerous unassociated sources. The black arrows point to the MIPS GAL high-quality Catalog and the white arrows point to the more complete Archive (Gutermuth & Heyer 2015).

The high rate of overlap between 70 μm sources and more extreme indicators along with the large number of unique 70 μm associations suggest that the Hi-GAL data is broadly probing a lower YSO bolometric luminosity, L_{bol} , than the other indicators. To assess the low-luminosity limit of the associations, we compute L_{bol} completeness functions for a representative sample of background levels given the sample of DPDFs in the Distance Catalog. The 70 μm background level and complexity is the limiting factor in the identification of compact sources. A detailed analysis of the background level distribution for the full Hi-GAL 70 μm dataset with the identification threshold quantified through fake source injection is beyond the scope of this paper. Instead, we bracket the completeness function with a sample of 30 clumps associated to the least confident 70 μm identifications (classified as Hi-GAL flag 4), evenly split between low background levels of 500 – 1000 MJy sr^{-1} and high background levels of 2000 – 3000 MJy sr^{-1} . Values are calculated from the cutouts described above. Aperture photometry of the 70 μm sources in these selected regions yields sources identified with flux densities $\lesssim 0.3$ Jy for the low backgrounds and $\lesssim 1$ Jy for the high backgrounds. Using these two detection thresholds, we compare to fluxes derived from the 20,000 axisymmetric YSO radiative transfer models computed in Robitaille et al. (2006, 2007). We use the PACS 70 μm fluxes from the largest physical aperture, 100,000 AU, which corresponds to the 20'' diameter aperture at the median clump distance of 5 kpc (see §5.1.2). We then draw from Monte Carlo simulations for each clump distance probability density function (described in §5.1) to scale the Robitaille et al. (2006) PACS 70 μm model flux and apply the detection threshold cut. Figure 4 shows the completeness function for all clumps with well-constrained distances and the cyan line shows the same but for the subset of clumps between $28^\circ < \ell < 31^\circ$ for which publicly available Hi-GAL data exists (Bally et al. 2010). The dotted lines show the 50% and 90% limits. We find in the low background environments the 70 μm visual flags are 50% complete to YSOs with $L_{\text{bol}} > 10 L_\odot$ and 90% complete to YSOs with $L_{\text{bol}} > 50 L_\odot$. For the high background environments, we find the 50% completeness limit to YSOs at $L_{\text{bol}} > 45 L_\odot$ and 90% complete to YSOs with $L_{\text{bol}} > 140 L_\odot$. To put these luminosities in perspective, a $\sim 1 M_\odot$ and $\sim 5 R_\odot$ YSO accreting at $\sim 10^{-5} M_\odot \text{ yr}^{-1}$ corresponds an accretion luminosity of $\sim 30 L_\odot$ (N.B. episodic accretion rates result in large variations in the accretion luminosity at a given epoch; see Dunham et al. 2014). While the true sample completeness

limits likely lie between these two values, it should be kept in mind that these limits are below the L_{bol} of the other star formation indicators by several orders of magnitude.

Among the positive Hi-GAL classifications, 1027/2170 (47.3%) have one or more additional star formation indicator and 1143/2170 (52.7%) are Hi-GAL 70 μm unique, representative a sample of deeply embedded and early protostellar candidates. In the following analysis, this sample of clumps uniquely identified with star formation activity from 70 μm compact sources is treated separately as its own category. It should be noted that the 70 μm unique category sources may have a MIPS 24 μm counterpart but does not contain any other star formation indicator (unique is defined in terms of our set of star formation indicators).

3.3. Masers

3.3.1. H₂O Masers

We complement the mid- and far-IR star formation indicators with radio observations of masers. The outflows driven by young protostars shock dense regions of the ISM and collisionally pump H₂O that creates a population inversion which drives the maser emission. The typical physical conditions for a masing regions are a spatial density $n \sim 10^7 - 10^9 \text{ cm}^{-3}$, kinetic temperature $T_K \sim 400$ K, spatial extent of $d \sim 0.66$ AU, and an aspect ratio $\sim 50 : 1$ (Hollenbach et al. 2013). H₂O masers are time variable on scales of months to years. The beaming effect of H₂O masers make them a sensitive probe at large distances but because of the necessary narrow geometrical alignment, the non-detection of a H₂O maser does not imply the lack of star formation activity. In addition to YSO molecular outflows, H₂O masers are also observed in the shells around AGB stars (Imai et al. 2002). From high resolution followup of the H₂O Southern Galactic Plane Survey (HOPS; Walsh et al. 2011) and association to catalogs of star formation indicators Walsh et al. (2014) find that 69% of water maser sites are associated with star formation, 19% with evolved stars, and 12% with unknown identification. We expect limited contamination of AGB stars coincident with our GBT pointings because the observations are targeted towards the clump peak $S_{1.1\text{mm}}$ and $N(\text{H}_2)$ positions ($\theta_{\text{HPBW}} \approx 30''$) where a YSO is likely to be located, but a chance alignment by a field AGB star is unlikely. Thus we use the detection of a H₂O maser as an observational indicator of star formation activity.

Large observational H₂O maser survey programs have been

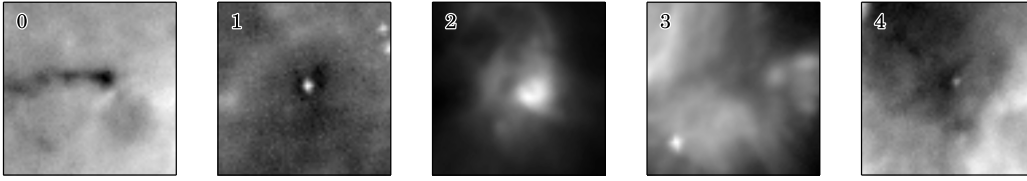


Figure 3. Hi-GAL visual inspection flag examples. Flag 0: quiescent background with no source identified. Flag 1: compact source. Flag 2: diffuse source. Flag 3: bright or complex background with no source identified. Flag 4: faint or low confidence source. The cutouts are $5' \times 5'$.

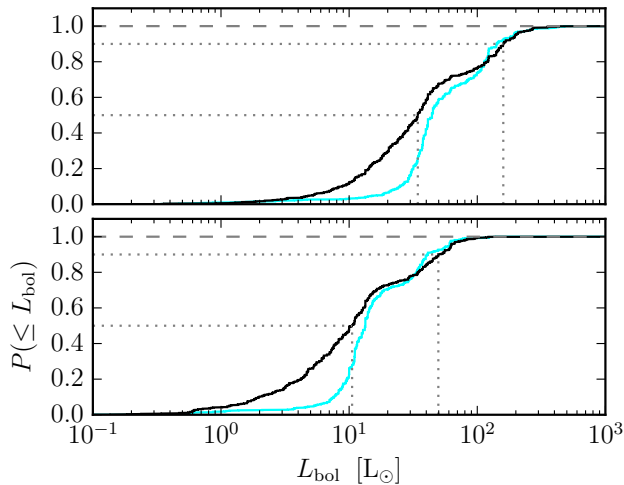


Figure 4. Completeness function for the bolometric luminosity, L_{bol} , of Hi-GAL $70 \mu\text{m}$ sources associated to BGPS clumps in the Distance Catalog (black line). Models from Robitaille et al. (2006) are used to compute L_{bol} . Top: Completeness in high background ($2000 - 3000 \text{ MJy sr}^{-1}$) regions calculated with source detection threshold of 1 Jy . Bottom: Completeness in low background ($500 - 1000 \text{ MJy sr}^{-1}$) regions calculated with source detection threshold of 0.3 Jy . Dotted lines show the 50% and 90% completeness limits and the cyan line shows the completeness function using only DPDFs between $\ell = 28 - 31^\circ$.

carried out by the Arcetri survey (Valdettaro et al. 2001), HOPS (Walsh et al. 2011), and the RMS H_2O Maser Survey (Urquhart et al. 2011). The variability of H_2O masers make multiple catalogs at different epochs complementary for systems that drop below a survey’s sensitivity limits (Furuya et al. 2003). The Arcetri catalog aggregates observations of all known literature H_2O water masers prior to 2001. HOPS is a blind Galactic plane survey with overlap coverage with the BGPS extending to $\ell < 20^\circ$. The HOPS team discovered a number of new H_2O masers not found in the Arcetri catalog, most in the southern sky that is inaccessible to the Arcetri survey. While the survey overlap between HOPS and the BGPS-GBT H_2O maser survey is limited to $10^\circ < \ell < 20^\circ$, it provides valuable context to evaluate the targeted GBT observations. In this range, the GBT observations have a 3.4 times higher detection rate towards BGPS clumps. This is likely due to the tighter beam coupling of the GBT compared to Mopra and the lower baseline RMS for the targeted, single-pointing observing strategy. The GBT observations primarily detect weaker H_2O masers with median integrated intensity $\sim 5 \text{ Jy km s}^{-1}$ compared to HOPS with $\sim 5 \times 10^2 \text{ Jy km s}^{-1}$.

3.3.2. CH_3OH Masers

The 6.7 GHz Class II methanol (CH_3OH) maser is thought to be exclusively associated with high-mass star formation

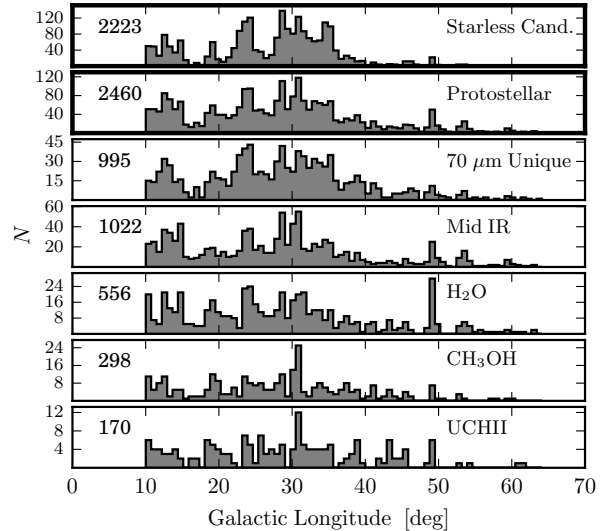


Figure 5. Observed distributions in Galactic longitude for different star formation indicators. The top two panels show the distributions for starless clump candidates and protostar-containing clumps for all BGPS clumps in the overlap region. The bottom five panels are ordered by star formation indicator, ranked by the approximate luminosity of a single protostar that produces the indicator. The number of BGPS clumps in each subset is shown in the upper left. Note that the y-axis scaling is different for each panel.

because of the environments necessary for IR pumping (Breen et al. 2013). A comparison between 6.7 GHz CH_3OH maser emission from the MMB and ATLASGAL $870 \mu\text{m}$ dust emission finds that 99% of MMB sources are associated with ATLASGAL emission indicating that methanol maser emission is almost ubiquitously associated with massive protostellar clumps (Urquhart et al. 2015). We associate BGPS clumps to CH_3OH maser indicators based on available literature data. We use data from the Arecibo CH_3OH survey (Pandian et al. 2007, 2011), the Methanol Multibeam Survey (MMB; Breen et al. 2012b,a, 2014, 2015), and aggregated literature data in Pestalozzi et al. (2005). Within the overlap region, MMB data extends from $10^\circ < \ell < 60^\circ$, Arecibo data extends from $35^\circ < \ell < 54^\circ$, and the data in Pestalozzi et al. (2005) are all-sky targeted observations. Thus there is a small gap in the CH_3OH maser survey data from $60^\circ < \ell < 65^\circ$, but there are only 15 BGPS clumps in this range, so there should not exist a strong sampling bias. While the MMB is the most uniform and complete of the surveys, multiple overlapping datasets are useful because the intensity of CH_3OH masers is time variable. This can be important for masers that drop below the sensitivity limits of a single survey. With multiple surveys at different epochs we create a more complete catalog of CH_3OH masers.

3.4. Radio Continuum – UCHII Regions

UCHII regions are an unambiguous indicator of high-mass star formation because an OB star must be present to internally photoionize the clump. We compare the BGPS with the Coordinated Radio and Infrared Sky Survey for High-Mass Star Formation (CORNISH; Hoare et al. 2012; Purcell et al. 2013) observed with the JVLA in 5 GHz continuum from $10^\circ < \ell < 65^\circ$. We compare all 241 sources classified as UCHII region candidates in Purcell et al. (2013), excluding 43 sources classified as either “HII-Region”, “Diffuse HII-Region”, or “Dark HII-Region”, representative of later stages of evolution. We find 219/243 (90.1%) CORNISH UCHII candidates associated with 170 BGPS clumps. No BGPS clumps are exclusively identified with star formation activity from the CORNISH UCHII region sources. All such clumps are associated with an additional evolutionary indicator: 169 Hi-GAL $70 \mu\text{m}$, 69 mid-IR, 103 H_2O maser, and 70 CH_3OH maser. Urquhart et al. (2013b) compare CORNISH with ATLASGAL and find 213/243 are matched to 170 ATLASGAL clumps. The 24 CORNISH sources classified as UCHII region candidates that are not associated with millimeter continuum emission in the BGPS could potentially be BGPS non-detections, contamination/mis-identification in the CORNISH survey, or more evolved systems that have disrupted most of the surrounding clump.

3.5. Star Formation Indicator Catalog Summary

3.5.1. Star Formation Indicator Statistics

We combine these catalogs of observational indicators of star formation activity into a series of flags to sort clumps into groups for joint analysis of their physical properties. The most basic distinction is between clumps that are associated with no star formation indicators, the “Starless Clump Candidates” (SSC), and “Protostellar” Clumps that are associated to one or more indicator. The star formation indicator groups are then ranked by the approximate luminosity of a single protostar that produces the indicator (see Figure 5). These rankings are a heuristic motivated by proposed linear clump evolutionary sequences (Battersby et al. 2010, 2011; Chambers et al. 2009), but the ordering is settled upon because it consistently yields monotonic trends for clump properties. “ $70 \mu\text{m}$ Unique” are clumps that only contain a Hi-GAL compact source, and thus are candidates for deeply embedded (\approx Class 0/I) protostellar activity. “Mid-IR” clumps are associated to one or more R08 YSO-flagged source, RMS protostellar source, and/or EGO. We group R08, RMS, and EGOS together because they are frequently coincident with the same protostellar sources and they use similar wavelengths to identify activity. “ H_2O ” clumps are associated to one or more H_2O maser from the BGPS GBT survey, Arcetri, and/or HOPS. Similarly, “ CH_3OH ” clumps are associated to one or more CH_3OH masers from Pestalozzi et al. (2005), Arecibo, and/or MMB. “UCHII” clumps are associated to the CORNISH UCHII regions. In section §5 we will use these categories to compare physical properties.

Table 4 lists the detection statistics for sources matched to the BGPS in the overlap region and number of clumps matched to sources. We find that in the common overlap region 2223/4683 (47.5%) are starless candidates and 2460/4683 (52.5%) show some indicator of protostellar activity. This fraction of starless clump candidates is lower than the upper limit of 67% estimated from the ATLASGAL survey by Csengeri et al. (2014) which compare ATLASGAL clumps to WISE $22 \mu\text{m}$ and MSX $21 \mu\text{m}$ point source catalogs. The smaller fraction of starless clump candidates in our analysis

is likely due to the inclusion of protostellar indicators with lower luminosity sensitivity such as *Herschel* $70 \mu\text{m}$ sources in our analysis. The *Herschel* $70 \mu\text{m}$ sources accounts for the largest fraction of star formation indicators detected toward Protostellar clumps (2168/2460 or 88% of Protostellar clumps contain a $70 \mu\text{m}$ source flag). No strong variation in the Galactic longitude distribution is observed between Starless Clump Candidates and Protostellar Clumps (Figure 5). Individual star formation indicator flags for each clump are listed in Table 5.

Except for $70 \mu\text{m}$ Unique, the BGPS indicator groups are not mutually exclusive. Indeed, 70/170 (41%) of UCHII clumps are also associated to a CH_3OH maser and 103/170 (61%) are associated to a H_2O maser. There are no BGPS clumps uniquely associated with H_2O , CH_3OH , or UCHII flags; those clumps are always associated with another protostellar indicator. This fact indicates that it is unlikely that a population of H_2O unique clumps (meaning H_2O masers are the only indicator of star formation activity) exist toward clumps that have been targeted by our GBT observations (§2.2 and §3.3.1). Figure 6 shows the intersection between indicators with the fraction of the total calculated for each. For example, 70 clumps are associated to both CH_3OH masers and UCHII regions: 0.412 (70/170) of those with UCHII regions are also associated to CH_3OH masers, alternatively 0.235 (70/298) of those with CH_3OH masers are also associated to UCHII regions.

Among these indicators the CH_3OH and UCHII clumps are the most consistent indicators of high-mass protostellar activity. However, it is important to note that more extreme indicators of star formation activity do not necessarily represent a later stage in a linear clump evolutionary sequence. For one, not all clumps will have sufficient mass to form an OB star to drive an observable CH_3OH maser or UCHII region. The sequence of star formation indicators outlined in Battersby et al. (2010) is consistent with the expected sequence of observational indicators for a high-mass protostellar core, but BGPS clumps are hierarchical constructs of density, likely composed of multiple cores (Merello et al. 2015). The surveys also do not have high enough resolution to identify single protostellar sources at large distances. For example, what appears to be a Hi-GAL compact source could be a protocluster at several kpc. In this case, the only certain true evolutionary transition is from the starless clump phase to the protostellar phase.

3.5.2. Comparison with Published Starless Clump Catalogs

We compare our protostellar indicator flags to the previously published starless clump catalog of Tackenberg et al. (2012) which identified 210 starless candidates with peak column density $N(\text{H}_2) > 10^{23} \text{ cm}^{-2}$ from ATLASGAL $870 \mu\text{m}$ images in the $10^\circ < \ell < 20^\circ$ range. Tackenberg et al. (2012) use a combination of mid-IR colors from *Spitzer* imaging plus visual analysis of $24 \mu\text{m}$ point sources to identify starless candidates. Within this longitude range, there are 52 BGPS catalog sources with peak positions that lie within the BGPS angular resolution ($33''$) of the Tackenberg et al. (2012) starless candidate position. We find that 30 out of those 52 clumps (58%) contain an indicator of star formation activity in our catalog. Nearly all of those associations result from identification of a $70 \mu\text{m}$ source in our catalog. This result highlights the necessity of far-IR imaging to identify deeply embedded and lower luminosity YSOs.

We also compare to the Traficante et al. (2015a) catalog of 1684 Hi-GAL clumps associated to IRDCs in the $10^\circ < \ell < 55^\circ$ and $|b| \leq 1^\circ$ range. Clumps are extracted

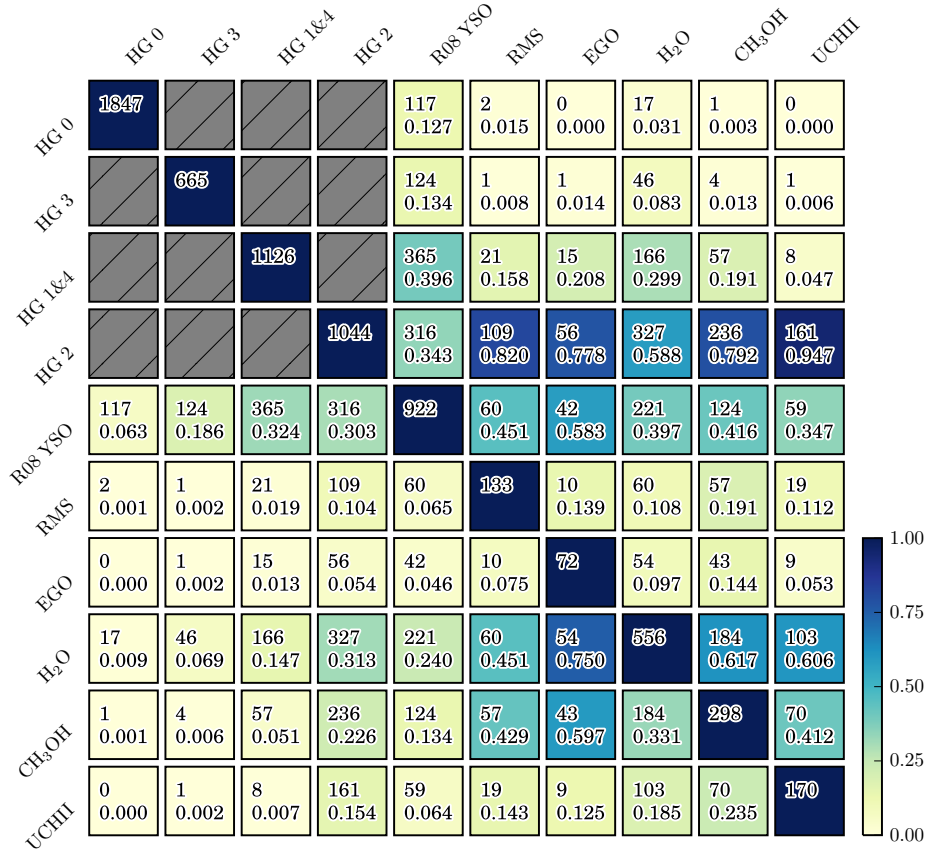


Figure 6. Intersection between pairs of star formation indicators. Totals for each indicator are shown along the diagonal. The top value in each square shows the number of overlapping indicators and the bottom value shows the overlap fraction calculated with respect to the total of the column. The overlap fraction is color-coded by the scale on the right. To read, select the first indicator along the top axis, and drop down to the row of the second indicator along the left axis. The Hi-GAL flags are mutually exclusive for each clump and are grayed out.

from the IRDC catalog of Peretto & Fuller (2009). A novel algorithm (*Hyper*; Traficante et al. 2015b) is used for clump extraction and photometry, and counterparts at 70 μm are used for protostellar identification. When compared by positions, 963 clumps in Traficante et al. (2015a) are associated to 692 BGPS clumps (14.8% of the BGPS clumps in the overlap region), whereas the remaining 721 clumps are not associated. Among the 692 BGPS clumps with associations, 550 (80.3%) star forming categorizations agree and 142 (19.7%) conflict. The conflicts are dominated (109 of 142 conflicts) by cases of a smaller “sub-component” starless clump in the Traficante et al. (2015a) catalog associated to a larger “parent” BGPS clump with a protostellar indicator (N.B. the *Herschel* Hi-GAL resolution at 160 μm is 13.6'' which is 2.4 times higher resolution than the BGPS at 1.1 mm). A minority of 33 (4.8%) BGPS clumps remain that we have classified as starless candidates that contain 70 μm counterparts from the Traficante et al. (2015a) catalog. In these cases we have conservatively assigned Hi-GAL flag 3s (28/33) for ambiguous high-backgrounds in the visual inspection.

4. DETERMINING HELIOCENTRIC DISTANCE

4.1. Distance Probability Density Functions

A radial velocity measurement for Galactic positions within the Solar Circle yields a kinematic ambiguity between a near and far distance. Unique radial velocities are determined from observations of dense gas tracers (HCO^+ , N_2H^+ , or NH_3 ;

Shirley et al. 2013, Dunham et al. 2011b) and from morphological matching the BGPS clumps to the ^{13}CO spectra from the Galactic Ring Survey (GRS; see Ellsworth-Bowers et al. 2014). A Bayesian statistical methodology of formulating clump distance probability density functions (DPDFs) based on a range of prior distributions has been carried out and applied to the BGPS by Ellsworth-Bowers et al. (2013) and Ellsworth-Bowers et al. (2014). Further, to accurately propagate our uncertainty in heliocentric distance, we shall use Monte Carlo random sampling of the DPDFs when calculating the derived physical properties. The DPDF is calculated by multiplying the likelihood function, derived from the measured v_{LSR} with a 7 km/s uncertainty to account for typical GMC dispersion and the Reid et al. (2014) rotation curve of the Galaxy, with prior distributions

$$\text{DPDF}(d_{\odot}) = \mathcal{L}(v_{\text{LSR}}, l, b; d_{\odot}) \prod_i P_i(d_{\odot}, l, b) . \quad (1)$$

The priors are calculated from morphological matching to 8 μm absorption features, latitude offsets compared to the Wolfire et al. (2003) model of the H_2 distribution in the Galaxy, maser parallax measurements, and proximity to an HII region of known distance. The well-constrained DPDFs are defined to have full-width of the 68% maximum-likelihood error bar $\text{FW}_{68} \leq 2.3$ kpc (Ellsworth-Bowers et al. 2013). The total number of well-constrained DPDFs is 1710 in the BGPS survey.

4.2. Distance Resolution Broadcasting

The well-constrained BGPS distance sample contains 1414 clump DPDFs representing 43% of the BGPS velocity catalog in $10^\circ < \ell < 65^\circ$. Clumps show an easily distinguishable tendency to cluster in velocity coherent groups. Indeed, 75.4% of clumps in the overlap region have at least one adjacent neighbor (i.e., pixels touching) in the `Bolocat` label-masks. Clumps that are within spatial and kinematic proximity are more likely to be cospatial than chance alignments of non-cospatial near/far kinematic distances. In order to increase the size of the Distance Sample, we apply a modified Friends-of-Friends algorithm (Huchra & Geller 1982) to associate or “broadcast” the known DPDFs based on whether clumps are nearby in $(\ell, b, v_{\text{LSR}})$ or position-position-velocity (PPV) space. Because this technique uses only proximity in PPV-space, the number of new associations does not have a strong selection effect from evolutionary stage or physical properties. To evaluate the optimal search angle-velocity search parameters, we use the Distance Sample as a training set, and minimize the fraction of near/far misassociations.

We assign a clump to a “PPV-group” or “group” by searching a distance ρ around the clump in angular separation, θ_s , and velocity, v_s :

$$\rho = \sqrt{\Delta\theta^2 + \left(\frac{\theta_s}{v_s} \Delta v\right)^2} < \sqrt{2}\theta_s \quad (2)$$

Clumps within this neighborhood are assigned to a parent group and the group is iteratively expanded by searching around the neighbors. This algorithm effectively creates groups out of a minimum density in PPV-space. We calculate group assignments over a 30×30 grid of angular search and velocity search radii from $\theta_s = 1.8 - 10.5'$ and $v_s = 1 - 6 \text{ km s}^{-1}$. We use the known maximum likelihood distances as a training set to evaluate the accuracy of the search parameters. We denote the conflict ratio, R_{conf} , as the number of clumps in groups with disagreeing distance resolutions divided by the number of clumps in groups with at least two distance resolutions. With R_{conf} as a figure of merit, we select the search parameters that maximizes the number of new distance resolutions for fixed R_{conf} . It is important to note however that the DPDFs are not simply Boolean near/far kinematic distance resolutions. Thus, R_{conf} can only be approximately as low as the mean weight between the near/far probabilities in the DPDFs. (Ellsworth-Bowers et al. 2013) find that 8% of the DPDFs disagree with the ^{13}CO Galactic Ring Survey kinematic distance ambiguity resolutions (KDARs) from Roman-Duval et al. (2009) using HI self-absorption (HISA). We fix the conflict ratio to be reasonably consistent with this figure at $R_{\text{conf}} = 0.12$ and select the search parameters $(\theta_s, v_s) = (3.9', 4.0 \text{ km s}^{-1})$ that maximize new associations. In total, we associate 446 new DPDFs over the full survey, and 226 in the survey overlap region. The KDA resolution broadcasting method thus increases the Distance Sample used in this study by 226 (16%) to 1640 clumps in the overlap region.

The DPDFs added to the Distance Sample are constructed from the weighted priors of the DPDFs within the group. The optimized search parameters are used to associate the neighboring clumps in the group to a common kinematic near/far distance. To create a new posterior DPDF for a clump in a group, we apply a weighted average of all priors from the clumps in the group with a DPDF to the the new group-member

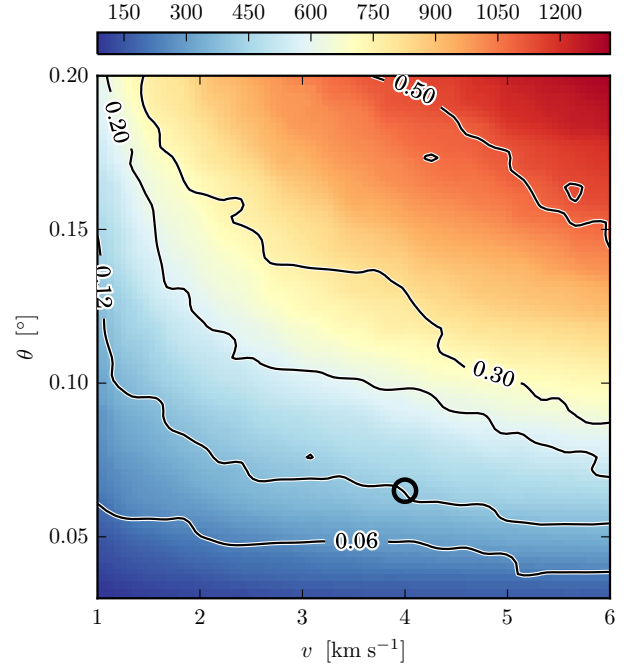


Figure 7. Optimization of the velocity and angular search parameters for the number of new clump KDA resolutions (color-scale). The new KDA resolutions are in PPV-groups with one or more resolved KDA member that have a well-constrained DPDF. Black contours show the conflict ratios R_{conf} , or the ratio of clumps in PPV-groups with conflicting Near/Far KDA resolutions to the total number of clumps in PPV-groups with two or more distance-resolved members. Maximizing the number of new KDAR associations for a fixed $R_{\text{conf}} = 0.12$ gives 446 new distance resolutions at $\theta = 0.065^\circ$ ($3.9'$) and $v = 4.0 \text{ km s}^{-1}$ (black circle).

clump. The priors are given Gaussian weights by the PPV-distance ρ with FWHM values set to the optimized θ_s and v_s above. This weighting ensures that the closest clump priors in the group are most strongly weighted. To propagate our uncertainty in broadcasting the distance resolution of an individual clump, we apply a weighted error function (as a step-function analogue) to the new posterior DPDF to account for $R_{\text{conf}} = 0.12$. Down-weighting the distance resolutions by the conflict fraction accounts for the mean uncertainty in the group associations.

4.3. Distance Comparisons

Dunham et al. (2011b) used a combination of visually identified $8 \mu\text{m}$ absorption features and HI self-absorption (HISA) to resolve the kinematic distance ambiguity (KDA) towards a sample of BGPS clumps. Because these sources are also in our sample, we compare the distance resolutions in Dunham et al. (2011b) with the resolutions of the well-constrained DPDFs in Ellsworth-Bowers et al. (2013) and Ellsworth-Bowers et al. (2014). The results of Dunham et al. (2011b) are based on the BGPS v1.0 data release and are assigned to BGPS v2.0 sources by mapping the peak flux positions of the v1.0 sources onto the v2.0 source masks. Of the 456 sources with resolved distances in Dunham et al. (2011b), 403 match to v2.0 sources and 100 have well-resolved KDAs in our sample. For sources flagged as either “near” or “tangent” in Dunham et al. (2011b), we find that $69/78 \approx 88\%$ agree. For sources flagged as “far” that had no incidence of an $8 \mu\text{m}$ absorption feature nor HISA, we find that only $11/20 \approx 53\%$ agree.

The lack of an HISA feature is commonly used to associate

GMCs to the far kinematic distance (Roman-Duval et al. 2010), where the superposition against the background HI distribution produces absorption at the velocity coincident with the high-column density present in the GMC. The clumps found in the BGPS are both on smaller spatial scales and at higher spatial densities than GMCs. The disagreement for far distance resolutions for clumps is because the HI distribution does not follow that of the clump dust continuum, and thus the lack of a HISA feature can not be used to accurately resolve the kinematic distance ambiguity for BGPS clumps.

Wienen et al. (2015) use associations of ^{13}CO GRS isocontours in PPV-space and the associated HI absorption with those GRS clouds to resolve 44% of ATLASGAL clumps to the far kinematic distance. This is twice the 22% fraction found in Ellsworth-Bowers et al. (2014). Comparison of the Wienen et al. (2015) KDA resolutions with Ellsworth-Bowers et al. (2014) DPDFs indicate a 30% conflict fraction. The origin of the larger conflict fraction is the larger PPV spaces used to associate objects in the Wienen et al. (2015) paper. Figure 7 shows that the conflict fraction increases with angular separation and velocity for larger PPV groups. This result combined with the larger number of far kinematic resolutions will systematically skew distributions of physical properties such as M , R , n , and $\langle t_{\text{ff}} \rangle$ to larger values for the Wienen et al. (2015) sample.

5. ANALYSIS OF PHYSICAL PROPERTIES WITH STAR FORMATION INDICATORS

In the following subsections, we shall compare and analyze observable and physical quantities for both the starless clump candidates and protostellar clumps. For the protostellar clumps, we sort clumps by their star formation indicators into subsamples described in §3.5. As noted in §3, this ordering is not an evolutionary sequence but is roughly ordered by the typical luminosity required to produce each indicator. In the following figures, the top two panels indicate the starless clump candidate and protostellar candidate subsamples while subsequent panels indicate various star formation indicator subsamples. For the physical properties and sampling techniques described below, Table 6 lists the derived physical properties and uncertainties for each clump in the Distance Sample, and Table 7 lists the statistical properties and uncertainties for subsamples of clumps sorted by star formation indicator.

5.1. Monte Carlo Sampling

For each subsample we compute Monte Carlo (MC) simulations to randomly sample all of the input parameters, both measured quantities with statistical uncertainties (e.g., S_ν , T_{K}) and DPDFs. By calculating descriptive statistical quantities (e.g., $\mu_{1/2}$, ρ_{spear}) from suites of MC simulations, we can estimate the uncertainty and significance of comparisons between samples of clumps associated with different star formation indicators. The suites of MC simulations also more accurately propagate the uncertainties when compared to simply creating a single histogram of the maximum likelihood values, because some quantities such as heliocentric distance can have highly asymmetric and/or bimodal PDFs. Thus, while a single clump may have large fractional uncertainties in any given derived physical property, we can make robust and accurate calculations for large ($\sim 10^2 - 10^3$), statistically significant subsamples of clumps.

5.1.1. AGB Contamination Re-sampling

Contamination from AGB stars is a significant source of uncertainty when the only indicator of star formation activity within a clump is from the mid-infrared colors of a point source. In order to propagate this uncertainty due to AGB contamination, we re-sample flags discriminating between R08 YSOs and AGBs sources in the MC simulations. We use conservative estimates of the contamination fractions between the R08 YSO contaminants in the AGB classification and AGB contaminants in the YSO classification. As described in §3.2.2, we apply contamination fractions of 40% for AGB sources and 50% for YSO sources. All R08 sources within clumps are re-sampled this way. If a clump is associated to another star formation indicator besides R08, then it is still flagged as protostellar and the MC flag re-sampling will not affect the clump’s overall designation. In the overlap region, only 280 clumps (6.0%) are uniquely associated with R08 sources, and 122 clumps (7.4%) in the Distance Sample. Re-sampling propagates our uncertainty in the R08 flags, but because of significant coincidence with other star formation indicators, it introduces only a minor effect in discriminating between starless clump candidates and protostellar clumps. In the following analysis, AGB contamination re-sampling is used in all MC calculations.

5.1.2. DPDF Sampling and Distance Biases

For the calculation of quantities which are distance dependent (e.g., R , M), we draw the heliocentric distance from the source DPDF. Each MC simulation consists of 10^4 random draws. Since the output distributions of the physical properties may be skewed, we use robust statistical indicators such as the median ($\mu_{1/2}$) and median absolute deviation ($\sigma_{1/2}$)¹² as conservative characterizations of the distribution of properties for a particular subsample.

Before we compare physical properties among clumps with different star formation indicators (§5.2-5.4), we compare the distribution of DPDFs for each star formation indicator subsample defined in §3.5. Figure 8c shows the mean distribution or average DPDF for each indicator. The indicator categories show similar distributions of heliocentric distance. While the number of clumps associated with each indicator vary, the range and distribution of d are similar, with medians between 4.4 – 5.1 kpc. As a result, physical properties which depend linearly or quadratically on distance will not be strongly biased by the underlying distance distribution for each indicator subsample. Sources with associated CH_3OH masers and/or UCHII regions show a relative deficit of distances from 2 – 4 kpc. This could be an effect from the method of resolving distances with the $8 \mu\text{m}$ absorption prior, where better spatially resolved clumps at the near distance are dominated by mid-IR emission from a high-mass YSO. These regions may not have the necessary contrast in the GLIMPSE $8 \mu\text{m}$ maps to result in a well constrained distance estimate, whereas further, and thus larger, clumps could have sufficient surrounding $8 \mu\text{m}$ absorption. In addition, the PPV method of associating nearby clumps with known distances for a fixed radius in angle and a fixed velocity better associates regions at larger distances where the angular separation between clumps is smaller.

When comparing distance independent quantities between starless candidate and protostellar categories, the total number of sources is nearly equal (2223 SCCs vs. 2460 protostar-

¹² The median absolute deviation is defined by $\sigma_{1/2} = \mu_{1/2,i}(|X_i - \mu_{1/2,j}(X_j)|)$ for a univariate dataset X . For normally distributed data, $\sigma_{1/2}$ is related to the standard deviation by $\sigma \approx 1.48260\sigma_{1/2}$.

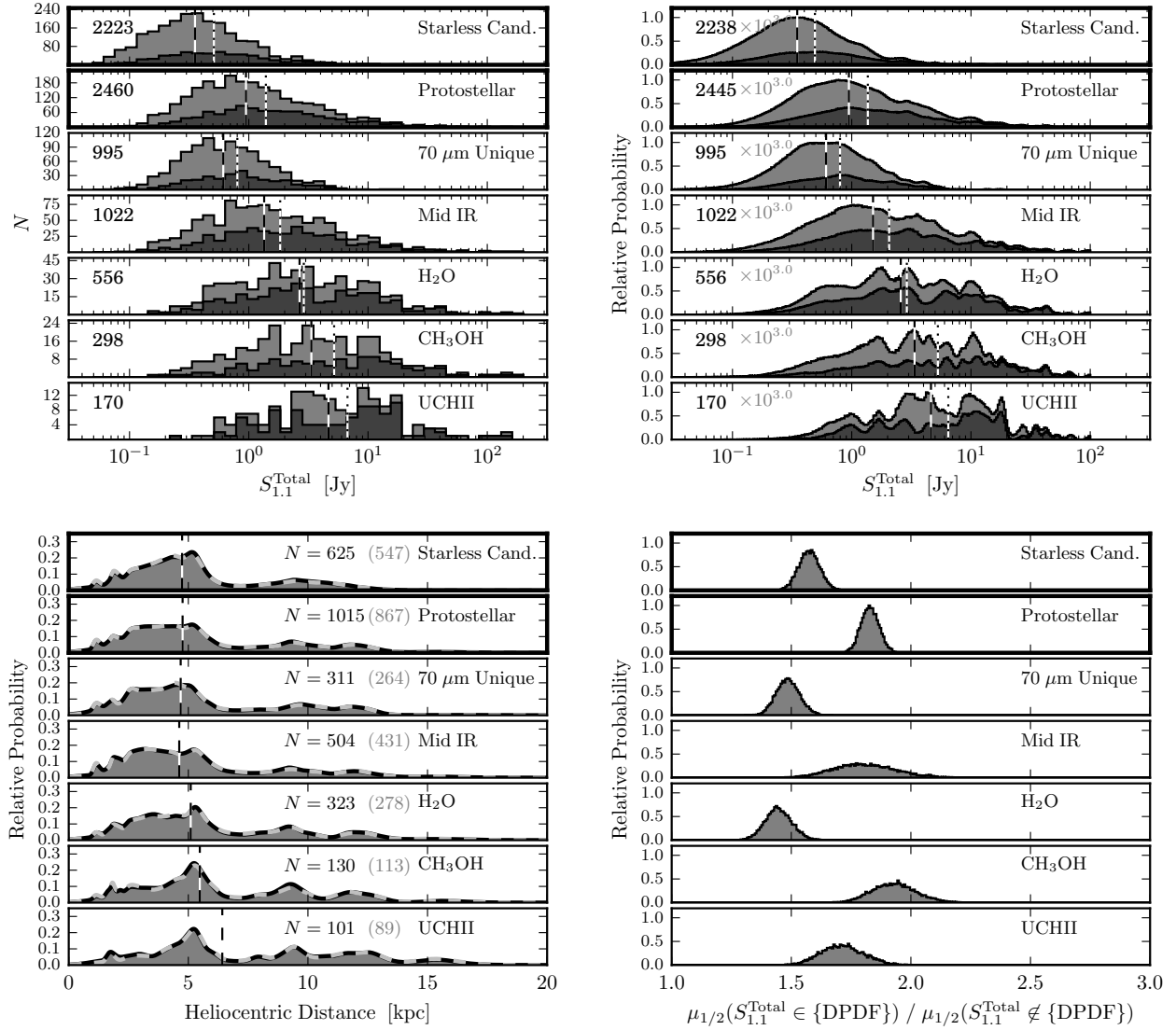


Figure 8. Distributions of total flux density for clumps in the full sample (light gray) and Distance Sample (dark gray) by star formation indicator. Top left: flux density histogram of observed values. Top right: flux density distribution drawn from MC simulation. Bottom left: average DPDF for the expanded DPDF sample (black line) and original DPDF sample (dashed gray line). The number N of the clumps are shown in black and gray, respectively. Bottom right: ratio of median total flux density of clumps with a DPDF to clumps without a DPDF. Clumps in the Distance Sample have a factor of $\sim 1.5 - 2.0$ higher median flux density than clumps not in the Distance Sample. The star formation indicator is shown in the upper-right of each panel.

containing clumps); however, when comparing distance dependent physical properties, it should be noted that in the Distance Sample there are 1.675 times as many protostellar-containing clumps than starless clump candidates (613 SCCs vs. 1027 protostellar clumps). The fraction of clumps in the Distance Sample that contain at least one star formation indicator is shown as a function of heliocentric distance in Figure 9. The median protostellar clump fraction in the Distance Sample is 0.60, and there is no significant trend in this ratio out to heliocentric distances of 12 kpc. Since only 58 clumps (3.5%) in this study have maximum likelihood distances greater than 12 kpc, this result indicates that differences in the properties of starless candidates compared to protostellar clumps are not driven by a bias in the protostellar fraction by distance.

We can only calculate distance-dependent quantities from the subset of clumps in each category of the Distance Sample. We run MC simulations for both the subsamples that have a well-constrained DPDF and those without to test how

this selection criteria may bias our distributions. Figure 8a shows the observed total flux density $S_{1.1}^{\text{Total}}$ for each indicator, with the total sample (light gray) and Distance Sample (dark gray). Figure 8b shows the cumulative results of 10^4 draws from the Monte Carlo simulation of the 1.1 mm flux density Gaussian-deviates and R08 AGB contamination re-sampling. The subsamples with DPDFs have greater median $S_{1.1}$ when compared to full samples. Similarly, figure 8d shows the distribution of the ratio of medians for each MC simulation. All indicator categories show a factor of 1.5 – 2.2 higher median flux for clumps with DPDFs; however, there is not a consistent trend in the ratio between star formation indicators. The ratio of median flux densities for protostar-containing clumps is only a factor of 1.1 – 1.2 times larger than the corresponding ratio for starless clump candidates. If we make the simple assumption that starless sources without well constrained DPDFs follow the average DPDF distributions for the Distance Sample, then this result implies that physical quantities that depend linearly

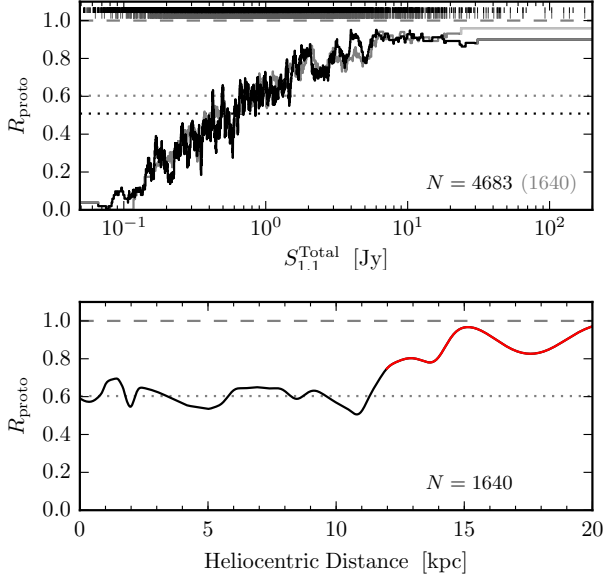


Figure 9. Protostellar fraction distributions, computed using the MC simulations. *Top:* Total flux density. The black line shows R_{proto} for a moving window of 50 sources over the full overlap sample and the Distance Sample is shown in gray. Vertical lines show the clump $S_{1.1}^{\text{Total}}$ values. *Bottom:* Heliocentric distance. The solid line shows R_{proto} computed as a weighted sum of the DPDFs. R_{proto} is approximately constant at < 12 kpc, suggesting that the star formation indicators are mostly complete for BGPS clumps. In red are the 58 clumps with $d_{\text{ML}} > 12$ kpc that compose 3.5% of the Distance Sample. Sample protostellar fractions are shown by horizontal dotted lines.

on flux density (i.e., mass) are biased by factors of 1.5 – 2.2 larger in the Distance Sample versus the total sample.

5.2. Flux Density, Flux Concentration, and Size

The observed 1.1 mm flux densities increase towards more extreme indicators from starless clump candidates to UCHII associated clumps (Fig. 8a). The median total 1.1 mm flux density of starless clump candidates is 0.356 ± 0.005 Jy and is a factor of 15 lower in total flux density compared to the median for UCHII associated clumps. The starless candidate and UCHII associated clump distributions are distinct where 99% of starless candidates have lower total 1.1 mm flux density than the median total flux of UCHII associated clumps. Even the presence of a deeply embedded YSO observed as a compact Hi-GAL $70 \mu\text{m}$ source preferentially increases the median observed flux density by a factor of ~ 1.8 . Figure 9 shows these trends in an alternative way as a strongly increasing protostellar clump fraction with increasing 1.1 mm flux density. The ratio crosses 0.5 around 500 mJy and approaches 1.0 above 5 Jy. Without internal star formation activity, starless clumps would only be externally heated by the interstellar radiation field (ISRF; Evans et al. 2002, Jørgensen et al. 2006, Wilcock et al. 2012). As a result, clumps with weaker internal heating will have colder dust temperatures and lower observed 1.1 mm flux densities (see §5.3).

The deconvolved clump equivalent angular radius θ_{eq} is calculated by subtracting the BGPS beam $\theta_{\text{HPBW}} = 33''$ ($\Omega_{\text{beam}} = 1234$ sq. arcsec) in quadrature from the observed equivalent angular radius $\theta_{\text{obs}} = \Omega_{\text{obs}}/\pi$ calculated directly from the sum of the $7.2'' \times 7.2''$ map pixels in the Bolocat label-mask frames

$$\theta_{\text{eq}} = \sqrt{\frac{\Omega_{\text{obs}}}{\pi} - \frac{\Omega_{\text{beam}}}{\pi}}, \quad (3)$$

where Ω_{obs} is either the total solid angle defined by the Bolocat v2.0 seeded watershed algorithm or the FWHM solid angle defined by the contour at half-maximum flux density. Quantities that are derived from the Bolocat label-masks of the BGPS maps are sensitive to the spatial filtering imposed by the principal component analysis performed on the Bolocat time stream data. A clump size based on the FWHM definition is more robust to spatial filtering and is also more prevalent in the literature (e.g., Beuther et al. 2002; Shirley et al. 2003). In the following analyses, we shall use both total size definition, i.e., the full label masks, as well as the FWHM size definition to calculate derived properties.

Figure 10a shows Ω^{Total} for each indicator, with an increasing trend in the distributions with median 3.62×10^3 square arcsec (1.01 square arcmin) for the starless candidates to 1.81×10^4 square arcsec (5.03 square arcmin) for the UCHII associated clumps. There is also a systematically increasing trend in the concentration of the 1.1 mm flux density distributions when sorted by indicator. Figure 10b shows the ratio in deconvolved solid angles, or Total to FWHM “concentration”, defined as $\Omega^{\text{Total}}/\Omega^{\text{FWHM}}$. Clumps that are near uniform brightness and with a peak brightness less than twice the 1σ ($\sim 0.1 - 0.5$ Jy) cut-off threshold of the clump boundaries should have concentrations near unity, while clumps with highly concentrated brightness distributions will have large concentration values ($\gg 1$). A strong increasing trend is seen from a median ratio $\Omega^{\text{Total}}/\Omega^{\text{FWHM}}$ for the starless candidate phase at 1.55 to 16.38 for UCHII clumps. Clumps associated with H_2O masers, CH_3OH masers, and UCHII regions are concentrated at similar levels and also more concentrated than those with less extreme indicators.

The equivalent physical radius R_{eq} is calculated from the observed Ω when projected to a heliocentric distance d_{\odot} drawn from the DPDFs

$$R_{\text{eq}} = 0.29 \left(\frac{\theta_{\text{eq}}}{\text{arcmin}} \right) \left(\frac{d_{\odot}}{\text{kpc}} \right) \quad (4)$$

Figure 11 shows the equivalent radius distributions for the Total (11a) and FWHM (11b) definitions. The median $R_{\text{eq}}^{\text{Total}}$ increases from 0.842 ± 0.017 to 2.66 ± 0.08 pc from starless candidates to UCHII clumps; however, little separation among different indicators is observed using the FWHM definition with median $R_{\text{eq}}^{\text{FWHM}} \sim 0.6$ pc. The $R_{\text{eq}}^{\text{Total}}$ in this study are larger than those found by Schlingman et al. (2011) (median $R_{\text{eq}} = 0.75$) for a subset of known 529 sources taken from the BGPS v1.0. This discrepancy can be attributed to the recovery of flux at lower spatial frequencies in the BGPS v2.0 maps resulting in larger clumps (Ginsburg et al. 2013). The different trends observed between the total source size and FWHM size are more striking and can be explained by offsetting factors. Clumps containing indicators of more luminous protostars (i.e., CH_3OH masers, UCHII) have the highest flux concentrations which partially offset their larger total solid angle resulting in their FWHM sizes remain nearly the same on median as starless clump candidates and clumps with lower luminosity protostellar indicators. This result highlights the need to explore multiple size definitions in the analysis of source physical properties.

5.3. Gas Kinetic Temperature and Linewidth

NH_3 is an excellent intermediate to dense gas tracer with an effective excitation of $\sim 10^3 \text{ cm}^{-3}$ for the lowest pure inversion transition (Shirley 2015). Fitting the intensities of the lowest energy inversion transitions provide estimates of

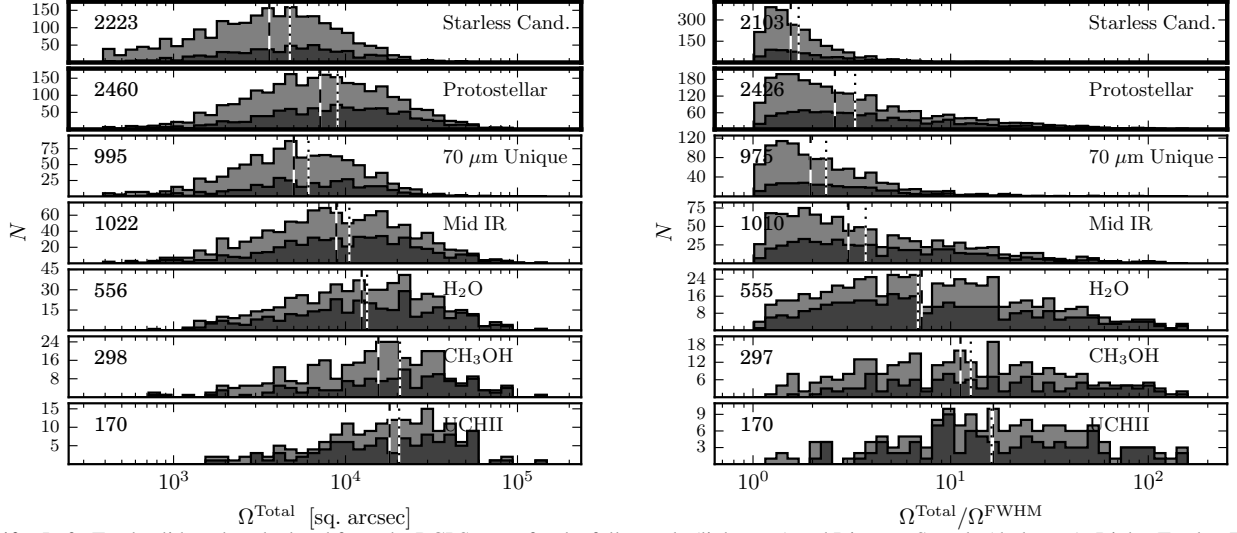


Figure 10. Left: Total solid angle calculated from the BGPS maps for the full sample (light gray) and Distance Sample (dark gray). Right: Total to FWHM concentration. The FWHM size is calculated for the extent of the emission above the half-max. Starless candidate clumps tend to have flux that is less extended and less concentrated than more extreme indicators.

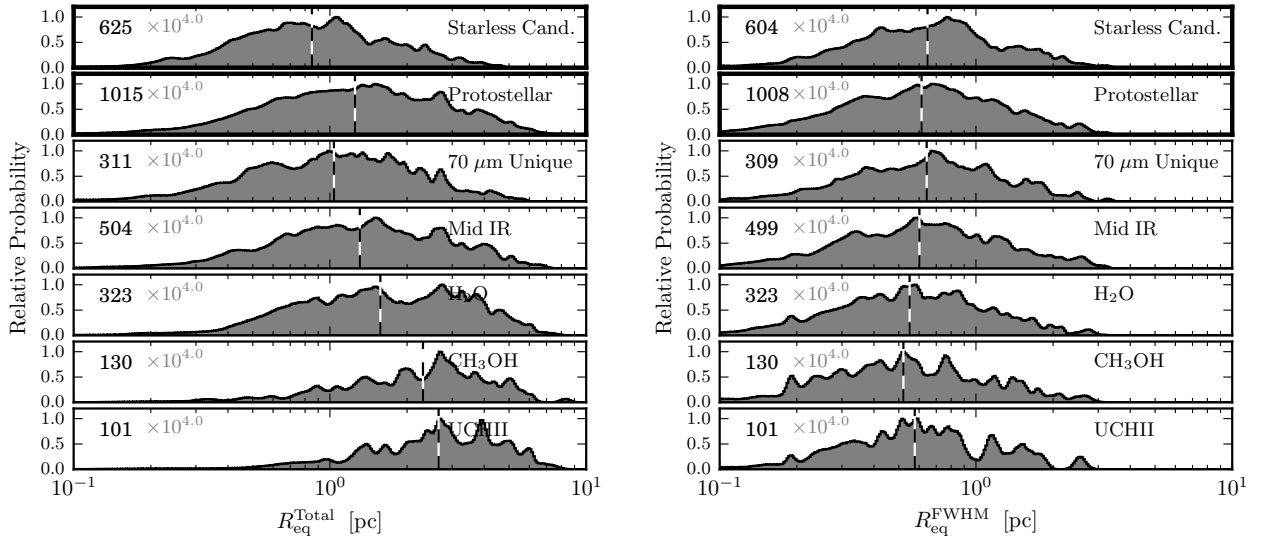


Figure 11. Physical equivalent radius histograms from the MC simulations for each star formation indicator sample. Left: Physical total radius. Right: Physical FWHM radius. The dashed lines show the median value and the number of clumps in the subsample is shown in the upper left.

the gas kinetic temperature (Ho & Townes 1983). The rotation temperature of the (1,1) and (2,2) p-NH₃ inversion transitions saturates for $T_K > 30$ K, but the simultaneously observed (3,3) transitions retain sensitivity to $T_K < 100$ K if the o-NH₃ (3,3) transition is not masing (Danby et al. 1988). Figure 12 shows the distributions of NH₃-derived gas kinetic temperature with values ranging between $T_K \sim 10 - 100$ K. The starless candidate phase has a median $T_K = 13.96 \pm 0.10$ K with an increasing trend to $T_K = 27.2 \pm 0.2$ K for UCHII clumps. The clumps uniquely associated with compact Hi-GAL $70\ \mu\text{m}$ sources, a sign of deeply embedded protostellar activity, show only a slight enhancement in the gas kinetic temperature. As a clump evolves from a quiescent phase to one with active star formation, radiative heating from star formation is expected to raise the gas kinetic temperature. With more extreme indicators of star formation activity suggesting higher luminosity YSOs, the CH₃OH and UCHII region containing clumps are subject to stronger radiative heating from massive star formation. The

starless clump candidate distribution does display a positive skew. This could be a result of undetected embedded sources or enhancement by the local radiation field from neighboring star forming regions. The lower $S_{1.1}$ in the candidate starless clump stage shown in Figure 8 can, in part, be attributed to this observed trend in T_K . The flux density of a modified blackbody is 4.9 times higher at $T_K = 30$ K than 10 K at 1.1 mm. We shall account for the temperature differences observed among the different star formation indicators in our calculations of the clump mass in §5.4.

The observed FWHM linewidths of NH₃ for clumps may be broadened due to a variety of factors including thermal broadening, bulk motion, optical depth, and turbulence. In the following analysis we use the NH₃ rather than HCO⁺ linewidth because the NH₃ observations have three times better spectral resolution, $0.3\ \text{km s}^{-1}$, and NH₃ has lower optical depths, $\tau_{\text{NH}_3(1,1)} \sim 1 - 5$ compared to $\tau_{\text{HCO}^+(3-2)} \sim 10$ (see Shirley et al. 2013). Figures 12b shows the distributions of ob-

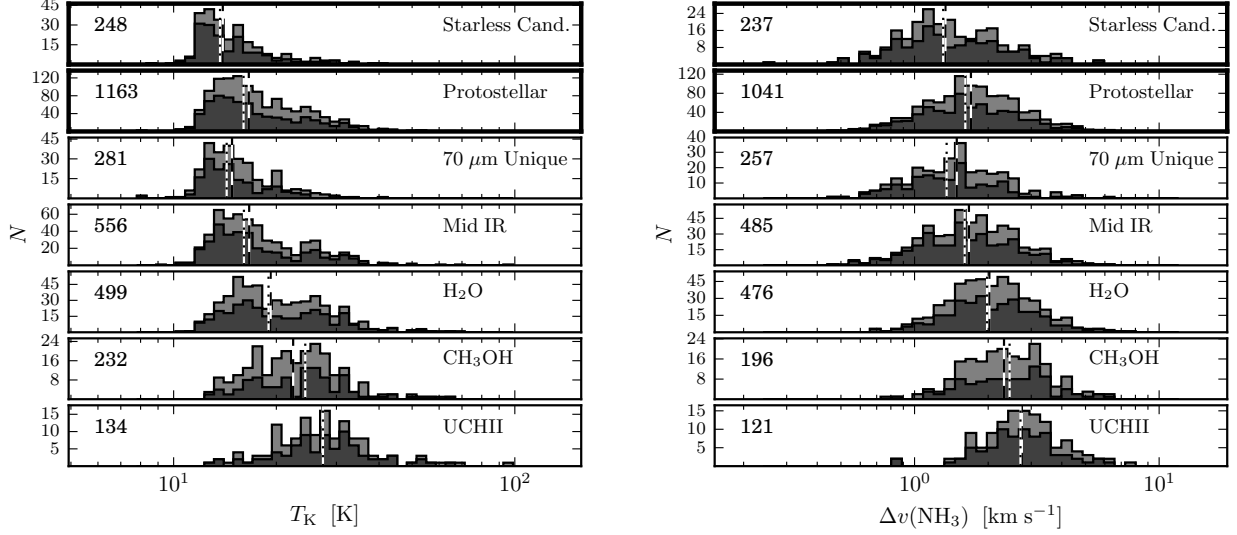


Figure 12. Observed distributions of NH_3 -derived kinetic temperature (Left) and linewidth (Right) by star formation indicator. The dashed lines show the median value and the number of clumps in the subsample is shown in the upper left.

served NH_3 linewidth, indicating a factor of two increase from $1.339 \pm 0.014 \text{ km s}^{-1}$ on median towards starless candidates to $2.736 \pm 0.03 \text{ km s}^{-1}$ on median towards UCHII associated clumps. For gas temperatures between $10 - 30 \text{ K}$ the thermal linewidth is $\Delta v_{\text{therm}}(\text{NH}_3) = 0.16 - 0.28 \text{ km s}^{-1}$. The observed NH_3 linewidths at $> 1 \text{ km s}^{-1}$ suggest supersonic turbulence exists on scales smaller than the $33''$ beam of the BGPS. The quiescent starless candidate phase and the deeply embedded candidate phase of uniquely identified Hi-GAL $70 \mu\text{m}$ compact sources have $\Delta v_{\text{turb}}/\Delta v_{\text{therm}} \sim 10$. The observed increase in linewidth with more extreme star formation indicators could be due to an increase in turbulent feedback in more luminous protostellar clumps. More luminous protostars will drive more powerful jets and outflows (see Bontemps et al. 1996) as well as provide more radiative feedback on the surrounding clump that can drive turbulence (see Krumholz & Thompson 2012). Alternatively, the larger linewidths towards clumps with more extreme indicators could be due to larger bulk-flow motions that are unresolved at the GBT angular resolution or a systematic tendency for higher mass stars to form in more turbulent regions. Without higher resolution observations of the clumps, it is difficult to determine which scenario drives the observed trend.

Prior observations of a significantly smaller subsample of BGPS clumps have indicated a breakdown in the linewidth-size relationship (Schlingman et al. 2011). We plot the linewidth-size relationship for SCCs and protostellar clumps observed in NH_3 , shown in Figure 13. The Spearman’s rank correlation coefficients for SCCs and protostellar clumps are $\rho_{\text{sp}} = 0.24$ and $\rho_{\text{sp}} = 0.50$ respectively from the MC simulations. The starless clumps appear uncorrelated while protostellar clumps have a weak correlation that is only marginally better than the Schlingman et al. (2011) correlation ($\rho_{\text{sp}} = 0.40$). SCCs, as traced by NH_3 emission, seems to have decoupled from the supersonic scaling relationship observed toward molecular clouds more so than protostellar clumps. Indeed the observed NH_3 model-fit velocity dispersion (expressed as FWHM linewidth) are below the extrapolated relationship observed by Larson (1981) for molecular clouds traced by CO 1 – 0. While these clumps themselves are still turbulent structures, their level of turbulence appears dissipated compared to the expected relationship

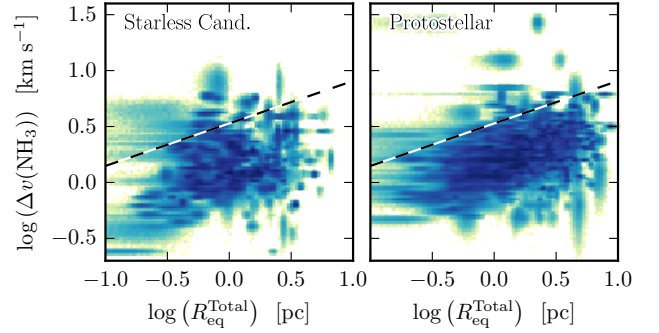


Figure 13. Linewidth-size relationship plotted for starless clump candidates (Left) and protostellar clumps (Right) drawn from MC simulations of each quantity. The protostellar clumps have a higher Spearman rank correlation coefficient $\rho_{\text{sp}} = 0.50$ than the starless clump candidates $\rho_{\text{sp}} = 0.24$. The dashed line indicates the converted relationship $\Delta v = 3.37 \text{ km s}^{-1} (R/\text{pc})^{0.38}$ observed in Larson (1981) for molecular clouds traced by CO 1 – 0.

in clouds when observed on clump spatial scales.

5.4. Mass Calculations

5.4.1. Mass Surface Density

The mean mass surface density is calculated using:

$$\Sigma_{\text{H}_2} = \frac{S_{1.1}}{B_{1.1}(T_{\text{dust}})\kappa_{1.1}\zeta} \frac{1}{\Omega} \quad (5)$$

where $B_{1.1}$ is the Planck function, $\kappa_{1.1}$ is the dust opacity, ζ is the dust-to-gas ratio, here assumed to be $1/100$, and Ω is the source solid angle, and $S_{1.1}$ is the source integrated flux density. Both the Total and FWHM size definitions are used for Ω or $S_{1.1}$. We assume the 1.1 mm emission is optically thin and use Gaussian-deviates to sample the statistical uncertainty. We also assume OH5 dust opacities calculated for coagulated grains with thin ice mantles (Ossenkopf & Henning 1994). For the Monte Carlo calculation, we draw Gaussian-deviates from the observational uncertainty on T_{K} , and assume that the dust temperature is equal to the gas kinetic temperature. Because 47% (772/1640) of clumps with a distance lack T_{K} measurements, for those clumps we draw T_{K} from that indicator’s observed distribution of T_{K} (Fig. 12a). This takes into

account the trend of increasing gas T_K for clumps associated to more extreme star formation indicators. For clumps associated with multiple star formation indicators, the indicator with the hottest median T_K is used.

Figure 14 shows $\Sigma_{\text{H}_2}^{\text{Total}}$ with an increasing trend towards higher $\Sigma_{\text{H}_2}^{\text{Total}}$ for clumps associated to more extreme star formation indicators. The median $\Sigma_{\text{H}_2}^{\text{Total}}$ increases from median values $\Sigma_{\text{H}_2}^{\text{Total}} = 0.0145 \pm 0.0002 \text{ g cm}^{-2}$ and $\Sigma_{\text{H}_2}^{\text{FWHM}} = 0.0165 \pm 0.0003 \text{ g cm}^{-2}$ for the starless candidate clumps to $\Sigma_{\text{H}_2}^{\text{Total}} = 0.0207 \pm 0.0005 \text{ g cm}^{-2}$ and $\Sigma_{\text{H}_2}^{\text{FWHM}} = 0.076 \pm 0.002 \text{ g cm}^{-2}$ for the UCHII associated clumps. A similar trend in increasing column density from quiescent (potentially starless) clumps to protostellar clumps has also been observed by other (sub)millimeter Galactic plane surveys (see Csengeri et al. 2014; Guzmán et al. 2015).

The factor of four increase in $\Sigma_{\text{H}_2}^{\text{FWHM}}$ is consistent with the greater flux densities and flux concentrations observed towards clumps with more extreme indicators. The median mass surface density for protostellar sources is close to the purported threshold for star formation of approximately $120 M_\odot \text{ pc}^{-2}$ (or 0.025 g cm^{-2} ; Lada et al. 2010; Heiderman et al. 2010). Since half of these clumps presumably contain protostellar sources despite being below this threshold, this result highlights that BGPS clumps themselves contain significant substructure which are at higher mass surface densities.

5.4.2. Clump Mass

We calculate total clump masses with:

$$M_{\text{H}_2} = \frac{S_{1.1} d_{\text{ML}}^2}{B_{1.1}(T_{\text{dust}})\kappa_{\text{dust},1.1}\zeta} \quad (6)$$

$$\approx 13.1 \left(\frac{e^{13\text{K}/T_{\text{dust}}} - 1}{e^{13\text{K}/20\text{K}} - 1} \right) \left(\frac{S_{1.1}}{1 \text{ Jy}} \right) \left(\frac{d_{\text{O}}}{1 \text{ kpc}} \right)^2 M_\odot$$

Figure 15 shows the distributions of $M_{\text{H}_2}^{\text{Total}}$ when sorted by indicator from 10^4 MC simulations that account for R08 AGB catalog contamination and uncertainties in $S_{1.1}$, T_K (or randomly drawn from the appropriate T_K distribution if no T_K observations exists), and the DPDFs. The masses show a systematic increase from $\mu_{1/2}(M_{\text{H}_2}) = 226 \pm 11 M_\odot$ for SCCs and $\mu_{1/2}(M_{\text{H}_2}) = 600 \pm 20 M_\odot$ for protostellar clumps. Among the clumps associated to star formation indicators, the masses increase from $\mu_{1/2}(M_{\text{H}_2}) = 390 \pm 30 M_\odot$ for the 70 μm Unique category to $\mu_{1/2}(M_{\text{H}_2}) = 2600 \pm 200 M_\odot$ for the UCHII category. The difference in median masses between the SCC and Protostellar categories of $\Delta\mu_{1/2}(M_{\text{H}_2}) = 370 \pm 20 M_\odot$ and the SCC and 70 μm Unique category of $\Delta\mu_{1/2}(M_{\text{H}_2}) = 170 \pm 30 M_\odot$. The median mass difference is driven by more SCCs than Protostellar clumps below $470 M_\odot$ and more Protostellar clumps than SCCs above that mass. We statistically estimate the highest mass SCC by integrating the upper-tail of $M_{\text{H}_2}^{\text{Total}}$ PDF to where it equals one part in the sample size, $1 : 625$, or the 99.84th percentile. This sets the maximum observed mass of SCCs at $< 1.4 \times 10^4 M_\odot$. The observed increase in mass towards clumps associated to more extreme star formation indicators could be due to several physical and systematic explanations. In the remainder of this section, we explore possible systematic effects to generate the observed mass difference.

For physical properties that depend on the dust temperature of the clumps, we assume an isothermal temperature with $T_{\text{dust}} = T_K$ in the clumps. Nominally, these two temperatures

are only expected to be well coupled by collisions at densities greater than $\sim 10^5 \text{ cm}^{-3}$ (Goldsmith 2001; Young et al. 2004). Battersby et al. (2014) find no correlation between NH_3 -derived T_K and *Herschel*-derived T_{dust} for a quiescent clump; however, agreement within 20% is observed when the *Herschel* data is not background subtracted. Battersby et al. (2014) suggest that the gas and dust are weakly coupled at densities $10^4 - 10^5 \text{ cm}^{-3}$. Similarly, the T_{dust} derived from far-infrared SEDs in Traficante et al. (2015a) show a 20% agreement to T_K for both starless candidate and protostellar clumps. A 20% decrease in T_{dust} (from $T_K \sim 12$) will increase our mass and column density measurements for the starless candidate group by 30%. This effect alone is not enough to explain the observed mass differences. There is no reason to decrease only the dust temperatures of starless clump candidates. Any simultaneous decrease in T_{dust} for protostellar clumps would mitigate the decrease of the median mass differences.

In reality, there are dust temperature gradients within the BGPS beam due to heating from the interstellar radiation field and due to embedded protostars in protostar-containing clumps. The general effect of line-of-sight dust temperature gradients on greybody SED fitting of dust continuum emission is to overestimate the dust temperature and underestimate the mass more severely for starless clumps than protostellar clumps (Malinen et al. 2011). The corresponding effect on the line-of-sight average NH_3 T_K cannot explain the observed mass difference unless the temperature gradients cause an underestimate of the average line-of-sight T_K for the starless clump candidates from the observed median value of 12 K down to 8.8 K, a value that is lower than all NH_3 -based T_K measurements in this paper and 95% of SED-based T_{dust} measurements in Traficante et al. (2015a). Analysis of the dust temperature profiles from grids of radiative transfer models of low-mass starless cores (Shirley et al. 2005; Launhardt et al. 2013) find that the mass-weighted average T_{dust} never drops below 10 K for a grid of Bonner-Ebert spheres (Ebert 1955; Bonnor 1956) with central densities spanning 10^4 to $3 \times 10^6 \text{ cm}^{-3}$ and strength of the interstellar radiation field equal to half the standard value (Habing 1968). These low-mass starless core models are not the exact analogues of massive starless clumps which are possibly fragmented and clumpy, have lower observed average density (Figure 14), and are likely subject to stronger heating from the interstellar radiation field than half the Habing value, effects which will increase the average T_{dust} compared to low-mass starless cores. These results indicate it is unlikely that dust temperature gradients result in an average T_{dust} as low as 8.8 K. Radiative transfer modeling of the entire BGPS clump population is beyond the scope of the current paper and requires higher spatial resolution continuum and NH_3 images. In the absence of reliable dust continuum temperatures for the full sample, a single component $T_{\text{dust}} = T_K$ assumption is the next best alternative.

The other assumption made in calculation of mass surface density and mass is that the dust opacities are well described by OH5 dust. They are a popular set of opacities because grains are expected to coagulate and accrete ice mantle in dense environments and there are observational constraints that indicate OH5 opacities are a reasonable match, albeit toward nearby, low-mass cores (see Shirley et al. 2011). The OH5 model assumes that the grains have coagulated for a period of 10^6 years at a density of 10^5 cm^{-3} . Both this time period and the density used in the coagulation model are likely larger than the typical values observed toward BGPS clumps (see Schlingman et al. 2011; Dunham et al. 2011a). In order to explain the ob-

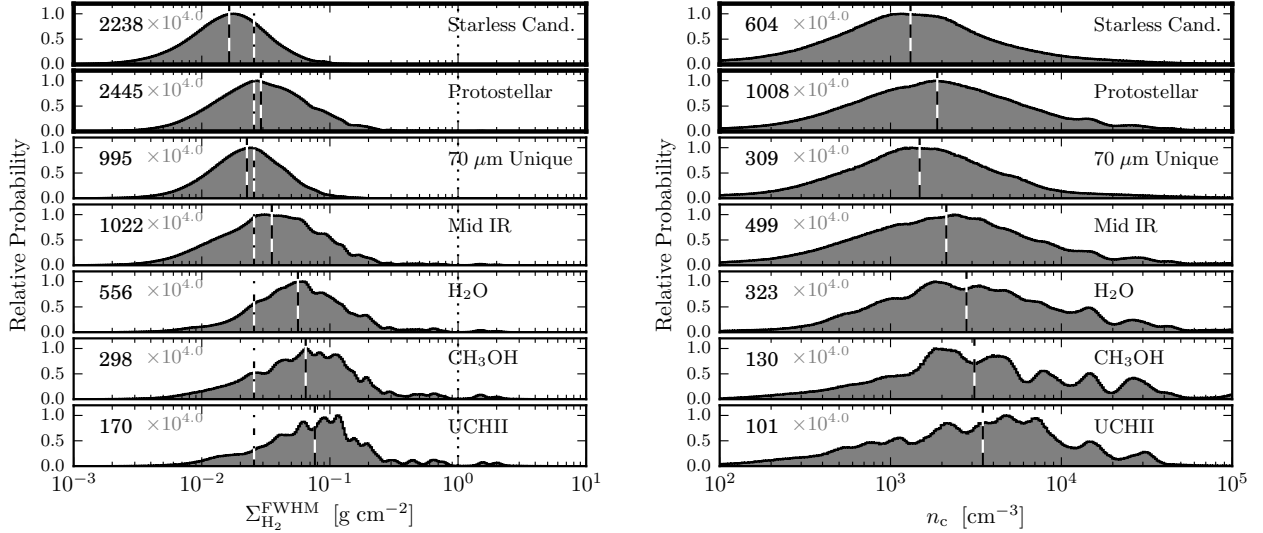


Figure 14. Distributions of FWHM mass surface (Left) density and central density (Right) from MC simulations by star formation indicator. The dashed lines show the median value and the number of clumps in the subsample is shown in the upper left. The dotted line shows the predicted 1 g cm^{-3} threshold for the formation of a massive star from [Krumholz & McKee \(2008\)](#). The dash-dotted line shows the 0.025 g cm^{-3} threshold for star formation observed in local clouds ([Lada et al. 2010](#); [Heiderman et al. 2010](#)).

served $\Delta M_{\text{H}_2}^{\text{Total}}$ the opacity ratio towards protostellar clumps versus starless clumps would have to be $1.7 - 2.6$ (for $70 \mu\text{m}$ unique clumps or the full protostellar clump sample). While it is certainly likely that there are opacity variations among clumps that deviate from the assumed OH5 opacities, the variation would have to be systematic between starless candidate and protostellar clumps. There is currently no evidence for or against such a systematic variation in opacities.

The observed mass difference cannot be due to selection effects on the flux density $S_{1.1}$ of the Distance Sample alone (i.e., the subsample of clumps that have DPDFs compared to those without) because SCCs and protostellar clumps have similar ratios in median $S_{1.1}$ (see §5, Fig. 8d). At most this effect could account for $\sim 10\%$, lowering the mass difference to $\Delta \mu_{1/2}(M_{\text{H}_2}) \approx 330 M_{\odot}$. In addition, as a flux limited survey, the BGPS is effected by Malmquist bias and mass incompleteness. [Ellsworth-Bowers et al. \(2015\)](#) derive the mass completeness function for clumps in the Distance Sample by computing Monte Carlo simulations drawn from the DPDFs, where the sample is 50% complete above $M_{\text{H}_2}^{\text{Total}} \approx 70 M_{\odot}$ and 90% above $M_{\text{H}_2}^{\text{Total}} \approx 400 M_{\odot}$. The median SCC mass, $M_{\text{H}_2}^{\text{Total}} = 230 M_{\odot}$, is at the 80% completeness level, and the 90% completeness level is achieved at the 64th mass percentile. The incompleteness in the SCC category should not, qualitatively, affect the observed median mass difference. Because R_{proto} is smaller at low flux densities and masses, the population of undetected clumps with $M < 400$ would disproportionately add to the SCC category and simply enhance the median mass difference further.

One additional possibility is the spatial filtering in the BGPS survey has systematically affected the flux densities of sources. [Ginsburg et al. \(2013\)](#) estimate the effects of spatial filtering by approximating the source brightness distribution as a power-law with varying index and finds that the flux density for sources with angular radii less than $40''$ is essentially recovered (see [Ginsburg et al. \(2013\)](#) Figure 8). Depending on the exact value of the power-law index, the spatial filtering recovers $> 75 - 80\%$ of the flux density for sources with angular radii $< 60''$. This accounts for 77% (3606/4683) of the BGPS

sources. It is evident from Fig. 10a that the sources more strongly affected by spatial filtering are protostellar stages with more luminous evolutionary indicators which tend to have larger angular radii. Thus, accounting for spatial filtering should systematically increase the median mass difference between starless clump candidates and protostellar clumps. A detailed analysis of the effects of spatial filtering on a source by source basis is beyond the scope of the present work.

In summary, the observed mass difference cannot be explained by biases between the Distance sample and the full sample, incompleteness, spatial filtering, or our assumptions in the mass calculation unless there is a factor $1.7 - 2.6$ systematic variation in dust opacities between starless clump candidates and protostellar clumps. Interestingly, the BGPS sample is the second statistically significant sample to see this systematic offset in mass. The *Herschel* survey of ([Traficante et al. 2015a](#)) toward IRDCs also find a modest offset of $\sim 80 M_{\odot}$ between the average mass of starless clumps and protostellar clumps. While the mass difference is smaller by a factor of two in their study than ours, the mass difference in their survey is significant. Alternatively, [Hoq et al. \(2013\)](#) using data from the first year data release of the MALT90 molecular line mapping survey of several hundred ATLASGAL clumps in the fourth and first quadrants do not observe an increasing trend in total mass from an “ $8/24 \mu\text{m}$ quiescent” phase to a “PDR” phase. It should be noted that these two surveys are drawn from subsets of clumps in the Galactic plane; therefore interpretation of these results depend on how the properties of the subsets compare to the more complete clump populations observed in (sub)millimeter continuum Galactic plane surveys. In §6.3 we explore possible physical explanations for the variation in the median mass between the starless clump candidates and protostellar candidates under the assumption that the observed mass difference is real.

5.4.3. Virial Parameter

The virial parameter, $\alpha = M_{\text{vir}}/M$, expresses the relative importance of gravitational and kinetic energy, and can be used to assess whether clumps are gravitationally bound and/or

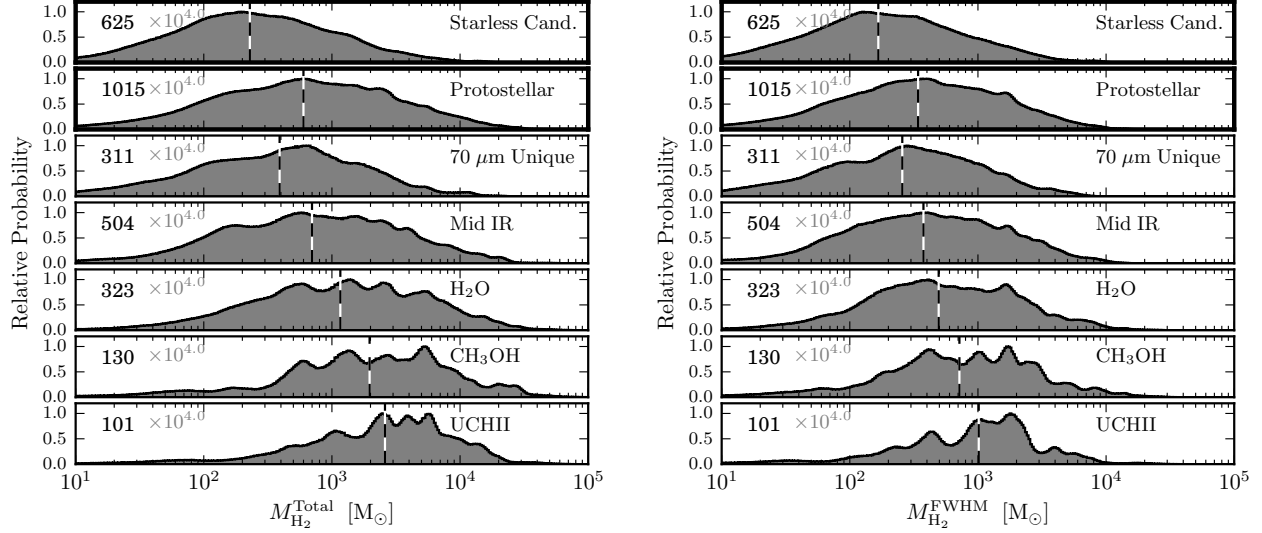


Figure 15. Distributions drawn from MC simulations of total mass (Left) and FWHM mass (Right) sorted by star formation indicator. The number of clumps in a sample is shown in the upper left and a vertical dashed line shows the median value.

stable to collapse. We calculate the virial parameter for a homoeoidal ellipsoid (ellipsoid of revolution) via

$$\alpha = \frac{5}{8 \ln 2} \frac{1}{a_1 a_2} \frac{\Delta v^2 R}{GM} \quad (7)$$

$$\approx 1 \frac{1}{a_1} \left(\frac{\Delta v}{1 \text{ km s}^{-1}} \right)^2 \left(\frac{R}{1 \text{ pc}} \right) \left(\frac{M}{209 M_\odot} \right)^{-1}$$

where $a_1 = \frac{1-p/3}{1-2p/5}$ is the correction factor for a power-law density distribution with index p and $a_2 \sim 1$ for sources with aspect ratios less than 2 (Bertoldi & McKee 1992). For a clump with negligible magnetic fields, $\alpha = 1$ is gravitational virial equilibrium and $\alpha \approx 2$ is marginally gravitationally bound (see Kauffmann et al. 2013). The BGPS does not have sufficient resolution to constrain p , so lacking appropriate data, we draw $p = 1.8 \pm 0.4$ Gaussian-deviates in the MC simulations, as constrained from dust continuum modelling of high-mass star forming regions (Mueller et al. 2002). Here we use the total mass and radius, thus setting the outer boundary to calculate α at the extent of the 1.1 mm emission. Figure 16 shows the virial parameter calculated from MC simulations for starless candidates and protostellar clumps with median values $\alpha = 0.73 \pm 0.06$ and $\alpha = 0.68 \pm 0.03$ respectively, suggesting that most clumps are in approximate virial equilibrium with more than half of clumps in the Distance Sample with NH_3 observations showing (sub)-virialized motions ($\alpha \lesssim 1$). Further, 76% of the starless candidates and 86% of the protostellar clumps have $\alpha < 2$ implying that most BGPS clumps are gravitationally bound. Although 24% of the starless candidates are unbound by the criteria $\alpha > 2$, it is probable that these clumps host gravitationally bound higher density substructures. These results suggest that the majority of BGPS clumps in the Distance Sample are self-gravitating or collapsing.

Observations of GMCs indicate virial parameters that are typically $\gtrsim 2$ (Larson 1981; Solomon et al. 1987; Scoville et al. 1987). For instance, analysis of GMCs in the Galactic Ring Survey find a mean value of $\alpha = 1.9$ (Heyer et al. 2009). For smaller clump scales there exist a range of virial parameter measurements that report samples with $\alpha \gtrsim 1$ or $\alpha \lesssim 1$ (see Kauffmann et al. 2013 for a summary of literature values).

We find our measurements of $\alpha \lesssim 1$ consistent with other Galactic plane surveys towards clumps from both BGPS and ATLASGAL with NH_3 -determined linewidths. The most direct comparison are previous studies using GBT observations of NH_3 that have been carried out towards the BGPS sources (Dunham et al. 2010, 2011b). Dunham et al. (2011b) measured the virial parameter towards 456 BGPS clumps with a median $\alpha = 0.74$. Wielen et al. (2012) also measure the virial parameter toward ATLASGAL clumps using NH_3 , and find a mean $\alpha \lesssim 1$ for clumps.

One important aspect that is often ignored in the standard virial parameter analysis is the importance of magnetic fields in virial balance. Magnetic fields in dense gas are notoriously difficult to measure, and there have been no systematic observations toward BGPS clumps. We can estimate the B-field strength required for virial balance from the expressions derived in Kauffmann et al. (2013) (their Equations 6 and 16)

$$B \gtrsim 15 \mu\text{G} \left(\frac{2}{\alpha} - 1 \right) \left(\frac{\Delta v}{1 \text{ km s}^{-1}} \right)^2 \left(\frac{1 \text{ pc}}{R} \right) . \quad (8)$$

Evaluating the above expression for the median values of the starless clump candidates indicate that the B-fields of only 50 μG are needed to support typical starless clump candidates against collapse. Magnetic fields of this magnitude and larger are indeed observed toward IRDCs. For instance, Pillai et al. (2015) find a total B-field strength of $\sim 250 \mu\text{G}$ toward the IRDC G11.1 from analysis of submillimeter continuum polarization. The required B-field strength scales as $B \sim 1/\alpha$, implying that very sub-virial clumps with $\alpha \lesssim 0.1$ required $B \gtrsim 600 \mu\text{G}$. In these more extreme cases, B-field support may prove difficult, but for the typical (median property) starless clump candidates, the required B-field strength for support is within a reasonable range of observed values (for a summary of B-field measurements, see Crutcher 2012).

6. DISCUSSION

For many of the observed properties and calculated physical properties analyzed in §5, there is a systematic trend in the property with the ordering of the star formation indicators from 70 μm unique flags, mid-IR star formation flags,

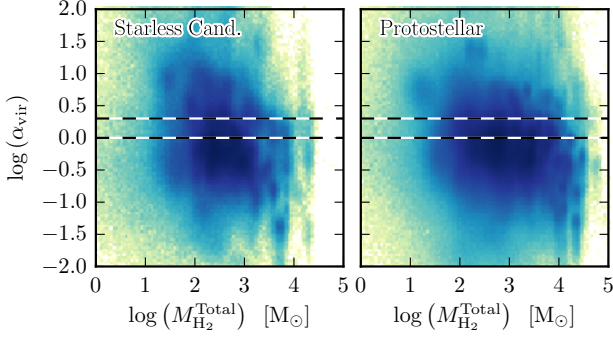


Figure 16. Comparison of virial parameter to clump total mass for SCCs (left) and protostellar clumps (right) computed using values drawn from the MC simulations. Virial parameters are derived from the model-fit NH_3 velocity dispersion. The dotted lines show $\alpha = 1$ and $\alpha = 2$. Note the logarithmic scaling.

H_2O maser flags, CH_3OH flags, to UCHII flags. Protostellar clumps that contain the most extreme indicators of luminous protostars (CH_3OH maser and UCHII containing clumps) tend to have the highest flux densities, are the most centrally condensed, have the highest temperatures, are more turbulent and more massive on median than other clumps. A partial evolutionary analysis of the ATLASGAL clumps associated to RMS sources, CH_3OH maser, and UCHII regions, has been performed (Urquhart et al. 2011, 2013a,b, 2014). The BGPS results are consistent with the observed trends (M , T_K) for the properties of ATLASGAL clumps that contain methanol masers and HII regions (see Table 4 of Urquhart et al. 2014). In contrast, the observable and physical properties indicate that starless clump candidates have lower flux densities, are less centrally concentrated, have smaller sizes, are colder and less turbulent, and are less massive on median when compared to clumps with indications of protostellar activity. In this section, we explore the potential for forming massive stars, the timescales for evolution of this newly discovered population of starless clumps, and explore possible explanations for the observed median mass difference between starless and protostellar clumps.

6.1. Massive Star-forming Potential of Clumps

With a robust sample of starless clump candidates, it is important to assess their potential to form high-mass stars. We can estimate the mass of the most massive star formed by a starless clump candidate, M_{max} , using the stellar Initial Mass Function (IMF) from Kroupa (2001)¹³. The total stellar cluster mass is equal to the mass of the progenitor clump times a star formation efficiency factor ϵ_{SF} . We can derive a relationship between M_{max} and the mass of the clump from

$$\epsilon_{\text{SF}} M_{\text{clump}} = \frac{\int_{0.08}^{150} N(M) M dM}{\int_{M_{\text{max}}}^{150} N(M) dM} \quad (9)$$

$$M_{\text{max}} \approx 20 M_{\odot} \left(\frac{\epsilon_{\text{SF}} M_{\text{clump}}}{0.3 \cdot 1064 M_{\odot}} \right)^{1/1.3}, \quad (10)$$

where the IMF is normalized such that at least 1 star with $M \geq M_{\text{max}}$ is formed. The values of ϵ_{SF} range from 0.05 – 0.5 with a typical value of 0.3 (see Lada & Lada 2003; Shirley et al.

¹³ $N(M) \propto M^{-1.3}$ for $0.08 M_{\odot} \leq M \leq 0.5 M_{\odot}$, $N(M) \propto M^{-2.3}$ for $M > 0.5 M_{\odot}$. We assume a maximum stellar mass of $150 M_{\odot}$ in IMF calculations.

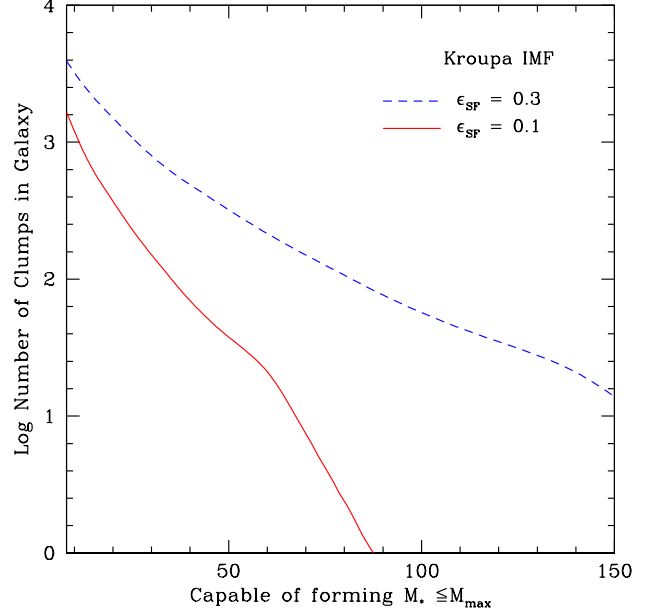


Figure 17. The number of clumps in the Milky Way capable of forming a star with a mass $\leq M_{\text{max}}$ assuming a Kroupa IMF. Two star formation efficiencies are plotted for the clumps (0.1 in red solid line and 0.3 in blue dashed line).

2003; Krumholz et al. 2007; Kuiper et al. 2010; Bontemps et al. 2010). Using $8 M_{\odot}$ as the definition of the minimum mass of a high-mass star, the corresponding BGPS clump mass is $320 M_{\odot}$. In the Distance Sample 42% of SCCs (264 clumps) have masses above $320 M_{\odot}$ in the MC simulations. This corresponds to 603 SCCs in the BGPS survey volume if we assume the SCCs without well-constrained DPDFs have a similar average DPDF and account for the different flux density distributions. If we use the Wolfire et al. (2003) model of the H_2 distribution in the Galaxy as an axisymmetric proxy for the massive clump spatial distribution¹⁴, then there are ~ 3900 SCCs capable of forming a $8 M_{\odot}$ star in the entire Milky Way. Figure 17 plots the number of clumps in the Milky Way capable of forming stars with masses $\leq M_{\text{max}}$. Note that the number of clumps is very sensitive to assumed star formation efficiency, especially for very massive stars.

An alternative way to assess the massive star-forming potential of BGPS clumps is to compare M_{H_2} and R_{eq} (Figure 18). Values are represented as the median value drawn from the MC simulations per clump. A robust increasing correlation is observed with $\rho_{\text{sp}} = 0.942$. To show the differences in clumps by star formation activity we plot SCCs in yellow and clumps associated to UCHII or CH_3OH masers as unambiguous detections of high-mass star formation activity in red. The distributions of points follow the general trends in discussed in §5: SCCs are generally lower mass, smaller radius, and lower mass surface density. Several thresholds for star formation

¹⁴ The correction factor is calculated numerically by integrating the H_2 density distribution over the volume of the wedge observed by the BGPS divided by the integral of the H_2 density distribution over the total volume of the Galaxy. The Wolfire et al. (2003) density distribution is given by $\rho(R_g, z_g) \propto \exp(-4 \ln 2 (R_g - 0.571 R_{\odot})^2 / (0.52 R_{\odot})^2) \exp(-|z_g|/0.059)$ for $R < 0.82 R_{\odot}$ and $\rho(R_g, z_g) \propto \exp(-R_g / (0.34 R_{\odot})) \exp(-|z_g|/0.059)$ for $R \geq 0.82 R_{\odot}$ where R_g is the Galactocentric radius in kpc, z_g is the height above the Galactic mid-plane in kpc, and $R_{\odot} = 8.5$ kpc is the distance to the Galactic center. Note that we account for the vertical offset of 25 pc of the Sun above the Galactic plane in the calculation of the BGPS wedge integrals (see Appendix C of Ellsworth-Bowers et al. 2013).

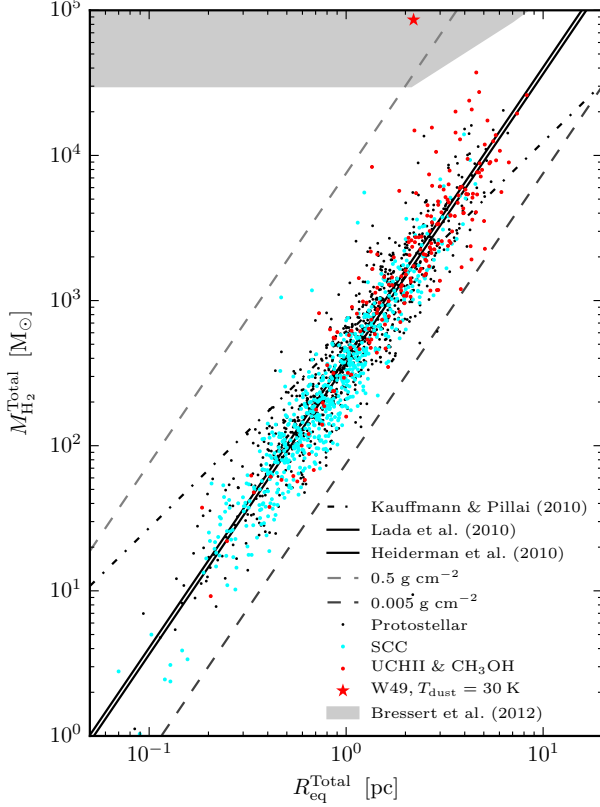


Figure 18. Equivalent radius compared to total mass. Median values for each clump are computed from MC simulations. Clumps are shown associated to UCHII or CH₃OH masers (red), other protostellar (black), and SCCs (cyan). The dash-dotted line shows the threshold for high-mass star formation $M(R) \geq 580 M_{\odot} (R \text{ pc}^{-1})^{1.33}$ from Kauffmann & Pillai (2010) when scaled to OH5 dust opacities. Solid lines show thresholds for “efficient star formation” of $116 M_{\odot} \text{ pc}^{-2}$ (Lada et al. 2010) and $129 M_{\odot} \text{ pc}^{-2}$ (Heiderman et al. 2010). The upper and lower dashed gray lines show 0.5 g cm^{-2} and 0.005 g cm^{-2} respectively. The shaded gray region in the upper left indicates the part of parameter space for Young Massive Clusters as defined in Bressert et al. (2012).

determined from local clouds are over-plotted. Fitting star formation rates to local molecular clouds, Lada et al. (2010) and Heiderman et al. (2010) find relationships for “efficient” star formation of $\approx 116 M_{\odot} \text{ pc}^{-2}$ and $129 \pm M_{\odot} \text{ pc}^{-2}$, respectively, where above these thresholds the star formation rate is linearly proportional to mass surface density. The thresholds from Lada et al. (2010) and Heiderman et al. (2010) approximately bisect the samples, with 50.6% and 42.5% of the full samples, 46.6% and 39.9% of the UCHII and CH₃OH maser sample, and 41.4% and 33.6% of the SCC sample each exceeding the respective limits. Kauffmann & Pillai (2010) derive the more restrictive criteria of $M \leq 580 M_{\odot} (R_{\text{eq}}/\text{pc})^{1.33}$ from observations of nearby molecular clouds. Note that Kauffmann & Pillai (2010) scale their OH5 dust opacities down by a factor of 1.5, so for consistency to values in this work we use the leading factor of $580 M_{\odot}$ rather than the original $870 M_{\odot}$. In the BGPS Distance Sample, 24.8% of the full sample, 54.9% of the UCHII and CH₃OH maser sample, and 10.8% of the SCC sample each exceed this criteria. Because nearly half of BGPS clumps with an unambiguous detection of a high-mass YSO do not meet this criteria, this suggests that the BGPS cloud structures do not strictly follow the criteria derived in Kauffmann & Pillai (2010). While the majority of SCCs lie

below this threshold, any systematic growth would increase clump total mass and radius, placing them in phase-space for a higher probability of high-mass star formation (see §6.3.2). In a similar blind sample from the ATLASGAL survey, Wiene et al. (2015) find that 92% of ATLASGAL clumps meet this criteria and 100% above the Lada et al. (2010) and Heiderman et al. (2010) lines. Notably, only 1 clump in the BGPS from $10^{\circ} < \ell < 65^{\circ}$ (W49, G043.167+00.011) meets the criteria for the progenitors of Young Massive Clusters (YMCs; Longmore et al. 2014) with clump masses $\gtrsim 10^5 M_{\odot}$, although W49 is not a SCC because it is actively forming stars.

6.2. Clump Timescales

6.2.1. Average Free-fall Time

For the SCC sample we estimate the average free-fall time, t_{ff} , calculated with

$$t_{\text{ff}} = \sqrt{\frac{3\pi}{32G\mu m_{\text{p}} n_{\text{c}}}} \quad (11)$$

$$\approx 0.98 \left(\frac{n_{\text{c}}}{10^3 \text{ cm}^{-3}} \right)^{-1/2} \text{ Myr.}$$

where n_{c} is the clump central density. We estimate the clump central density n_{c} from the peak mass surface density and FWHM radius, assuming a spherically symmetric Gaussian density distribution (cf. Appendix C of Pattle et al. 2015). Integrating over the FWHM cylindrical aperture yields the expression

$$n_{\text{c}} = \sqrt{\frac{\ln 2}{\pi}} \frac{\Sigma_{\text{H}_2}^{\text{peak}}}{\mu m_{\text{H}} R^{\text{FWHM}}} \left[\text{erf} \left(\sqrt{\ln 2} \frac{\theta^{\text{Total}}}{\theta^{\text{FWHM}}} \right) \right]^{-1} \quad (12)$$

where θ is the deconvolved angular radius for the Total or FWHM definition (see §5.2) and μ is the mean molecular weight. While a density distribution described by a singly peaked Gaussian is a crude assumption, it is more representative of higher density sub-structures within starless clumps than just the average density with the FWHM. Figure 19 shows the average free fall time plotted versus the mass of the clumps of the MC simulation. There is no significant correlation between the average free-fall time with the mass of the clumps. The median is $t_{\text{ff,c}} = 0.84 \pm 0.02 \text{ Myr}$ for the starless clump candidates.

Since the BGPS clump FWHM sizes are typically a factor of two larger when compared to the Jeans length of $0.36 \text{ pc} (T_{\text{K}}/15 \text{ K})^{1/2} (10^3 \text{ cm}^{-3}/n_{\text{c}})^{1/2}$, these starless clumps should fragment into smaller structures. Higher resolution observations of a subset of BGPS clumps show this fragmentation into objects with higher densities (Merello et al. 2015). As a result, the median t_{ff} is likely an upper limit to the free-fall time for a typical starless clump candidate to form a single detectable star.

6.2.2. Clump Lifetimes from Number Statistics

If the Galactic population of clumps is in steady state where the clump formation rate is equal to the destruction rate then the number fraction of clumps in a given state is proportional to the lifetime of that state. We find nearly equal numbers of starless clump candidates (47.5%) compared to protostellar clumps. This result implies that the typical lifetime of a starless clump candidate is nearly equal to the typical lifetime of a protostellar clump. The starless clump lifetime is defined as the time it takes for a clump detectable by the BGPS to form a

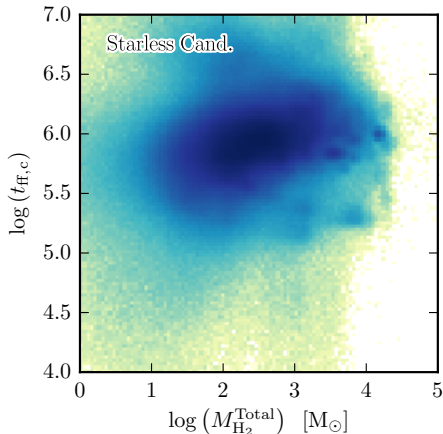


Figure 19. Comparison of clump free-fall time to clump total mass for starless clump candidates computed using values drawn from the MC simulations. Free-fall time values calculated from central density n_c .

single star that is detectable in current infrared surveys of the Galactic plane. The protostellar clump lifetime is determined by the time it takes a cluster of stars to form (not a single star) and dissipate the gas and dust to the point where the clump is no longer detectable in the BGPS. This latter timescale is difficult to determine, but we can use the cluster formation timescale as a rough estimate. This cluster formation timescale has a large range and is typically longer than 1 Myr and up to a few Myrs (Rebull et al. 2007, Chomiuk & Povich 2011, Morales et al. 2013; see review by Longmore et al. 2014). The total population statistics imply a long average timescale for starless clump candidates that is on the order of a few times the average free-fall time of the clumps and that is consistent with the effects of turbulence and or magnetic fields lengthening the starless evolution timescale.

A single timescale cannot properly describe the starless clump evolution timescale because clumps with different masses should evolve out of the starless phase at different rates. While a median mass starless clump candidate ($230 M_\odot$) may have a lifetime over 1 Myr, it seems highly unlikely that $10^4 M_\odot$ starless clumps exist in a starless phase for that long. The lack of very massive ($M > 1.4 \times 10^4 M_\odot$) starless clump candidates argues for a shorter timescale for these objects to form a single detectable star and move to the Protostellar clump category. Current single timescale estimates (or upper limits) in the literature for massive starless clumps (Csengeri et al. 2014; Traficante et al. 2015a) are problematic because they do not account for this variation with mass and because they also attempt to compare to a single timescale for the lifetime of the embedded massive star formation phase (i.e., Davies et al. 2011; Duarte-Cabral et al. 2013). For the remaining discussion, we analyze how starless clump lifetimes vary with the mass of the clumps.

We can estimate how the clump lifetime for massive clumps vary with mass by using a method pioneered in Battersby (2013, Ph.D. Thesis) by pinning the relative lifetimes of clumps to an estimated absolute lifetime of the Class II CH₃OH maser $\tau_{\text{CH}_3\text{OH}} = 2.5 - 4.5 \times 10^4 \text{ yr}$ (van der Walt 2005). This timescale is a statistical estimate based on correcting the number of the observed CH₃OH masers in Pestalozzi et al. (2005) for completeness to predict the total Galactic count of high-mass stars with mass $> 20 M_\odot$. van der Walt (2005) uses a $\text{SFR} = 4 M_\odot \text{ yr}^{-1}$ based on the $\text{SFR} = 3 - 6 M_\odot \text{ yr}^{-1}$ range

in Boissier & Prantzos (1999). Chomiuk & Povich (2011) re-analyze several Galactic SFR measurements (see Table 1 therein) to derive $\text{SFR} = 1.9 \pm 0.4 M_\odot \text{ yr}^{-1}$. The Chomiuk & Povich (2011) study is unique in that they apply the same IMF (Kroupa 2001) and SFR law to all measurements and use the Starburst99 code to self-consistently compare studies with substantially different methodologies (including free-free radio continuum observations as well as YSO counts). Scaling the CH₃OH maser lifetime inversely by their revised SFR yields $\tau_{\text{CH}_3\text{OH}} = 6.1 - 9.3 \times 10^4 \text{ yr}$.

The clump lifetime is calculated using the relative number fraction of sources compared to the CH₃OH maser sample at a given mass via

$$\tau_{\text{SCC}} = \tau_{\text{CH}_3\text{OH}} \left(\frac{N_{\text{SCC}}}{N_{\text{CH}_3\text{OH}}} \right) \quad (13)$$

where $\tau_{\text{CH}_3\text{OH}}$ is the completeness corrected and the SFR corrected Class II CH₃OH maser lifetime. The ratio of $N_{\text{SCC}}/N_{\text{CH}_3\text{OH}}$ is corrected for the fraction of SCCs and clumps with CH₃OH that are in the Distance sample compared to the total sample. The fundamental assumption of this method is that all clumps capable of forming a $20 M_\odot$ star ($M_{\text{clump}} > 1000 M_\odot$) will at some time form high-mass YSOs with detectable CH₃OH masers. A population of equal mass clumps that are not capable of producing observable CH₃OH masers would decrease the observed fraction and lead us to overestimate the inferred lifetime. This method also assumes the lifetime of a single CH₃OH maser ($\tau_{\text{CH}_3\text{OH}}$) for all clumps with CH₃OH maser associations. For clumps associated to multiple CH₃OH maser sites (i.e., YSOs) an age spread within the clump would increase the observed duration of the clump CH₃OH maser phase and lead us to underestimate the phase lifetime when the shorter, single YSO $\tau_{\text{CH}_3\text{OH}}$ is applied; however, for clumps associated to MMB sources, which have accurate interferometric positions, only 25/272 (9.2%) are host to more than one CH₃OH maser, so this does not likely introduce a strong bias. To calculate the lifetimes as a function of mass we extend this method to the relative fractions of MC samples in narrow mass bins (0.0125 dex logarithmic bins for 10^4 MC mass samples per clump). In effect this is the ratio of two mass PDFs each scaled by the sample sizes and then multiplied by $\tau_{\text{CH}_3\text{OH}}$.

Figure 20 shows the lifetime of SCCs as a function of mass. The starless candidate clump lifetime approximately follows $\tau_{\text{SCC}} \sim 0.37 \pm 0.08 \text{ Myr} (10^3 M_\odot / M)$ for $M > 10^3 M_\odot$. The uncertainty corresponds the systematic uncertainty in $\tau_{\text{CH}_3\text{OH}}$. It is not advisable to continue our timescale analysis to $< 1000 M_\odot$ as the assumption that all clumps will form a CH₃OH maser is less likely to be true; however, extrapolation of the trend to lower masses indicates that the starless clump lifetime becomes longer than the average clump free-fall time at $< 450 M_\odot$. This is approximately twice the median SCC mass. Thus, most starless clump candidates have lifetimes longer than their average free-fall times of 0.8 Myr. In turn, very massive starless clump candidates with $M_{\text{H}_2} > 10^4 M_\odot$ have very short lifetimes $\tau \lesssim 0.03 \text{ Myr}$ consistent with lack of such massive objects detected in the BGPS survey (Ginsburg et al. 2012). Our lifetimes estimates are 5 times longer and 3.5 times longer than the lifetimes estimates of Tackenberg et al. (2012) for ATLASGAL clumps capable of forming $20 M_\odot$ and $40 M_\odot$ stars respectively. The Tackenberg et al. (2012) estimates are based on large extrapolations from small numbers of clumps (6 and 1 respectively) observed in their 20 square

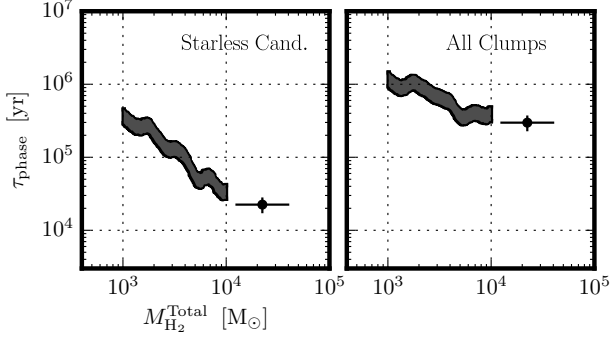


Figure 20. Clump lifetimes as a function of total mass. Relative lifetimes are computed from the number of MC samples in a narrow mass range and scaled using an absolute lifetime for the Class II CH₃OH maser, between $6.1 - 9.3 \times 10^4$ yr, corresponding to the upper and lower limits of the filled curves. The markers show the average values for $M > 10^4 M_{\odot}$ where $N \lesssim 30$.

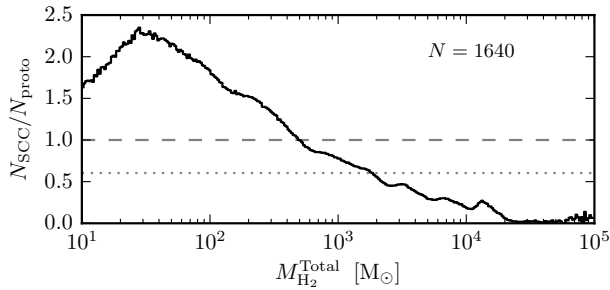


Figure 21. Ratio of starless clump candidates to protostellar clumps by total clump mass drawn from the MC simulations. The dotted line shows the total sample fraction $613/1027 \approx 0.597$. The plotted values taken from the Distance Sample are corrected by the factor $1027/613 \approx 1.675$ to be representative of the full survey.

degree survey area to the entire Galaxy.

6.3. Origin of Starless vs. Protostellar Clump Mass Difference

In §5.4.2 a systematic difference between the median mass of protostellar clumps and starless clump candidates of $170 - 370 M_{\odot}$ was discussed. Fundamentally, the median mass difference is due to more starless clump candidates with masses below $M \lesssim 470 M_{\odot}$ and fewer higher mass starless clump candidates than protostellar clumps (see Figure 21). We explore three possible physical explanations for this mass difference: (i) not all starless clump candidates will evolve into detectable protostellar clumps, (ii) clumps grow in mass by accreting surrounding material from their parent GMC, and (iii) clumps evolve at different rates from the starless to protostellar phase in exact proportion to their number statistics.

6.3.1. Infertile Starless Clumps

Perhaps the simplest physical explanation for the systematic mass difference is that there is a large population of clumps among the SCCs that, while starless, will not evolve to form YSOs detectable by our star formation indicators. In order for this population of objects to remain starless clump candidates, they would either remain “infertile” and never form stars or would only be able to form stars with bolometric luminosities that are less than the $30 - 140 L_{\odot}$ sensitivity (corresponding to $1 - 2 M_{\odot}$ protostars accreting at typical rates) of current far-infrared Galactic plane surveys (§3). Such a population of

low-density and low-mass clumps would bias the SCC distribution to lower masses. For a Kroupa IMF, a $230 M_{\odot}$ median mass SCC is capable of forming stars up to $6 M_{\odot}$, which is detectable given the sensitivity limits of current far-infrared surveys (see Figure 4); however, for SCCs at the 50% BGPS mass completeness limit of $70 M_{\odot}$, the maximum mass star formed is only $2.5 M_{\odot}$ which is closer to the sensitivity limit of current mid- and far-infrared surveys.

One test of this hypothesis is to check for the presence of dense gas. The HCO⁺ $3 - 2$ transition has an effective excitation density $n_{\text{eff}} > 10^4 \text{ cm}^{-3}$ for the typical properties of starless clump candidates (Shirley 2015). HCO⁺ $3 - 2$ from Shirley et al. (2013) was detected towards 44% of SCCs and 78% of protostellar clumps in the Distance Sample. This result indicates that there is either a population of lower density SCCs or that their filling fraction of dense gas is less than toward protostellar clumps. Since the $3 - 2$ transition has an upper energy level that is 25.7 K above ground, the effective excitation density (n_{eff}) is a very sensitive function of T_{K} at the median temperature of 12.8 K measured toward SCCs. The sensitivity of the $3 - 2$ transition to T_{K} means that the detection is biased against the SCCs that are colder on average than protostellar clumps. So this test is biased meaning that since SCCs are colder on average than protostellar clumps, HCO⁺ $3 - 2$ requires higher densities in SCCs (by a factor of ≈ 2) to be excited than toward protostellar clumps.

Another test of this hypothesis is to carefully control systematic effects from sampling clumps with different physical properties by performing a variety of astrophysical cuts on the sample and calculate the distribution of $\Delta\mu_{1/2}(M_{\text{H}_2})$ from the MC simulations. These cuts are designed to remove low-mass, low-density, or unbound objects. Figure 22 shows the cumulative distribution functions (CDFs) for $\Delta\mu_{1/2}(M_{\text{H}_2})$ subsamples selected on mass, NH₃-derived gas kinetic temperature, heliocentric distance, virial parameter, mass surface density, central density, and molecular detections. The observed mass differences between categories, $\Delta\mu_{1/2}(M_{\text{H}_2})$ are robust to these criteria, with the values calculated with respect to the Hi-GAL $70 \mu\text{m}$ Unique category at $\Delta\mu_{1/2}(M_{\text{H}_2}) \sim 100 - 200 M_{\odot}$ and the values calculated with respect to the Protostellar category ranging between $\Delta\mu_{1/2}(M_{\text{H}_2}) \sim 200 - 500 M_{\odot}$. The robustness of the median mass difference to astrophysical cuts does not support the explanation that a population of low star formation potential SCCs solely drive the increasing trend in clump total mass.

6.3.2. Possible Clump Mass Growth

BGPS clumps commonly reside in a complex structural hierarchy of clouds and filaments. When sorted by protostellar indicator, the increasing trend in both Σ and M_{tot} but weak increasing trend in R_{eq} are consistent with the physical process of clumps, as focusing points of local gravitational potential minima, accreting mass from the surrounding cloud in a “conveyor belt” fashion while maintaining the same approximate volume. Clump mass growth via accretion from the surrounding molecular cloud is a possible mechanism for the difference between SCCs and protostellar clump masses. An upper-limit to the clump accretion rate can be set by the free-fall time of the highest density sub-component of the clump. An estimate of t_{ff} from the MC simulation shown in Figure 19, suggest a median $t_{\text{ff}} = 0.84 \text{ Myr}$. For a median mass difference between the SCC and $70 \mu\text{m}$ unique clumps or protostellar clumps of $170 - 370 M_{\odot}$, this yields an accretion rate of $\approx 200 - 440 M_{\odot} \text{ Myr}^{-1}$ as an upper limit if this is assumed to be the sole

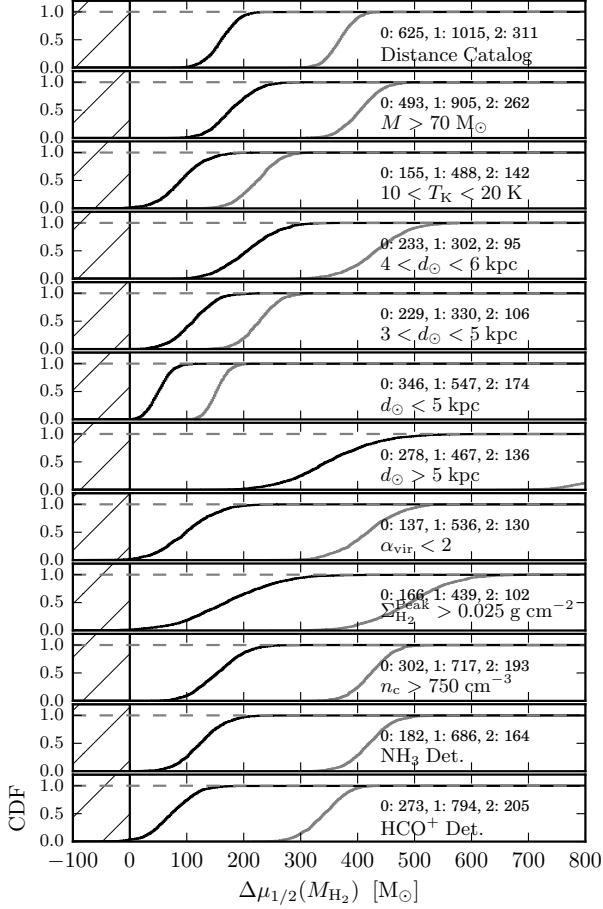


Figure 22. Cumulative distribution functions of the median mass difference $\Delta\mu_{1/2}(M_{H_2})$ drawn from the MC simulations based on different cuts in physical properties. The black curve shows the difference between the Hi-GAL Unique and SCCs, and the gray curve shows the difference between the Protostellar and SCCs. The cut is labeled in the bottom right of each panel and above are the sample numbers for SCC (0), Protostellar (1), and Hi-GAL 70 μm Unique (2). The values $\Delta\mu_{1/2}(M_{H_2}) \sim 100 M_{\odot}$ agree across a wide range of physical cuts designed to remove low mass, low density, or unbound objects.

explanation for the mass difference. Note that all molecular clouds cannot be collapsing on free-fall timescales and still be consistent with the observed Milky Way SFR (Zuckerman & Evans 1974). Other mechanisms such as magnetic and turbulent support would increase the clump collapse time and decrease the predicted growth rate.

As a simple estimate, we calculate the total mass available to a clump embedded in a GMC with typical properties. We assume a GMC with a spherical inflow velocity of $\Delta v \sim 1 \text{ km s}^{-1}$ onto a clump, feeding from a zone of $\Delta R_{\text{feed}} \sim 1.0 \text{ pc}$ over $t \sim 1 \text{ Myr}$. For median sized clump with $R_{\text{eq}} \sim 1 \text{ pc}$ and feeding zone density $n \sim 150 \text{ cm}^{-3}$ (N.B. median $n = 230 \text{ cm}^{-3}$ in GMCs in the Galactic Ring Survey, Roman-Duval et al. 2009), the homogeneous, spherical-shell reservoir mass would be $M_{\text{res}} \sim 250 M_{\odot}$. Higher inflow velocity or density would both increase the available mass. These values show that reasonable physical conditions within a GMC yield estimates that are consistent with the observed median mass difference between the SCCs and protostellar clumps, suggesting that cloud-to-clump accretion as a plausible physical mechanism.

There are theoretical models of such large scale clump ac-

cretion. For instance, Vázquez-Semadeni et al. (2009) invoke a model of hierarchical gravitational fragmentation in which multi-scale collapse occurs. In this picture, the mass accretion rate onto the clumps is determined by the clump tidal radius and initial gravitational well hierarchy (see also Smith et al. 2009). In another approach, Murray & Chang (2012) have explored a model of Bondi-Hoyle accretion of clumps within GMCs and predict that the clump mass accretion rate is slightly super-linear with mass of the clump ($\dot{M} \sim M_{\text{clump}}^{5/4}$). Maschberger et al. (2014) instead use a model of stochastic growth with a sub-linear mass growth rate ($\dot{M} \sim M_{\text{sink}}^{2/3}$). The exact nature of clump accretion and how it depends on the mass of the clump is still under debate; nevertheless, there is theoretical support for cloud-to-clump accretion.

There is also direct observational evidence for large scale flows onto clumps and filaments. One of the most striking examples is a flow estimated at $2500 M_{\odot} \text{ Myr}^{-1}$ traced by $\text{HCO}^+ 1-0$ blue asymmetric line profiles along a filamentary complex into the central clump of the source SDC335.579 – 0.272 (SDC335; Peretto et al. 2013). The total mass of this region is $5500 M_{\odot}$ which would place this among the most massive clumps in our survey. Another example of inflow onto clumps is seen in the converging flows toward the DR21 filament complex with inflow rates of $1000 M_{\odot} \text{ Myr}^{-1}$ onto 4900 and 3300 M_{\odot} clumps from infall profiles of the $1-0$ transitions of HCO^+ and CO (Schneider et al. 2010). Analysis of velocity centroids can also reveal potential mass inflow onto clumps along filaments (see three examples from the IRDC survey in Tackenberg et al. 2014) although there can be a degeneracy between inflow and outflow in the interpretation (Henshaw et al. 2014). These regions are already forming protostars and display hub-filament geometries where filaments of dense gas appear to converge on the central hub, so they are not exact analogues to the massive starless clumps in the BGPS survey; nevertheless, they show that clumps are deep gravitational potentials that draw surrounding material in.

The examples of large scale inflow also extend to nearby lower mass regions. For example, inflow signatures are seen in line profiles of $\text{HNC } 1-0$ toward the Serpens South region indicating mass flow rates of $130 M_{\odot} \text{ Myr}^{-1}$ onto the filament complex and $28 M_{\odot} \text{ Myr}^{-1}$ onto the central cluster (Kirk et al. 2013; for a higher resolution study of the same region, see Fernández-López et al. 2014). The central filament (L1495, B213) of the low-mass star-forming Taurus complex also shows direct evidence of a large scale flow in $\text{CO } 1-0$ of $27-50 M_{\odot} \text{ pc}^{-1} \text{ Myr}^{-1}$ perpendicular onto the filament complex (Palmeirim et al. 2013). While these last two examples occur in lower mass regions than the typical BGPS starless clumps, they show that flow rates of $10-100 M_{\odot} \text{ Myr}^{-1}$ are possible in low-mass regions. It therefore seems plausible that higher mass inflow rates of a few $100 M_{\odot} \text{ Myr}^{-1}$ should be possible in the more massive starless clump regions see in the BGPS.

6.3.3. Different Starless Clump vs. Protostellar Clump Lifetimes

A third explanation for the observed mass difference is that the lifetime of the SCC phase decreases with increasing total clump mass in exact proportion to the fraction of SCCs at each mass. The shorter lifetime of massive clumps explains the lack of very massive ($M > 10^4 M_{\odot}$) starless clumps candidates. We estimate the lifetime of this phase is less than 0.03 Myr based on the CH_3OH maser technique. Thus protostellar clumps with $> 10^4 M_{\odot}$ require an alternative formation mechanism: the average mass-growth from cloud-

to-clump accretion is not sufficient to explain the lack of these massive SCCs. Using even a high mass infall rate of $\sim 10^3 M_\odot \text{ Myr}^{-1}$, the most massive clumps could only accrete a meager few $\sim 10^1 M_\odot$ over their few $\sim 10^4$ yr starless-phase lifetimes.

The lifetime ratio of SCCs to Protostellar clumps would have to decrease with increasing mass in proportion to the ratio $N_{\text{SCC}}/N_{\text{proto}}$ if lifetimes arguments are the sole explanation for the observed median mass difference. The ratio of $N_{\text{SCC}}/N_{\text{proto}}$ scales as $M^{-0.4}$ over the range $100 \leq M \leq 1000 M_\odot$. The negative exponent implies that the lifetime scaling for SCCs is a steeper function of mass than the Protostellar clump lifetime. The value of the exponent is insensitive to the lower bound of the mass between 100 and $300 M_\odot$. There is no known theoretical prediction of such a lifetime scaling between high-mass SCCs and high-mass Protostellar clumps.

With the current data, it is difficult to disentangle the relative importance of differing lifetimes for SCCs and Protostellar clumps versus the importance of clump mass growth in explaining the median mass difference between SCCs and Protostellar clumps. It is likely that both processes occur.

7. SUMMARY

We present a sample of 4683 molecular cloud clumps from the BGPS sorted by different observational indicators of star formation activity. We use a variety of Galactic plane surveys in a common overlap region between $10^\circ < \ell < 65^\circ$ that include: $70 \mu\text{m}$ compact sources from *Herschel* Hi-GAL, mid-IR color-selected YSOs, H_2O and CH_3OH masers, and UCHII regions. We use Monte Carlo random sampling to calculate the clump physical properties using a subsample of 1640 well-constrained clump DPDFs. We also present a catalog of 1663 clump NH_3 T_K measurements and 22 GHz H_2O maser observations.

We find the following conclusions:

1. We identify a subsample of 2223 dense clumps with no indicators of star formation activity, representing the largest and most robust sample of starless clump candidates from a blind survey to date.
2. We measure numerous increasing trends in median physical properties from starless candidates to the most extreme indicator of star formation, UCHII regions. These include: $S_{1.1}^{\text{Total}}$ (Jy), $\Omega^{\text{Total}}/\Omega^{\text{FWHM}}$, T_K (K), $\Delta v(\text{NH}_3)$ (km s^{-1}), $R_{\text{eq}}^{\text{Total}}$ (pc), $\Sigma_{\text{H}_2}^{\text{FWHM}}$ (g cm^{-2}), n_c (cm^{-3}), and $M_{\text{H}_2}^{\text{Total}}$ (M_\odot).
3. Median mass SCCs ($230 M_\odot$) are capable of forming intermediate mass protostars up to $6 M_\odot$ (assuming a Kroupa IMF and $\epsilon_{\text{SF}} = 0.3$) which are detectable by current mid and far-infrared Galactic plane surveys. Mass is well correlated with radius for BGPS clumps, but the observed M - R relationship lies above the [Kauffmann & Pillai \(2010\)](#) thresholds for massive star formation for only 10.8% of SCCs.
4. The average SCC free-fall timescale is $\langle t_{\text{ff}} \rangle = 0.8 \text{ Myr}$. Using CH_3OH masers and counting the number of SCCs to CH_3OH maser containing clumps, we estimate that the lifetime of massive SCCs decreases as $\sim 0.37 \pm 0.08 \text{ Myr} (10^3 M_\odot / M)$ for $M > 10^3 M_\odot$. There are no SCCs observed with $M > 1.4 \times 10^4 M_\odot$ indicating a very short lifetime of $< 0.03 \text{ Myr}$. The majority of SCCs

(median total mass $230 M_\odot$) however have lifetimes that are longer than their average free-fall timescale.

5. Virial parameters derived from NH_3 show sub-virial clumps with median $\alpha = 0.7$. More than 75% of BGPS clumps are gravitationally bound ($\alpha < 2$). A median-property SCC would be in virial equilibrium if a modest $\sim 50 \mu\text{G}$ magnetic field is present.
6. We find a median mass difference between the SCC and protostellar categories of $\Delta M_{\text{H}_2}^{\text{Total}} = 170 - 370 M_\odot$. It is unlikely that this mass difference can be solely explained by a population of SCCs which are incapable of forming detectable protostars in current Galactic plane surveys. If the observed mass difference is not due to a systematic increase in dust opacity of 1.7 – 2.5 from SCCs to protostellar clumps, then there are two likely explanations: a) SCCs accrete mass from their surroundings and b) that the lifetime of SCCs is proportionally longer than Protostellar clumps at the same mass below $470 M_\odot$ and shorter than Protostellar clumps at masses above $470 M_\odot$. If mass accretion is the sole explanation then for an average clump free-fall timescale, $M \sim 200 - 440 M_\odot \text{ Myr}^{-1}$ is required. If the variation in SCC and Protostellar clump lifetimes is the sole explanation, then their ratio of lifetimes should scale as $M^{-0.4}$ for $100 \leq M \leq 1000 M_\odot$. In reality, both processes likely occur although it is not possible to disentangle them with the current data.

We sincerely thank the observatory staff at the Green Bank Telescope for their help during observing. We also sincerely thank Shari Breen for sharing coordinates to the MMB catalogue between $20^\circ < \ell < 60^\circ$ prior to publication. We would also like to thank Julia Kamenetzky and Kimberly Ward-Duong for many useful comments that benefited this paper. BES was supported by the National Science Foundation Graduate Research Fellowship under Grant No. DGE-1143953. YLS and BES were supported in part by the NSF Grants AST-1008577 and AST-1410190. NJE was supported by NSF grant AST-1109116 to the University of Texas at Austin. EWR was supported by a Discovery Grant from NSERC of Canada.

REFERENCES

- Aguirre, J. E., et al. 2011, *ApJS*, 192, 4 [1, 2](#)
 André, P., Belloche, A., Motte, F., & Peretto, N. 2007, *A&A*, 472, 519 [1](#)
 André, P., Di Francesco, J., Ward-Thompson, D., Inutsuka, S.-i., Pudritz, R. E., & Pineda, J. 2013, *ArXiv e-prints* [1](#)
 Bally, J., et al. 2010, *A&A*, 518, L90 [5, 6](#)
 Battersby, C. 2013, PhD thesis, University of Colorado at Boulder [21](#)
 Battersby, C., Bally, J., Dunham, M., Ginsburg, A., Longmore, S., & Darling, J. 2014, *ApJ*, 786, 116 [16](#)
 Battersby, C., Bally, J., Jackson, J. M., Ginsburg, A., Shirley, Y. L., Schlingman, W., & Glenn, J. 2010, *ApJ*, 721, 222 [8](#)
 Battersby, C., et al. 2011, *A&A*, 535, A128 [8](#)
 Benjamin, R. A., et al. 2003, *PASP*, 115, 953 [4](#)
 Bertoldi, F., & McKee, C. F. 1992, *ApJ*, 395, 140 [18](#)
 Beuther, H., Schilke, P., Menten, K. M., Motte, F., Sridharan, T. K., & Wyrowski, F. 2002, *ApJ*, 566, 945 [13](#)
 Boissier, S., & Prantzos, N. 1999, *MNRAS*, 307, 857 [21](#)
 Bonnell, I. A., Bate, M. R., Clarke, C. J., & Pringle, J. E. 2001, *MNRAS*, 323, 785 [3](#)
 Bonnell, I. A., Larson, R. B., & Zinnecker, H. 2007, *Protostars and Planets V*, 149 [3](#)
 Bonnor, W. B. 1956, *MNRAS*, 116, 351 [16](#)
 Bontemps, S., André, P., Terebey, S., & Cabrit, S. 1996, *A&A*, 311, 858 [15](#)
 Bontemps, S., Motte, F., Csengeri, T., & Schneider, N. 2010, *A&A*, 524, A18 [19](#)
 Breen, S. L., Ellingsen, S. P., Caswell, J. L., Green, J. A., Voronkov, M. A., Fuller, G. A., Quinn, L. J., & Avison, A. 2012a, *MNRAS*, 426, 2189 [7](#)
 —. 2012b, *MNRAS*, 421, 1703 [7](#)

- Breen, S. L., Ellingsen, S. P., Contreras, Y., Green, J. A., Caswell, J. L., Stevens, J. B., Dawson, J. R., & Voronkov, M. A. 2013, *MNRAS*, 435, 524 [7](#)
- Breen, S. L., et al. 2014, *MNRAS*, 438, 3368 [7](#)
- Bressert, E., Ginsburg, A., Bally, J., Battersby, C., Longmore, S., & Testi, L. 2012, *ApJ*, 758, L28 [20](#)
- Carey, S. J., et al. 2009, *PASP*, 121, 76 [4, 5](#)
- Chambers, E. T., Jackson, J. M., Rathborne, J. M., & Simon, R. 2009, *ApJS*, 181, 360 [8](#)
- Chen, X., Gan, C.-G., Ellingsen, S. P., He, J.-H., Shen, Z.-Q., & Titmarsh, A. 2013, *ApJS*, 206, 9 [5](#)
- Chomiuk, L., & Povich, M. S. 2011, *AJ*, 142, 197 [21](#)
- Churchwell, E., et al. 2009, *PASP*, 121, 213 [4](#)
- Contreras, Y., et al. 2013, *A&A*, 549, A45 [1](#)
- Crutcher, R. M. 2012, *ARA&A*, 50, 29 [18](#)
- Csengeri, T., et al. 2014, *A&A*, 565, A75 [1, 8, 16, 21](#)
- Cyganowski, C. J., et al. 2008, *AJ*, 136, 2391 [5](#)
- Danby, G., Flower, D. R., Valiron, P., Schilke, P., & Walmsley, C. M. 1988, *MNRAS*, 235, 229 [14](#)
- Davies, B., Hoare, M. G., Lumsden, S. L., Hosokawa, T., Oudmaijer, R. D., Urquhart, J. S., Mottram, J. C., & Stead, J. 2011, *MNRAS*, 416, 972 [21](#)
- di Francesco, J., Evans, II, N. J., Caselli, P., Myers, P. C., Shirley, Y., Aikawa, Y., & Tafalla, M. 2007, *Protostars and Planets V*, 17 [1](#)
- Duarte-Cabral, A., Bontemps, S., Motte, F., Hennemann, M., Schneider, N., & André, P. 2013, *A&A*, 558, A125 [21](#)
- Dunham, M. K., Robitaille, T. P., Evans, II, N. J., Schlingman, W. M., Cyganowski, C. J., & Urquhart, J. 2011a, *ApJ*, 731, 90 [4, 16](#)
- Dunham, M. K., Rosolowsky, E., Evans, II, N. J., Cyganowski, C., & Urquhart, J. S. 2011b, *ApJ*, 741, 110 [2, 3, 5, 9, 10, 18](#)
- Dunham, M. K., et al. 2010, *ApJ*, 717, 1157 [3, 18](#)
- Dunham, M. M., et al. 2014, *Protostars and Planets VI*, 195 [6](#)
- Ebert, R. 1955, *ZAp*, 37, 217 [16](#)
- Ellsworth-Bowers, T. P., Rosolowsky, E., Glenn, J., Ginsburg, A., Evans, II, N. J., Battersby, C., Shirley, Y. L., & Svoboda, B. 2014, *ArXiv e-prints* [2, 9, 10, 11](#)
- Ellsworth-Bowers, T. P., et al. 2013, *ApJ*, 770, 39 [2, 9, 10, 19](#)
- , 2015, *ArXiv e-prints* [2, 17](#)
- Evans, N. J., Shirley, Y. L., Mueller, K. E., & Knez, C. 2002, in *Astronomical Society of the Pacific Conference Series*, Vol. 267, *Hot Star Workshop III: The Earliest Phases of Massive Star Birth*, ed. P. Crowther, 17 [13](#)
- Fernández-López, M., et al. 2014, *ApJ*, 790, L19 [23](#)
- Furuya, R. S., Kitamura, Y., Wootten, A., Claussen, M. J., & Kawabe, R. 2003, *ApJS*, 144, 71 [7](#)
- Ginsburg, A., Bressert, E., Bally, J., & Battersby, C. 2012, *ApJ*, 758, L29 [21](#)
- Ginsburg, A., et al. 2013, *ApJS*, 208, 14 [1, 2, 3, 13, 17](#)
- Goldsmith, P. F. 2001, *ApJ*, 557, 736 [16](#)
- Greene, T. P., Wilking, B. A., Andre, P., Young, E. T., & Lada, C. J. 1994, *ApJ*, 434, 614 [5](#)
- Gutermuth, R. A., & Heyer, M. 2015, *AJ*, 149, 64 [5, 6](#)
- Guzmán, A. E., Sanhueza, P., Contreras, Y., Smith, H. A., Jackson, J. M., Hoq, S., & Rathborne, J. M. 2015, *ArXiv e-prints* [16](#)
- Habing, H. J. 1968, *Bull. Astron. Inst. Netherlands*, 19, 421 [16](#)
- Heiderman, A., Evans, II, N. J., Allen, L. E., Huard, T., & Heyer, M. 2010, *ApJ*, 723, 1019 [16, 17, 20](#)
- Henshaw, J. D., Caselli, P., Fontani, F., Jiménez-Serra, I., & Tan, J. C. 2014, *MNRAS*, 440, 2860 [23](#)
- Heyer, M., Krawczyk, C., Duval, J., & Jackson, J. M. 2009, *ApJ*, 699, 1092 [18](#)
- Ho, P. T. P., & Townes, C. H. 1983, *ARA&A*, 21, 239 [14](#)
- Hoare, M. G., et al. 2012, *PASP*, 124, 939 [4, 8](#)
- Hollenbach, D., Elitzur, M., & McKee, C. F. 2013, *ApJ*, 773, 70 [6](#)
- Hoq, S., et al. 2013, *ApJ*, 777, 157 [17](#)
- Huchra, J. P., & Geller, M. J. 1982, *ApJ*, 257, 423 [10](#)
- Imai, H., Obara, K., Diamond, P. J., Omodaka, T., & Sasao, T. 2002, *Nature*, 417, 829 [6](#)
- Jackson, J. M., et al. 2006, *ApJS*, 163, 145 [2](#)
- Jørgensen, J. K., Johnstone, D., van Dishoeck, E. F., & Doty, S. D. 2006, *A&A*, 449, 609 [13](#)
- Kauffmann, J., & Pillai, T. 2010, *ApJ*, 723, L7 [20, 24](#)
- Kauffmann, J., Pillai, T., & Goldsmith, P. F. 2013, *ApJ*, 779, 185 [18](#)
- Kirk, H., Myers, P. C., Bourke, T. L., Gutermuth, R. A., Hedden, A., & Wilson, G. W. 2013, *ApJ*, 766, 115 [23](#)
- Kroupa, P. 2001, *MNRAS*, 322, 231 [19, 21](#)
- Krumholz, M. R., Klein, R. I., & McKee, C. F. 2007, *ApJ*, 656, 959 [19](#)
- Krumholz, M. R., & McKee, C. F. 2008, *Nature*, 451, 1082 [17](#)
- Krumholz, M. R., & Thompson, T. A. 2012, *ApJ*, 760, 155 [15](#)
- Kuiper, R., Klahr, H., Beuther, H., & Henning, T. 2010, *ApJ*, 722, 1556 [19](#)
- Lada, C. J., & Lada, E. A. 2003, *ARA&A*, 41, 57 [19](#)
- Lada, C. J., Lombardi, M., & Alves, J. F. 2010, *ApJ*, 724, 687 [16, 17, 20](#)
- Larson, R. B. 1981, *MNRAS*, 194, 809 [15, 18](#)
- Launhardt, R., et al. 2013, *A&A*, 551, A98 [16](#)
- Longmore, S. N., et al. 2014, *Protostars and Planets VI*, 291 [20, 21](#)
- Lumsden, S. L., Hoare, M. G., Oudmaijer, R. D., & Richards, D. 2002, *MNRAS*, 336, 621 [4](#)
- Lumsden, S. L., Hoare, M. G., Urquhart, J. S., Oudmaijer, R. D., Davies, B., Mottram, J. C., Cooper, H. D. B., & Moore, T. J. T. 2013, *ApJS*, 208, 11 [4](#)
- Malinen, J., Juvela, M., Collins, D. C., Lunttila, T., & Padoan, P. 2011, *A&A*, 530, A101 [16](#)
- Maschberger, T., Bonnell, I. A., Clarke, C. J., & Moraux, E. 2014, *MNRAS*, 439, 234 [23](#)
- McKee, C. F., & Ostriker, E. C. 2007, *ARA&A*, 45, 565 [1](#)
- McKee, C. F., & Tan, J. C. 2003, *ApJ*, 585, 850 [3](#)
- Merello, M., Evans, II, N. J., Shirley, Y. L., Rosolowsky, E., Ginsburg, A., Bally, J., Battersby, C., & Dunham, M. M. 2015, *ArXiv e-prints* [2, 8, 20](#)
- Molinari, S., Schisano, E., Faustini, F., Pestalozzi, M., di Giorgio, A. M., & Liu, S. 2011, *A&A*, 530, A133 [5](#)
- Molinari, S., et al. 2010, *PASP*, 122, 314 [2, 4, 5](#)
- Morales, E. F. E., Wyrowski, F., Schuller, F., & Menten, K. M. 2013, *A&A*, 560, A76 [21](#)
- Mueller, K. E., Shirley, Y. L., Evans, II, N. J., & Jacobson, H. R. 2002, *ApJS*, 143, 469 [18](#)
- Murray, N., & Chang, P. 2012, *ApJ*, 746, 75 [23](#)
- Ossenkopf, V., & Henning, T. 1994, *A&A*, 291, 943 [15](#)
- Palmeirim, P., et al. 2013, *A&A*, 550, A38 [23](#)
- Pandian, J. D., Goldsmith, P. F., & Deshpande, A. A. 2007, *ApJ*, 656, 255 [7](#)
- Pandian, J. D., Momjian, E., Xu, Y., Menten, K. M., & Goldsmith, P. F. 2011, *ApJ*, 730, 55 [7](#)
- Pattle, K., et al. 2015, *ArXiv e-prints* [20](#)
- Peretto, N., & Fuller, G. A. 2009, *A&A*, 505, 405 [9](#)
- Peretto, N., et al. 2013, *A&A*, 555, A112 [23](#)
- Pestalozzi, M. R., Minier, V., & Booth, R. S. 2005, *A&A*, 432, 737 [7, 8, 21](#)
- Pillai, T., Kauffmann, J., Tan, J. C., Goldsmith, P. F., Carey, S. J., & Menten, K. M. 2015, *ApJ*, 799, 74 [18](#)
- Purcell, C. R., et al. 2013, *ApJS*, 205, 1 [8](#)
- Ragan, S. E., Henning, T., & Beuther, H. 2013, *A&A*, 559, A79 [1](#)
- Rebull, L. M., et al. 2007, *ApJS*, 171, 447 [21](#)
- Reid, M. J., et al. 2014, *ApJ*, 783, 130 [9](#)
- Robitaille, T. P., Whitney, B. A., Indebetouw, R., & Wood, K. 2007, *ApJS*, 169, 328 [6](#)
- Robitaille, T. P., Whitney, B. A., Indebetouw, R., Wood, K., & Denzmore, P. 2006, *ApJS*, 167, 256 [6, 7](#)
- Robitaille, T. P., et al. 2008, *AJ*, 136, 2413 [4](#)
- Roman-Duval, J., Jackson, J. M., Heyer, M., Johnson, A., Rathborne, J., Shah, R., & Simon, R. 2009, *ApJ*, 699, 1153 [10, 23](#)
- Roman-Duval, J., Jackson, J. M., Heyer, M., Rathborne, J., & Simon, R. 2010, *ApJ*, 723, 492 [11](#)
- Rosolowsky, E., et al. 2010, *ApJS*, 188, 123 [1, 2, 4](#)
- Rosolowsky, E. W., Pineda, J. E., Foster, J. B., Borkin, M. A., Kauffmann, J., Caselli, P., Myers, P. C., & Goodman, A. A. 2008, *ApJS*, 175, 509 [3](#)
- Schlingman, W. M., et al. 2011, *ApJS*, 195, 14 [2, 3, 13, 15, 16](#)
- Schneider, N., Csengeri, T., Bontemps, S., Motte, F., Simon, R., Hennebelle, P., Federrath, C., & Klessen, R. 2010, *A&A*, 520, A49 [23](#)
- Schuller, F., et al. 2009, *A&A*, 504, 415 [1](#)
- Scoville, N. Z., Yun, M. S., Sanders, D. B., Clemens, D. P., & Waller, W. H. 1987, *ApJS*, 63, 821 [18](#)
- Shirley, Y. L. 2015, *PASP*, 127, 299 [13, 22](#)
- Shirley, Y. L., Evans, II, N. J., Young, K. E., Knez, C., & Jaffe, D. T. 2003, *ApJS*, 149, 375 [13, 19](#)
- Shirley, Y. L., Huard, T. L., Pontoppidan, K. M., Wilner, D. J., Stutz, A. M., Bieging, J. H., & Evans, II, N. J. 2011, *ApJ*, 728, 143 [16](#)
- Shirley, Y. L., Nordhaus, M. K., Grevech, J. M., Evans, II, N. J., Rawlings, J. M. C., & Tatematsu, K. 2005, *ApJ*, 632, 982 [16](#)
- Shirley, Y. L., et al. 2013, *ApJS*, 209, 2 [2, 3, 9, 14, 22](#)
- Smith, R. J., Longmore, S., & Bonnell, I. 2009, *MNRAS*, 400, 1775 [23](#)
- Solomon, P. M., Rivolo, A. R., Barrett, J., & Yahil, A. 1987, *ApJ*, 319, 730 [18](#)
- Tackenberg, J., et al. 2012, *A&A*, 540, A113 [1, 8, 21](#)
- , 2014, *A&A*, 565, A101 [23](#)
- Tafalla, M., Myers, P. C., Caselli, P., & Walmsley, C. M. 2004, *Ap&SS*, 292, 347 [1](#)
- Tan, J. C., Beltran, M. T., Caselli, P., Fontani, F., Fuente, A., Krumholz, M. R., McKee, C. F., & Stolte, A. 2014, *ArXiv e-prints* [1](#)
- Traficante, A., Fuller, G. A., Peretto, N., Pineda, J. E., & Molinari, S. 2015a, *ArXiv e-prints* [1, 8, 9, 16, 17, 21](#)
- Traficante, A., Fuller, G. A., Pineda, J. E., & Pezzuto, S. 2015b, *A&A*, 574, A119 [9](#)
- Traficante, A., et al. 2011, *MNRAS*, 416, 2932 [5](#)
- Urquhart, J. S., et al. 2011, *MNRAS*, 418, 1689 [7, 19](#)
- , 2013a, *MNRAS*, 431, 1752 [19](#)
- , 2013b, *MNRAS*, 435, 400 [8, 19](#)
- , 2014, *MNRAS*, 443, 1555 [19](#)
- , 2015, *MNRAS*, 446, 3461 [7](#)
- Valdettaro, R., et al. 2001, *A&A*, 368, 845 [7](#)
- van der Walt, J. 2005, *MNRAS*, 360, 153 [21](#)
- Vázquez-Semadeni, E., Gómez, G. C., Jappsen, A.-K., Ballesteros-Paredes, J., & Klessen, R. S. 2009, *ApJ*, 707, 1023 [23](#)
- Walsh, A. J., Purcell, C. R., Longmore, S. N., Breen, S. L., Green, J. A., Harvey-Smith, L., Jordan, C. H., & Macpherson, C. 2014, *MNRAS*, 442, 2240 [6](#)
- Walsh, A. J., et al. 2011, *MNRAS*, 416, 1764 [4, 6, 7](#)
- Ward-Thompson, D., Scott, P. F., Hills, R. E., & Andre, P. 1994, *MNRAS*, 268, 276 [1](#)
- Wiener, M., Wyrowski, F., Schuller, F., Menten, K. M., Walmsley, C. M., Bronfman, L., & Motte, F. 2012, *A&A*, 544, A146 [3, 18](#)

- Wienen, M., et al. 2015, ArXiv e-prints [11, 20](#)
- Wilcock, L. A., et al. 2012, MNRAS, 424, 716 [1, 13](#)
- Wolfire, M. G., McKee, C. F., Hollenbach, D., & Tielens, A. G. G. M. 2003, ApJ, 587, 278 [9, 19](#)
- Young, K. E., Lee, J.-E., Evans, II, N. J., Goldsmith, P. F., & Doty, S. D. 2004, ApJ, 614, 252 [16](#)
- Zuckerman, B., & Evans, II, N. J. 1974, ApJ, 192, L149 [23](#)

Table 1
Observed 1.1 mm Properties

ID number	Source	Peak R.A. (J2000)	Peak Decl. (J2000)	Ω^{FWHM} (sq. $'$)	Ω^{Total} (sq. $'$)	$\theta_{\text{eq}}^{\text{FWHM}}$ ($''$)	$\theta_{\text{eq}}^{\text{Total}}$ ($''$)	$S_{1.1}^{\text{FWHM}}$ (mJy)	$S_{1.1}^{\text{Total}}$ (mJy)
2351	BGPSv2_G010.013+00.082	18 07 29.0	-20 14 18.0	1.613	2.534	39.7	51.3	760 (160)	1000 (200)
2352	BGPSv2_G010.027-00.354	18 09 08.3	-20 26 15.8	1.598	3.456	39.5	60.7	1420 (190)	2110 (290)
2353	BGPSv2_G010.051-00.208	18 08 38.6	-20 20 45.5	0.734	0.994	23.9	29.4	420 (120)	490 (140)
2354	BGPSv2_G010.059-00.210	18 08 40.0	-20 20 23.8	0.965	1.037	28.9	30.3	250 (110)	290 (120)
2355	BGPSv2_G010.061-00.174	18 08 32.2	-20 19 14.7	1.397	1.930	36.4	44.0	780 (160)	930 (180)
2356	BGPSv2_G010.069-00.406	18 09 25.2	-20 25 34.2	1.210	5.328	33.4	76.4	1050 (160)	2750 (350)
2357	BGPSv2_G010.079-00.414	18 09 28.2	-20 25 16.6	0.778	1.080	24.9	31.1	570 (120)	680 (140)
2358	BGPSv2_G010.079-00.194	18 08 38.9	-20 18 52.9	1.670	3.096	40.5	57.2	1510 (190)	2010 (250)
2359	BGPSv2_G010.083-00.434	18 09 33.2	-20 25 38.8	0.547	0.763	18.8	24.5	310 (100)	390 (120)
2360	BGPSv2_G010.105-00.416	18 09 31.9	-20 23 58.2	0.936	2.117	28.3	46.4	850 (140)	1320 (210)

Note. — Uncertainties are given in parentheses.

(This table is available in its entirety in the online journal. A portion is shown here for guidance regarding its form and content.)

Table 2
Observed NH₃ Properties

ID Number ^a	GBT R.A. (J2000)	GBT Decl. (J2000)	θ_{offset} (")	v_{LSR} (km s ⁻¹)	σ_v (km s ⁻¹)	$T_{\text{mb}}(1,1)$ (K)	$W(1,1)$ (K km s ⁻¹)	$T_{\text{mb}}(2,2)^b$ (K)	$W(2,2)^b$ (K km s ⁻¹)	$T_{\text{mb}}(3,3)^b$ (K)	$W(3,3)^b$ (K km s ⁻¹)
2351	18 07 28.3	-20 14 10.3	12.9	30.1300 (0.1600)	0.6900 (0.1600)	0.73 (0.20)	1.57 (0.58)	0.58 (0.20)	-0.06 (0.58)	0.67 (0.22)	0.83 (0.58)
2356	18 09 25.6	-20 25 43.6	11.0	11.7570 (0.0170)	0.8700 (0.0160)	3.82 (0.22)	32.32 (0.64)	1.37 (0.20)	3.07 (0.63)	0.88 (0.22)	0.21 (0.64)
2358	18 08 38.8	-20 18 58.9	6.1	28.2010 (0.0170)	0.8770 (0.0160)	3.62 (0.21)	27.42 (0.62)	1.29 (0.19)	3.35 (0.62)	0.88 (0.23)	0.20 (0.69)
2360	18 09 32.3	-20 24 07.7	11.5	11.7862 (0.0098)	0.8173 (0.0093)	6.03 (0.21)	42.04 (0.67)	2.39 (0.20)	4.62 (0.69)	1.02 (0.21)	0.05 (0.74)
2361	18 08 01.4	-20 12 19.1	10.8	41.8440 (0.0160)	1.0290 (0.0140)	4.04 (0.21)	34.86 (0.64)	2.04 (0.20)	5.65 (0.68)	0.92 (0.22)	-0.71 (0.74)
2367	18 09 27.0	-20 19 11.2	3.5	14.1900 (0.0220)	2.2420 (0.0210)	4.92 (0.25)	68.37 (0.90)	3.81 (0.22)	20.81 (0.86)	4.55 (0.33)	30.31 (1.28)
2372	18 09 36.9	-20 18 41.8	9.3	10.7959 (0.0046)	0.8328 (0.0041)	11.89 (0.23)	90.16 (0.69)	6.88 (0.21)	25.18 (0.69)	3.03 (0.23)	10.36 (0.76)
2376	18 09 05.4	-20 13 39.7	2.0	13.2780 (0.0240)	0.8210 (0.0240)	2.59 (0.21)	16.26 (0.61)	1.04 (0.20)	0.18 (0.62)	0.84 (0.24)	-0.43 (0.70)
2378	18 09 24.8	-20 15 37.6	2.1	10.9600 (0.0055)	1.3419 (0.0044)	12.33 (0.23)	168.72 (0.74)	8.47 (0.22)	52.84 (0.76)	5.10 (0.24)	28.28 (0.86)
2379	18 09 00.3	-20 11 37.5	6.2	11.7906 (0.0033)	0.7766 (0.0031)	16.59 (0.23)	114.18 (0.70)	9.21 (0.21)	33.00 (0.70)	4.87 (0.26)	17.92 (0.83)

Note. — Uncertainties are given in parentheses.

(This table is available in its entirety in the online journal. A portion is shown here for guidance regarding its form and content.)

^a B, C, D, and E denote multiple ammonia pointings that fall within a single 1.1 mm source.

^b Upper-limits are $T_{\text{mb}} < 4\sigma$ and $W < 5\sigma\Delta v\sqrt{N}$, where σ is the rms noise, Δv is the width of a single channel in velocity, and N is the number of pixels over which the average RMS was calculated.

Table 3
Observed H₂O Maser Properties

ID Number	GBT R.A. (J2000)	GBT Decl. (J2000)	θ_{offset} (")	$v_{\text{LSR}}(\text{peak})$ (km s ⁻¹)	v_{spread} (km s ⁻¹)	T_{mb} (K)	W (K km s ⁻¹)	N_{lines}
2380	18 07 49.6	-20 01 43.2	5.9	49.97	5.59	2.94 (0.17)	6.67 (0.22)	2
2381	18 08 41.6	-20 07 40.6	13.2	6.85	1.31	1.94 (0.17)	1.98 (0.12)	1
2386	18 08 48.1	-20 05 55.0	9.1	6.04	12.67	25.23 (0.17)	31.67 (0.26)	4
2392	18 09 23.1	-20 08 08.7	10.9	42.93	23.69	29.36 (0.20)	34.43 (0.25)	3
2394	18 09 02.2	-20 05 08.7	9.1	22.57	20.07	40.00 (0.17)	74.63 (0.36)	7
2396	18 09 00.6	-20 03 34.3	2.2	9.47	32.58	15.35 (0.18)	105.01 (0.43)	9
2406	18 09 21.5	-20 02 10.0	10.9	13.30	0.98	4.40 (0.17)	2.99 (0.12)	1
2411	18 08 45.1	-19 54 33.2	2.4	71.05	5.59	60.60 (0.20)	95.22 (0.23)	3
2415	18 09 01.7	-19 48 14.0	12.7	67.53	1.64	5.33 (0.17)	5.25 (0.14)	1
2418	18 10 22.5	-19 56 31.8	4.6	2.06	3.45	1.13 (0.18)	4.09 (0.24)	1

Note. — Uncertainties are given in parentheses.

(This table is available in its entirety in the online journal. A portion is shown here for guidance regarding its form and content.)

Table 4
Catalog Matching Statistics

Catalog	Min. ℓ (°)	Max. ℓ (°)	$< b $ (°)	Total BGPS	Source in BGPS	Source Match	Source Fraction	Clump Match	Clump Fraction
Hi-GAL	10	65	(all BGPS)						
HG0				4683	1847	0.3944
HG1				4683	944	0.2016
HG2				4683	1044	0.2229
HG3				4683	665	0.1420
HG4				4683	182	0.0389
CuTeX				4683	1369	0.2923
RMS	10	65	(all BGPS)						
HII region				4683	285	242	0.8491	205	0.0438
YSO				4683	158	135	0.8544	125	0.0267
Evolved star				4683	111	11	0.0991	11	0.0023
OH / IR star				4683	63	3	0.0476	3	0.0006
PN				4683	41	4	0.0976	1	0.0002
HII / YSO				4683	10	8	0.8000	8	0.0017
Other				4683	28	7	0.2500	7	0.0015
(All)				4683	696	410	0.5891	311	0.0664
MIPSGAL	10	65	1						
Archive				4682	106305	7492	0.0705	2976	0.6356
Catalog				4682	162125	5650	0.0348	2785	0.5948
(All)				4682	268430	13142	0.0490	3788	0.8091
Red Spitzer	10	65	1						
YSO				4682	3909	1246	0.3188	922	0.1969
sAGB				4682	1090	112	0.1028	108	0.0231
xAGB				4682	944	169	0.1790	159	0.0340
(All)				4682	5943	1527	0.2569	1085	0.2317
EGO	10	65	1	4682	91	81	0.8901	72	0.0154
H₂O									
GBT	446	...
Arcetri	202	146	0.7228	143	...
HOPS	10	30	0.5	2563	161	114	0.7081	92	0.0359
(All)	556	...
CH₃OH									
Pandian	35.2	53.7	0.41	674	88	76	0.8636	67	0.0994
MMB	10	60	1	4467	364	301	0.8269	272	0.0609
Pestalozzi	198	149	0.7525	144	...
(All)	650	526	0.8092	298	...
CORNISH	10	65	1	4682	228	219	0.9605	170	0.0363
Starless Cand.								2223	0.4747
Protostellar								2460	0.5253

Note. — Columns list the (1) catalog matched to the BGPS, (2) minimum Galactic longitude of the survey if applicable, (3) maximum Galactic longitude, (4) range in Galactic latitude, (5) total number of BGPS clumps in the catalog survey region, (6) number of catalog sources in the region with overlapping BGPS coverage, (7) number of catalog sources associated to BGPS clumps, (8) fraction of catalog sources matched to BGPS clumps, (9) number of unique associated BGPS clumps (10) fraction of BGPS clumps with associations.

Table 5
Star Formation Indicator Flags

ID Number	Activity		Hi-GAL Flag	MIPS		mid-IR				H ₂ O				CH ₃ OH				UCHII	
	SF?	P_{proto}		Cat.	Arch.	IR?	R08	RMS	EGO	H ₂ O?	GBT	Arc	HOPS	CH ₃ OH?	MMB	Pesta.	Pand.	UCHII?	Corn.
5096	1	1.00	2	5	5	1	1	0	0	1	1	0	0	1	2	0	0	1	1
5097	1	1.00	4	2	1	1	1	0	0	0	0	0	0	0	0	0	0	0	0
5098	1	1.00	1	5	7	1	1	0	0	0	0	0	0	0	0	0	0	0	0
5099	1	0.50	3	2	1	1	1	0	0	0	0	0	0	0	0	0	0	0	0
5100	1	1.00	1	1	2	1	1	0	0	0	0	0	0	0	0	0	0	0	0
5101	1	1.00	2	2	8	1	1	0	0	0	0	0	0	1	0	1	0	0	0
5102	1	1.00	1	3	6	1	1	0	0	0	0	0	0	0	0	0	0	0	0
5103	1	1.00	2	2	8	2	0	0	0	0	0	0	0	0	0	0	0	0	0
5104	0	0.00	0	2	3	0	0	0	0	0	0	0	0	0	0	0	0	0	0
5105	0	0.00	0	0	0	0	0	0	0	0	0	0	0	0	0	0	0	0	0

References. — see §3 for catalog descriptions.

Note. — Columns list the (1) BGPS ID number, (2) protostellar flag, (3) protostellar probability including R08 AGB contamination, (4) Hi-GAL visual inspection flag, (5-6) number of MIPS Catalog and Archive associations, (7) mid-IR group, 2 for uniquely R08 AGB, (8-10) number of mid-IR YSO associations, (11) H₂O group, 2 for uniquely GBT non-detection, (12-14) number of H₂O maser associations, (15) CH₃OH group, (16-18) number of CH₃OH maser associations, (19) UCHII group, and (20) number of CORNISH associations.

(This table is available in its entirety in the online journal. A portion is shown here for guidance regarding its form and content.)

Table 6
Clump Physical Properties

ID	d_{\odot} (pc)					$M_{\text{H}_2}^{\text{Total}}$ (M_{\odot})				
	Number	15.9	50.0	84.1	ML	$\sigma_{1/2}$	15.9	50.0	84.1	ML
2409	8073	8630	9264	8711	403.2	3863	4597	5522	4547	553.2
2416	4610	5050	5592	4714	324.7	575.4	719.3	909.8	629.1	108.7
2418	4602	5036	5581	5187	329.1	904.2	1107	1369.6	962.5	150.4
2421	4603	5046	5578	4899	322.0	1318	1617	2016	1455.5	229.1
2424	4595	5042	5577	4852	328.1	3763	4575	5662	4842	625.4
2425	4594	5037	5576	4800	332.3	3147	3830	4744	3888	529.0
2430	1564	2497	3853	2209	637.7	176.1	449.0	1301	327.2	219.0
2432	2436	3145	3849	3034	451.4	165.7	286.1	459.5	207.9	91.93
2433	2297	3047	3914	2882	502.3	276.9	490.9	822.9	425.5	164.0
2434	2369	3158	3964	2732	500.0	389.4	687.1	1120.7	564.8	226.3
2436	2443	3156	3786	3113	443.6	157.7	304.0	533.3	276.5	118.88

Note. — Physical properties calculated from the MC simulations for each clump in the Distance Sample. The percentiles of the posterior distributions (15.9 – 84.1), maximum likelihood (ML), and median absolute deviation ($\sigma_{1/2}$) with uncertainties are calculated. Columns list the (1) BGPS ID number, (2–4) heliocentric distance, (5–8) total mass.

(A subset of the derived physical properties (d_{\odot} , M) are shown above for guidance regarding the tables form and content. This table is available in its entirety in the online journal.

Table 7
Statistics of Observed and Physical Properties

Property	Indicator	N	10	25	50 ($\mu_{1/2}$)	75	90	$\sigma_{1/2}$
Ω^{Total} (sq. arcsec)	Starless Cand.	2223	920.2 ^{+3.7} _{-3.5}	1824.2 ^{+4.7} _{-4.7}	3620.4 ^{+8.2} _{-8.3}	6531 ⁺¹⁷ ₋₁₇	10668 ⁺³⁸ ₋₃₉	2110.9 ^{+6.2} _{-6.2}
	Protostellar	2460	2002.9 ^{+6.5} _{-6.6}	3678.3 ^{+9.8} ₋₁₀	7114 ⁺¹⁵ ₋₁₆	13755 ⁺³⁵ ₋₃₆	23286 ⁺⁶⁵ ₋₆₄	4191 ⁺¹² ₋₁₂
	70 μm Unique	995	1629.6 ^{+7.2} _{-7.0}	2908 ⁺¹¹ ₋₁₁	4985 ⁺¹⁷ ₋₁₇	9148 ⁺²⁸ ₋₂₈	14540 ⁺⁶³ ₋₆₄	2626 ⁺¹² ₋₁₂
	Mid IR	1022	2360 ⁺¹⁴ ₋₁₄	4575 ⁺¹⁵ ₋₁₅	8802 ⁺⁴² ₋₄₂	17114 ⁺⁵⁹ ₋₆₃	30320 ⁺¹³⁰ ₋₁₃₀	5416 ⁺²² ₋₂₂
	H ₂ O	556	3129 ⁺¹⁶ ₋₁₇	5912 ⁺³⁵ ₋₃₆	12445 ⁺⁴⁹ ₋₄₈	23076 ⁺⁷⁸ ₋₇₄	36950 ⁺²⁴⁰ ₋₂₃₀	7632 ⁺³⁶ ₋₃₆
	CH ₃ OH	298	3792 ⁺²³ ₋₂₃	7330 ⁺⁴⁹ ₋₄₇	15526 ⁺⁷⁷ ₋₇₅	27840 ⁺¹⁶⁰ ₋₁₆₀	40420 ⁺²⁷⁰ ₋₂₉₀	9135 ⁺⁶⁷ ₋₆₆
	UCHII	170	4661 ⁺⁴² ₋₄₄	9635 ⁺⁵⁷ ₋₅₄	18060 ⁺¹²⁰ ₋₁₁₀	31190 ⁺¹⁷⁰ ₋₁₈₀	45480 ⁺³⁴⁰ ₋₃₃₀	10238 ⁺⁹⁵ ₋₁₂₀
	$\Omega^{\text{Total}}/\Omega^{\text{FWHM}}$	Starless Cand.	2103	1.1517 ^{+0.0016} _{-0.0016}	1.2830 ^{+0.0016} _{-0.0016}	1.5534 ^{+0.0026} _{-0.0026}	2.0949 ^{+0.0043} _{-0.0042}	3.088 ^{+0.012} _{-0.012}
Protostellar		2426	1.2676 ^{+0.0023} _{-0.0023}	1.6210 ^{+0.0033} _{-0.0033}	2.5959 ^{+0.0054} _{-0.0053}	5.485 ^{+0.015} _{-0.015}	14.191 ^{+0.050} _{-0.050}	1.2064 ^{+0.0045} _{-0.0044}
70 μm Unique		975	1.1915 ^{+0.0023} _{-0.0023}	1.4324 ^{+0.0033} _{-0.0033}	1.9578 ^{+0.0053} _{-0.0053}	3.1400 ^{+0.0097} _{-0.0096}	5.167 ^{+0.024} _{-0.024}	0.6559 ^{+0.0047} _{-0.0047}
Mid IR		1010	1.3419 ^{+0.0046} _{-0.0045}	1.7800 ^{+0.0048} _{-0.0047}	3.030 ^{+0.010} _{-0.010}	7.570 ^{+0.032} _{-0.032}	16.923 ^{+0.081} _{-0.082}	1.6073 ^{+0.0092} _{-0.0094}
H ₂ O		555	1.886 ^{+0.011} _{-0.011}	3.350 ^{+0.019} _{-0.018}	7.142 ^{+0.048} _{-0.047}	16.566 ^{+0.077} _{-0.080}	39.33 ^{+0.24} _{-0.25}	4.906 ^{+0.037} _{-0.037}
CH ₃ OH		297	2.709 ^{+0.018} _{-0.017}	4.747 ^{+0.035} _{-0.034}	11.215 ^{+0.056} _{-0.057}	25.16 ^{+0.16} _{-0.16}	54.28 ^{+0.35} _{-0.35}	7.643 ^{+0.056} _{-0.056}
UCHII		170	4.066 ^{+0.035} _{-0.037}	8.501 ^{+0.054} _{-0.058}	16.377 ^{+0.085} _{-0.085}	34.87 ^{+0.25} _{-0.25}	59.61 ^{+0.46} _{-0.49}	10.906 ^{+0.080} _{-0.080}
$S_{1.1}^{\text{Total}}$ (Jy)		Starless Cand.	2223	0.1021 ^{+0.0031} _{-0.0030}	0.1891 ^{+0.0033} _{-0.0033}	0.3559 ^{+0.0046} _{-0.0046}	0.6729 ^{+0.0087} _{-0.0084}	1.275 ^{+0.018} _{-0.018}
	Protostellar	2460	0.2590 ^{+0.0023} _{-0.0023}	0.4639 ^{+0.0064} _{-0.0064}	0.9493 ^{+0.0099} _{-0.0099}	2.229 ^{+0.024} _{-0.025}	5.256 ^{+0.063} _{-0.065}	0.6093 ^{+0.0079} _{-0.0083}
	70 μm Unique	995	0.2058 ^{+0.0069} _{-0.0070}	0.3436 ^{+0.0072} _{-0.0071}	0.6090 ^{+0.010} _{-0.0099}	1.101 ^{+0.017} _{-0.017}	1.928 ^{+0.037} _{-0.036}	0.3220 ^{+0.0079} _{-0.0079}
	Mid IR	1022	0.320 ^{+0.011} _{-0.011}	0.624 ^{+0.013} _{-0.013}	1.348 ^{+0.021} _{-0.021}	3.448 ^{+0.049} _{-0.049}	8.26 ^{+0.16} _{-0.16}	0.929 ^{+0.018} _{-0.018}
	H ₂ O	556	0.516 ^{+0.019} _{-0.018}	1.050 ^{+0.031} _{-0.030}	2.579 ^{+0.048} _{-0.049}	6.71 ^{+0.12} _{-0.12}	14.29 ^{+0.30} _{-0.29}	1.917 ^{+0.042} _{-0.041}
	CH ₃ OH	298	0.600 ^{+0.031} _{-0.030}	1.326 ^{+0.043} _{-0.042}	3.363 ^{+0.068} _{-0.072}	9.09 ^{+0.21} _{-0.19}	18.52 ^{+0.50} _{-0.48}	2.519 ^{+0.059} _{-0.062}
	UCHII	170	0.896 ^{+0.047} _{-0.048}	2.115 ^{+0.097} _{-0.097}	4.63 ^{+0.12} _{-0.12}	11.37 ^{+0.29} _{-0.29}	19.78 ^{+0.63} _{-0.57}	3.562 ^{+0.10} _{-0.099}
	$S_{1.1}^{\text{FWHM}}$ (Jy)	Starless Cand.	2223	0.0619 ^{+0.0028} _{-0.0028}	0.1442 ^{+0.0029} _{-0.0029}	0.2871 ^{+0.0038} _{-0.0039}	0.5313 ^{+0.0066} _{-0.0063}	0.963 ^{+0.014} _{-0.014}
Protostellar		2460	0.1911 ^{+0.0043} _{-0.0043}	0.3425 ^{+0.0045} _{-0.0044}	0.6316 ^{+0.0061} _{-0.0061}	1.234 ^{+0.011} _{-0.011}	2.332 ^{+0.027} _{-0.025}	0.3611 ^{+0.0051} _{-0.0051}
70 μm Unique		995	0.1515 ^{+0.0056} _{-0.0055}	0.2610 ^{+0.0055} _{-0.0056}	0.4417 ^{+0.0069} _{-0.0070}	0.751 ^{+0.012} _{-0.012}	1.234 ^{+0.021} _{-0.020}	0.2176 ^{+0.0056} _{-0.0055}
Mid IR		1022	0.2344 ^{+0.0079} _{-0.0080}	0.4396 ^{+0.0085} _{-0.0085}	0.831 ^{+0.012} _{-0.012}	1.644 ^{+0.021} _{-0.021}	3.179 ^{+0.050} _{-0.048}	0.4908 ^{+0.0093} _{-0.0093}
H ₂ O		556	0.348 ^{+0.012} _{-0.012}	0.612 ^{+0.014} _{-0.013}	1.195 ^{+0.019} _{-0.019}	2.502 ^{+0.039} _{-0.039}	4.598 ^{+0.088} _{-0.088}	0.722 ^{+0.016} _{-0.017}
CH ₃ OH		298	0.388 ^{+0.017} _{-0.016}	0.687 ^{+0.019} _{-0.020}	1.304 ^{+0.028} _{-0.026}	2.901 ^{+0.058} _{-0.056}	5.61 ^{+0.17} _{-0.16}	0.812 ^{+0.026} _{-0.026}
UCHII		170	0.533 ^{+0.030} _{-0.030}	0.948 ^{+0.029} _{-0.029}	1.664 ^{+0.043} _{-0.042}	3.674 ^{+0.092} _{-0.092}	6.99 ^{+0.22} _{-0.21}	0.975 ^{+0.039} _{-0.037}
T_{K} (K)		Starless Cand.	248	11.685 ^{+0.084} _{-0.085}	12.485 ^{+0.073} _{-0.074}	13.961 ^{+0.096} _{-0.091}	16.57 ^{+0.16} _{-0.15}	21.64 ^{+0.38} _{-0.36}
	Protostellar	1164	12.688 ^{+0.045} _{-0.044}	14.081 ^{+0.042} _{-0.042}	16.577 ^{+0.055} _{-0.056}	21.62 ^{+0.14} _{-0.13}	27.98 ^{+0.21} _{-0.21}	3.133 ^{+0.052} _{-0.052}
	70 μm Unique	282	12.121 ^{+0.077} _{-0.083}	12.989 ^{+0.074} _{-0.072}	14.711 ^{+0.089} _{-0.089}	17.48 ^{+0.19} _{-0.19}	21.31 ^{+0.44} _{-0.37}	1.976 ^{+0.076} _{-0.074}
	Mid IR	556	12.868 ^{+0.061} _{-0.065}	14.116 ^{+0.058} _{-0.057}	16.584 ^{+0.075} _{-0.075}	21.82 ^{+0.23} _{-0.24}	28.18 ^{+0.32} _{-0.32}	3.011 ^{+0.071} _{-0.071}
	H ₂ O	499	13.770 ^{+0.067} _{-0.067}	15.508 ^{+0.070} _{-0.067}	19.17 ^{+0.12} _{-0.12}	25.76 ^{+0.11} _{-0.11}	31.45 ^{+0.19} _{-0.19}	4.353 ^{+0.071} _{-0.080}
	CH ₃ OH	232	15.28 ^{+0.17} _{-0.17}	17.84 ^{+0.13} _{-0.14}	22.48 ^{+0.21} _{-0.21}	27.33 ^{+0.21} _{-0.20}	32.39 ^{+0.22} _{-0.12}	4.74 ^{+0.13} _{-0.11}

Table 7 — Continued

Property	Indicator	N	10	25	50 ($\mu_{1/2}$)	75	90	$\sigma_{1/2}$
	UCHII	134	18.02 ^{+0.53} _{-0.36}	22.38 ^{+0.24} _{-0.37}	27.27 ^{+0.17} _{-0.18}	32.46 ^{+0.44} _{-0.13}	39.88 ^{+0.76} _{-0.84}	5.14 ^{+0.22} _{-0.17}
$\sigma_v(\text{NH}_3)$ (km s ⁻¹)	Starless Cand.	319	0.3085 ^{+0.0061} _{-0.0067}	0.4197 ^{+0.0051} _{-0.0051}	0.5671 ^{+0.0058} _{-0.0054}	0.882 ^{+0.010} _{-0.010}	1.485 ^{+0.030} _{-0.027}	0.2008 ^{+0.0052} _{-0.0048}
	Protostellar	1132	0.3998 ^{+0.0040} _{-0.0037}	0.5369 ^{+0.0031} _{-0.0031}	0.7160 ^{+0.0032} _{-0.0030}	0.9862 ^{+0.0042} _{-0.0043}	1.3305 ^{+0.0083} _{-0.010}	0.2157 ^{+0.0027} _{-0.0026}
	70 μm Unique	297	0.3555 ^{+0.0048} _{-0.0063}	0.4571 ^{+0.0054} _{-0.0049}	0.6222 ^{+0.0061} _{-0.0058}	0.8343 ^{+0.0067} _{-0.0057}	1.077 ^{+0.021} _{-0.019}	0.1819 ^{+0.0048} _{-0.0049}
	Mid IR	511	0.4002 ^{+0.0042} _{-0.0042}	0.5256 ^{+0.0038} _{-0.0039}	0.7132 ^{+0.0046} _{-0.0042}	0.9699 ^{+0.0063} _{-0.0063}	1.287 ^{+0.022} _{-0.016}	0.2165 ^{+0.0032} _{-0.0032}
	H ₂ O	493	0.5281 ^{+0.0044} _{-0.0050}	0.6636 ^{+0.0033} _{-0.0033}	0.8549 ^{+0.0050} _{-0.0050}	1.1253 ^{+0.0083} _{-0.0087}	1.469 ^{+0.015} _{-0.016}	0.2197 ^{+0.0036} _{-0.0034}
	CH ₃ OH	205	0.6210 ^{+0.0072} _{-0.0089}	0.7528 ^{+0.0067} _{-0.0067}	0.9851 ^{+0.0044} _{-0.0046}	1.321 ^{+0.011} _{-0.011}	1.627 ^{+0.036} _{-0.019}	0.2757 ^{+0.0066} _{-0.0080}
	UCHII	139	0.706 ^{+0.012} _{-0.012}	0.914 ^{+0.012} _{-0.013}	1.162 ^{+0.010} _{-0.013}	1.451 ^{+0.020} _{-0.014}	2.085 ^{+0.047} _{-0.047}	0.2676 ^{+0.0100} _{-0.0097}
d_\odot (kpc)	Starless Cand.	613	2.250 ^{+0.075} _{-0.071}	3.395 ^{+0.056} _{-0.056}	4.706 ^{+0.057} _{-0.055}	6.52 ^{+0.41} _{-0.29}	10.11 ^{+0.15} _{-0.14}	1.424 ^{+0.077} _{-0.072}
	Protostellar	1027	2.160 ^{+0.058} _{-0.056}	3.242 ^{+0.046} _{-0.045}	4.788 ^{+0.055} _{-0.054}	7.94 ^{+0.23} _{-0.25}	11.11 ^{+0.15} _{-0.17}	1.821 ^{+0.070} _{-0.068}
	70 μm Unique	311	2.18 ^{+0.11} _{-0.13}	3.208 ^{+0.088} _{-0.088}	4.680 ^{+0.092} _{-0.089}	7.86 ^{+0.45} _{-0.50}	10.90 ^{+0.26} _{-0.25}	1.77 ^{+0.13} _{-0.12}
	Mid IR	504	2.086 ^{+0.061} _{-0.060}	3.105 ^{+0.060} _{-0.063}	4.623 ^{+0.083} _{-0.079}	7.00 ^{+0.39} _{-0.33}	10.70 ^{+0.26} _{-0.24}	1.688 ^{+0.090} _{-0.084}
	H ₂ O	323	2.315 ^{+0.097} _{-0.098}	3.437 ^{+0.085} _{-0.080}	5.089 ^{+0.091} _{-0.092}	8.31 ^{+0.27} _{-0.31}	11.45 ^{+0.22} _{-0.33}	1.99 ^{+0.12} _{-0.12}
	CH ₃ OH	130	2.47 ^{+0.15} _{-0.15}	4.07 ^{+0.17} _{-0.18}	5.48 ^{+0.14} _{-0.13}	9.16 ^{+0.18} _{-0.21}	11.78 ^{+0.21} _{-0.23}	2.41 ^{+0.19} _{-0.20}
	UCHII	101	2.85 ^{+0.26} _{-0.27}	4.63 ^{+0.19} _{-0.20}	6.41 ^{+0.97} _{-0.47}	10.94 ^{+0.33} _{-0.36}	13.03 ^{+0.26} _{-0.23}	2.99 ^{+0.16} _{-0.16}
$R_{\text{eq}}^{\text{Total}}$ (pc)	Starless Cand.	613	0.352 ^{+0.010} _{-0.010}	0.5286 ^{+0.010} _{-0.0099}	0.842 ^{+0.016} _{-0.016}	1.333 ^{+0.035} _{-0.031}	2.152 ^{+0.071} _{-0.064}	0.366 ^{+0.012} _{-0.011}
	Protostellar	1027	0.431 ^{+0.011} _{-0.011}	0.705 ^{+0.012} _{-0.012}	1.251 ^{+0.021} _{-0.021}	2.162 ^{+0.042} _{-0.043}	3.376 ^{+0.075} _{-0.070}	0.638 ^{+0.012} _{-0.016}
	70 μm Unique	311	0.366 ^{+0.018} _{-0.017}	0.591 ^{+0.019} _{-0.018}	1.037 ^{+0.031} _{-0.028}	1.706 ^{+0.050} _{-0.046}	2.560 ^{+0.091} _{-0.12}	0.512 ^{+0.023} _{-0.021}
	Mid IR	504	0.453 ^{+0.016} _{-0.015}	0.758 ^{+0.018} _{-0.018}	1.308 ^{+0.031} _{-0.031}	2.257 ^{+0.067} _{-0.067}	3.46 ^{+0.11} _{-0.10}	0.648 ^{+0.025} _{-0.023}
	H ₂ O	323	0.579 ^{+0.022} _{-0.023}	0.899 ^{+0.027} _{-0.025}	1.574 ^{+0.044} _{-0.041}	2.833 ^{+0.068} _{-0.063}	3.981 ^{+0.097} _{-0.093}	0.849 ^{+0.033} _{-0.033}
	CH ₃ OH	130	0.812 ^{+0.048} _{-0.054}	1.352 ^{+0.056} _{-0.051}	2.309 ^{+0.098} _{-0.10}	3.28 ^{+0.13} _{-0.12}	4.56 ^{+0.21} _{-0.19}	0.967 ^{+0.064} _{-0.060}
	UCHII	101	0.991 ^{+0.14} _{-0.099}	1.653 ^{+0.073} _{-0.088}	2.656 ^{+0.073} _{-0.079}	3.876 ^{+0.096} _{-0.11}	5.02 ^{+0.15} _{-0.15}	1.111 ^{+0.062} _{-0.066}
$R_{\text{eq}}^{\text{FWHM}}$ (pc)	Starless Cand.	592	0.2593 ^{+0.0074} _{-0.0073}	0.4005 ^{+0.0073} _{-0.0071}	0.642 ^{+0.012} _{-0.012}	0.964 ^{+0.021} _{-0.019}	1.532 ^{+0.044} _{-0.041}	0.2694 ^{+0.0083} _{-0.0082}
	Protostellar	1020	0.2264 ^{+0.0058} _{-0.0056}	0.3653 ^{+0.0058} _{-0.0056}	0.6166 ^{+0.0092} _{-0.0089}	0.988 ^{+0.017} _{-0.017}	1.509 ^{+0.032} _{-0.032}	0.2847 ^{+0.0071} _{-0.0069}
	70 μm Unique	309	0.243 ^{+0.013} _{-0.012}	0.383 ^{+0.011} _{-0.011}	0.643 ^{+0.015} _{-0.017}	0.996 ^{+0.032} _{-0.030}	1.515 ^{+0.055} _{-0.066}	0.286 ^{+0.013} _{-0.012}
	Mid IR	499	0.2247 ^{+0.0088} _{-0.0087}	0.3543 ^{+0.0078} _{-0.0075}	0.602 ^{+0.012} _{-0.011}	0.981 ^{+0.023} _{-0.026}	1.523 ^{+0.052} _{-0.052}	0.2803 ^{+0.0095} _{-0.0091}
	H ₂ O	323	0.2105 ^{+0.010} _{-0.0095}	0.3400 ^{+0.0086} _{-0.0089}	0.551 ^{+0.013} _{-0.012}	0.870 ^{+0.022} _{-0.020}	1.326 ^{+0.047} _{-0.043}	0.2499 ^{+0.0095} _{-0.0098}
	CH ₃ OH	130	0.212 ^{+0.012} _{-0.012}	0.318 ^{+0.015} _{-0.015}	0.521 ^{+0.018} _{-0.017}	0.837 ^{+0.034} _{-0.031}	1.383 ^{+0.054} _{-0.060}	0.241 ^{+0.012} _{-0.012}
	UCHII	101	0.243 ^{+0.016} _{-0.017}	0.366 ^{+0.023} _{-0.020}	0.577 ^{+0.021} _{-0.021}	0.867 ^{+0.042} _{-0.033}	1.434 ^{+0.056} _{-0.073}	0.242 ^{+0.015} _{-0.015}
$\Sigma_{\text{H}_2}^{\text{Total}}$ (g cm ⁻²)	Starless Cand.	2222	5.67 ^{+0.17} _{-0.17}	9.23 ^{+0.17} _{-0.17}	14.53 ^{+0.20} _{-0.20}	21.86 ^{+0.30} _{-0.29}	30.88 ^{+0.49} _{-0.47}	6.03 ^{+0.14} _{-0.15}
	Protostellar	2459	8.09 ^{+0.18} _{-0.18}	12.56 ^{+0.18} _{-0.18}	19.29 ^{+0.19} _{-0.19}	28.10 ^{+0.28} _{-0.27}	39.19 ^{+0.47} _{-0.46}	7.50 ^{+0.14} _{-0.14}
	70 μm Unique	994	7.91 ^{+0.27} _{-0.27}	11.72 ^{+0.25} _{-0.25}	17.38 ^{+0.31} _{-0.30}	24.80 ^{+0.42} _{-0.42}	33.50 ^{+0.69} _{-0.65}	6.32 ^{+0.21} _{-0.21}
	Mid IR	1022	8.09 ^{+0.32} _{-0.30}	13.41 ^{+0.32} _{-0.32}	21.26 ^{+0.31} _{-0.31}	31.37 ^{+0.46} _{-0.46}	44.19 ^{+0.73} _{-0.71}	8.71 ^{+0.25} _{-0.25}
	H ₂ O	556	11.27 ^{+0.37} _{-0.36}	16.82 ^{+0.29} _{-0.30}	23.68 ^{+0.34} _{-0.32}	34.06 ^{+0.54} _{-0.54}	48.7 ^{+1.1} _{-1.1}	8.12 ^{+0.27} _{-0.27}
	CH ₃ OH	298	10.18 ^{+0.47} _{-0.48}	15.57 ^{+0.45} _{-0.46}	21.47 ^{+0.38} _{-0.37}	31.94 ^{+0.85} _{-0.82}	48.8 ^{+1.6} _{-1.5}	7.47 ^{+0.41} _{-0.40}
	UCHII	170	9.67 ^{+0.55} _{-0.54}	14.71 ^{+0.54} _{-0.56}	20.55 ^{+0.48} _{-0.47}	30.41 ^{+0.89} _{-0.87}	45.1 ^{+1.8} _{-1.7}	7.33 ^{+0.46} _{-0.44}
$\Sigma_{\text{H}_2}^{\text{FWHM}}$ (g cm ⁻²)	Starless Cand.	2138	5.54 ^{+0.22} _{-0.21}	9.94 ^{+0.21} _{-0.21}	16.56 ^{+0.25} _{-0.26}	26.51 ^{+0.41} _{-0.40}	42.00 ^{+0.90} _{-0.86}	7.72 ^{+0.19} _{-0.18}
	Protostellar	2439	9.75 ^{+0.24} _{-0.25}	16.53 ^{+0.28} _{-0.28}	28.90 ^{+0.37} _{-0.36}	51.61 ^{+0.59} _{-0.59}	90.2 ^{+1.2} _{-1.2}	15.13 ^{+0.28} _{-0.27}
	70 μm Unique	985	8.99 ^{+0.33} _{-0.35}	14.23 ^{+0.36} _{-0.35}	22.47 ^{+0.44} _{-0.41}	34.76 ^{+0.69} _{-0.69}	51.8 ^{+1.2} _{-1.2}	9.57 ^{+0.33} _{-0.32}
	Mid IR	1010	10.01 ^{+0.45} _{-0.43}	18.63 ^{+0.57} _{-0.56}	35.22 ^{+0.69} _{-0.66}	64.6 ^{+1.0} _{-1.0}	112.0 ^{+2.2} _{-2.2}	20.17 ^{+0.52} _{-0.52}
	H ₂ O	556	19.61 ^{+0.80} _{-0.81}	32.96 ^{+0.79} _{-0.79}	56.27 ^{+0.89} _{-0.91}	96.6 ^{+1.5} _{-1.5}	166.8 ^{+3.9} _{-3.7}	28.20 ^{+0.76} _{-0.77}
	CH ₃ OH	297	17.4 ^{+1.3} _{-1.2}	33.5 ^{+1.4} _{-1.4}	64.3 ^{+1.5} _{-1.5}	114.3 ^{+2.3} _{-2.3}	196.8 ^{+5.7} _{-5.7}	37.0 ^{+1.7} _{-1.3}
	UCHII	170	20.8 ^{+2.1} _{-2.0}	40.5 ^{+1.8} _{-1.7}	75.2 ^{+2.3} _{-2.3}	123.6 ^{+3.0} _{-2.8}	208.4 ^{+9.1} _{-8.1}	39.7 ^{+1.6} _{-1.7}
$\Sigma_{\text{H}_2}^{\text{peak}}$ (g cm ⁻²)	Starless Cand.	2222	0.13 ^{+0.49} _{-0.50}	8.66 ^{+0.42} _{-0.39}	20.82 ^{+0.51} _{-0.50}	38.45 ^{+0.76} _{-0.76}	61.8 ^{+1.3} _{-1.3}	14.05 ^{+0.36} _{-0.35}
	Protostellar	2459	7.72 ^{+0.53} _{-0.53}	19.86 ^{+0.53} _{-0.54}	40.75 ^{+0.68} _{-0.70}	75.1 ^{+1.1} _{-1.0}	125.3 ^{+1.8} _{-1.8}	24.83 ^{+0.52} _{-0.50}
	70 μm Unique	994	4.76 ^{+0.85} _{-0.87}	15.48 ^{+0.73} _{-0.77}	30.83 ^{+0.86} _{-0.87}	52.1 ^{+1.3} _{-1.2}	78.8 ^{+2.2} _{-2.1}	17.52 ^{+0.63} _{-0.62}
	Mid IR	1021	9.41 ^{+0.81} _{-0.84}	23.09 ^{+0.93} _{-0.94}	49.4 ^{+1.2} _{-1.2}	92.7 ^{+1.8} _{-1.8}	155.0 ^{+3.2} _{-3.3}	31.24 ^{+0.89} _{-0.88}
	H ₂ O	556	22.2 ^{+1.6} _{-1.6}	43.7 ^{+1.5} _{-1.5}	78.8 ^{+1.7} _{-1.7}	133.4 ^{+2.5} _{-2.5}	228.9 ^{+5.7} _{-5.7}	41.1 ^{+1.4} _{-1.4}
	CH ₃ OH	297	21.3 ^{+2.1} _{-1.9}	45.1 ^{+2.2} _{-2.2}	88.0 ^{+2.5} _{-2.5}	155.7 ^{+3.2} _{-3.7}	267.1 ^{+8.1} _{-8.1}	50.6 ^{+2.0} _{-2.0}
	UCHII	170	27.2 ^{+3.2} _{-2.9}	54.6 ^{+2.9} _{-2.9}	101.2 ^{+3.5} _{-3.5}	169.4 ^{+4.9} _{-4.7}	279 ⁺¹² ₋₁₂	54.0 ^{+2.8} _{-2.6}
$M_{\text{H}_2}^{\text{Total}}$ (M_\odot)	Starless Cand.	612	33.2 ^{+2.8} _{-2.6}	86.1 ^{+4.7} _{-4.6}	228 ⁺¹¹ ₋₁₁	639 ⁺³⁵ ₋₃₃	1610 ⁺¹¹⁰ ₋₁₀₀	179.3 ^{+9.5} _{-9.1}
	Protostellar	1026	65.2 ^{+4.3} _{-4.2}	183.8 ^{+8.0} _{-7.8}	596 ⁺²² ₋₂₁	1834 ⁺⁷³ ₋₆₉	4620 ⁺²¹⁰ ₋₂₁₀	503 ⁺¹⁹ ₋₁₈
	70 μm Unique	310	40.8 ^{+5.6} _{-5.0}	122.1 ^{+9.7} _{-9.4}	391 ⁺²⁶ ₋₂₅	1007 ⁺⁷⁸ ₋₇₁	2290 ⁺²⁰⁰ ₋₁₈₀	318 ⁺²² ₋₂₁

Table 7 — Continued

Property	Indicator	N	10	25	50 ($\mu_{1/2}$)	75	90	$\sigma_{1/2}$
	Mid IR	504	83.6 ^{+7.1} _{-6.7}	215 ⁺¹⁴ ₋₁₃	699 ⁺³⁷ ₋₃₆	2140 ⁺¹¹⁰ ₋₁₁₀	5060 ⁺³³⁰ ₋₃₂₀	587 ⁺³² ₋₃₁
	H ₂ O	323	140 ⁺¹⁴ ₋₁₃	384 ⁺²⁶ ₋₂₅	1164 ⁺⁷⁰ ₋₆₆	3350 ⁺²²⁰ ₋₂₀₀	7500 ⁺⁴⁴⁰ ₋₄₂₀	961 ⁺⁶⁰ ₋₅₆
	CH ₃ OH	130	224 ⁺⁶¹ ₋₄₅	700 ⁺⁷⁵ ₋₆₂	1970 ⁺¹⁸⁰ ₋₁₈₀	5180 ⁺³¹⁰ ₋₃₁₀	9930 ⁺⁹⁸⁰ ₋₈₀₀	1570 ⁺¹⁵⁰ ₋₁₄₀
	UCHII	101	354 ⁺⁸⁰ ₋₇₆	970 ⁺¹¹⁰ ₋₁₁₀	2590 ⁺²⁰⁰ ₋₁₈₀	5520 ⁺³⁵⁰ ₋₃₅₀	9810 ⁺⁹²⁰ ₋₈₆₀	1930 ⁺¹⁵⁰ ₋₁₄₀
$M_{\text{H}_2}^{\text{FWHM}}$ (M_{\odot})	Starless Cand.	613	19.7 ^{+2.0} _{-2.0}	61.5 ^{+3.5} _{-3.6}	166.2 ^{+8.1} _{-7.5}	450 ⁺²⁵ ₋₂₂	1141 ⁺⁷⁹ ₋₇₂	133.1 ^{+6.7} _{-6.3}
	Protostellar	1026	43.2 ^{+2.9} _{-2.9}	119.7 ^{+5.2} _{-4.9}	341 ⁺¹² ₋₁₁	944 ⁺³⁵ ₋₂₉	2068 ⁺⁹¹ ₋₈₃	274.5 ⁺¹⁰ _{-9.6}
	70 μm Unique	310	29.9 ^{+4.3} _{-3.7}	86.6 ^{+6.8} _{-6.6}	257 ⁺¹⁶ ₋₁₅	641 ⁺⁴⁷ ₋₄₃	1370 ⁺¹²⁰ ₋₁₁₀	203 ⁺¹⁴ ₋₁₃
	Mid IR	503	53.0 ^{+4.4} _{-4.2}	133.7 ^{+7.4} _{-7.1}	376 ⁺¹⁸ ₋₁₇	1037 ⁺⁵⁴ ₋₅₀	2310 ⁺¹⁴⁰ ₋₁₃₀	299 ⁺¹⁶ ₋₁₅
	H ₂ O	323	82.9 ^{+8.8} _{-8.3}	198 ⁺¹² ₋₁₁	494 ⁺³⁰ ₋₂₇	1373 ⁺⁷⁵ ₋₇₁	2710 ⁺¹⁷⁰ ₋₁₆₀	378 ⁺²⁴ ₋₂₂
	CH ₃ OH	130	109 ⁺²⁰ ₋₁₉	294 ⁺¹⁸ ₋₁₈	717 ⁺²⁷ ₋₂₆	1770 ⁺⁹⁸ ₋₉₈	3230 ⁺³²⁰ ₋₂₄₀	546 ⁺⁵⁵ ₋₄₉
	UCHII	101	152 ⁺³⁴ ₋₃₁	394 ⁺³⁸ ₋₃₉	1010 ⁺⁷⁴ ₋₇₁	1850 ⁺¹¹⁰ ₋₁₀₀	3180 ⁺⁴⁵⁰ ₋₄₂₀	689 ⁺⁴⁹ ₋₄₈
n_{c} (cm^{-3})	Starless Cand.	591	287 ⁺³⁰ ₋₃₁	645 ⁺³⁶ ₋₃₆	1338 ⁺⁶¹ ₋₅₇	2800 ⁺¹⁶⁰ ₋₁₄₀	6560 ⁺⁶⁹⁰ ₋₅₈₀	863 ⁺⁴⁷ ₋₄₅
	Protostellar	1019	390 ⁺²⁵ ₋₂₄	848 ⁺³² ₋₃₀	1857 ⁺⁵⁷ ₋₅₄	4160 ⁺¹⁵⁰ ₋₁₄₀	9880 ⁺⁶⁴⁰ ₋₅₈₀	1253 ⁺⁴⁶ ₋₄₅
	70 μm Unique	308	322 ⁺⁴³ ₋₄₃	721 ⁺⁵³ ₋₅₁	1475 ⁺⁸⁴ ₋₈₀	3000 ⁺²²⁰ ₋₁₉₀	6370 ⁺⁸⁶⁰ ₋₈₆₀	940 ⁺⁶⁴ ₋₆₆
	Mid IR	498	415 ⁺³⁶ ₋₃₆	917 ⁺⁴⁹ ₋₄₈	2120 ⁺⁹³ ₋₉₁	4760 ⁺²³⁰ ₋₂₂₀	11580 ⁺¹⁰⁰⁰ ₋₉₀₀	1468 ⁺⁷³ ₋₇₂
	H ₂ O	323	635 ⁺⁵⁰ ₋₄₈	1290 ⁺⁷⁵ ₋₇₅	2780 ⁺¹⁴⁰ ₋₁₄₀	6560 ⁺³⁷⁰ ₋₃₄₀	15670 ⁺¹⁸⁰⁰ ₋₈₀₀	1890 ⁺¹¹⁰ ₋₁₁₀
	CH ₃ OH	130	686 ⁺⁸⁹ ₋₈₇	1550 ⁺¹¹⁰ ₋₁₂₀	3080 ⁺²²⁰ ₋₂₁₀	8090 ⁺⁵⁵⁰ ₋₅₂₀	24900 ⁺¹⁷⁰⁰ ₋₁₇₀₀	2060 ⁺¹⁸⁰ ₋₁₆₀
	UCHII	101	539 ⁺⁷³ ₋₆₆	1300 ⁺¹⁸⁰ ₋₁₄₀	3460 ⁺²⁶⁰ ₋₂₄₀	7260 ⁺⁴⁴⁰ ₋₄₂₀	15600 ⁺¹⁶⁰⁰ ₋₁₄₀₀	2540 ⁺²⁰⁰ ₋₁₉₀
$t_{\text{ff,c}}$ (yr) $\text{val} \times 10^{-6}$	Starless Cand.	590	0.379 ^{+0.018} _{-0.018}	0.581 ^{+0.016} _{-0.016}	0.839 ^{+0.019} _{-0.018}	1.207 ^{+0.034} _{-0.031}	1.795 ^{+0.099} _{-0.085}	0.299 ^{+0.014} _{-0.014}
	Protostellar	1018	0.3092 ^{+0.0093} _{-0.0094}	0.4763 ^{+0.0086} _{-0.0083}	0.713 ^{+0.011} _{-0.011}	1.053 ^{+0.019} _{-0.019}	1.545 ^{+0.050} _{-0.047}	0.2729 ^{+0.0084} _{-0.0083}
	70 μm Unique	307	0.385 ^{+0.021} _{-0.024}	0.560 ^{+0.019} _{-0.019}	0.799 ^{+0.022} _{-0.022}	1.139 ^{+0.043} _{-0.040}	1.682 ^{+0.12} _{-0.099}	0.275 ^{+0.018} _{-0.017}
	Mid IR	498	0.286 ^{+0.012} _{-0.012}	0.446 ^{+0.011} _{-0.011}	0.667 ^{+0.014} _{-0.014}	1.013 ^{+0.028} _{-0.026}	1.503 ^{+0.070} _{-0.062}	0.264 ^{+0.011} _{-0.011}
	H ₂ O	322	0.2456 ^{+0.0071} _{-0.0078}	0.379 ^{+0.010} _{-0.010}	0.583 ^{+0.015} _{-0.014}	0.857 ^{+0.025} _{-0.024}	1.218 ^{+0.051} _{-0.044}	0.229 ^{+0.010} _{-0.010}
	CH ₃ OH	129	0.1948 ^{+0.0072} _{-0.0064}	0.341 ^{+0.011} _{-0.012}	0.553 ^{+0.021} _{-0.019}	0.782 ^{+0.032} _{-0.028}	1.173 ^{+0.080} _{-0.070}	0.221 ^{+0.015} _{-0.014}
	UCHII	100	0.247 ^{+0.012} _{-0.012}	0.361 ^{+0.011} _{-0.010}	0.523 ^{+0.020} _{-0.019}	0.852 ^{+0.051} _{-0.054}	1.325 ^{+0.092} _{-0.082}	0.204 ^{+0.017} _{-0.016}
α_{vir}	Starless Cand.	174	0.173 ^{+0.024} _{-0.024}	0.339 ^{+0.030} _{-0.028}	0.726 ^{+0.063} _{-0.058}	1.90 ^{+0.23} _{-0.19}	5.74 ^{+1.1} _{-0.89}	0.498 ^{+0.056} _{-0.049}
	Protostellar	637	0.167 ^{+0.012} _{-0.012}	0.338 ^{+0.015} _{-0.015}	0.676 ^{+0.026} _{-0.025}	1.353 ^{+0.059} _{-0.058}	2.90 ^{+0.24} _{-0.21}	0.415 ^{+0.021} _{-0.020}
	70 μm Unique	153	0.167 ^{+0.026} _{-0.025}	0.344 ^{+0.032} _{-0.032}	0.664 ^{+0.052} _{-0.049}	1.32 ^{+0.13} _{-0.12}	2.85 ^{+0.49} _{-0.40}	0.400 ^{+0.042} _{-0.039}
	Mid IR	319	0.153 ^{+0.016} _{-0.015}	0.302 ^{+0.018} _{-0.018}	0.591 ^{+0.032} _{-0.030}	1.162 ^{+0.067} _{-0.063}	2.18 ^{+0.22} _{-0.18}	0.359 ^{+0.024} _{-0.024}
	H ₂ O	276	0.204 ^{+0.023} _{-0.022}	0.407 ^{+0.026} _{-0.026}	0.810 ^{+0.044} _{-0.042}	1.564 ^{+0.10} _{-0.098}	3.33 ^{+0.39} _{-0.34}	0.484 ^{+0.035} _{-0.033}
	CH ₃ OH	94	0.204 ^{+0.043} _{-0.036}	0.430 ^{+0.047} _{-0.045}	0.866 ^{+0.074} _{-0.072}	1.61 ^{+0.18} _{-0.15}	3.29 ^{+0.61} _{-0.48}	0.513 ^{+0.061} _{-0.056}
	UCHII	81	0.212 ^{+0.049} _{-0.042}	0.484 ^{+0.071} _{-0.060}	1.05 ^{+0.11} _{-0.10}	2.12 ^{+0.36} _{-0.27}	5.04 ^{+1.3} _{-0.87}	0.673 ^{+0.092} _{-0.079}

Note. — Columns list the (1) physical property, unit, and numerical scale factor if applied, (2) star formation indicator category, (3) number of clumps in calculation, (4-8) 10th through 90th percentile, and (9) median absolute deviation. Uncertainties show the 1σ confidence interval.